

**BIOMASS-DERIVED ACTIVATED
CARBON SUBSTITUTED
POLYOXOMETALATES FOR ENERGY
APPLICATIONS**

Thesis

Submitted in partial fulfillment of the requirements for the degree

of

DOCTOR OF PHILOSOPHY

by

MADHUSREE J E (Reg. No: 197116CY011)



**DEPARTMENT OF CHEMISTRY
NATIONAL INSTITUTE OF TECHNOLOGY
KARNATAKA,
SURATHKAL, MANGALORE-575025
SEPTEMBER, 2024.**

DECLARATION

By the Ph.D. Research Scholar

I hereby *declare* that the Research Thesis titled "**Biomass-Derived Activated Carbon Substituted Polyoxometalates for Energy Applications,**" which is being submitted to the *National Institute of Technology, Karnataka, Surathkal*, in partial fulfillment of the requirements for the award of the *Degree of Doctor of Philosophy in Chemistry* is a *bonafide report of the research work carried out by me*. The materials contained in this Research Thesis have not been submitted to any University or Institution for the award of any degree.

Madhusree . J.E

MADHUSREE J E

Registration No.: 197116CY011

Department of Chemistry

Place: NITK Surathkal

Date: *19.09.2024*

CERTIFICATE

This is to *certify* that the Research Thesis titled "**Biomass-Derived Activated Carbon Substituted Polyoxometalates for Energy Applications,**" submitted by **MADHUSREE J E** (Registration Number: 197116CY011) as the record of the research work carried out by her, is *accepted* as the *Research Thesis submission* in partial fulfillment of the requirements for the award of the degree of *Doctor of Philosophy*.



Dr. Sib Sankar Mal

Supervisor

Associate Professor

Department of Chemistry

NITK Surathkal-575025



Chairperson - DRPC

डॉ. नरगत भार विवेदी (USRS Fellow)
प्राध्यापक एवं विभागाध्यक्ष / Professor & Head
रसायन शास्त्र विभाग / Chemistry Dept.
राष्ट्रीय प्रौद्योगिकी संस्थान कर्नाटक, सुपुल
NITK, SURATHKAL
मंगलूरु, कर्नाटक - 575 025

ACKNOWLEDGEMENT

I am deeply grateful for the support and cooperation of the many people who have helped me along the way as I worked on my thesis. I express my sincere gratitude to Dr. Sib Sankar Mal, Associate Professor, Department of Chemistry, NITK, for accepting me as a research student in his group. His guidance, inspiration, and thoughtful experience have been invaluable to me, providing immense support when I faltered, helping me overcome obstacles, and driving me to continue my research well. Most importantly I want to thank for being an elderly friend and Well-Wisher and I am certain that without his skillful guidance my Ph.D. would not have been possible.

My sincere thanks to my research progress assessment committee members Dr. Keyur Raval, Professor, Department of Chemical Engineering and Dr. Darshak R. Trivedi, Professor, Department of Chemistry, NITK, for assessing my research from time to time and for enlightening me with their technical suggestions and motivations right through my entire research period.

I thank the Heads of the Department (present and past) and all the faculty members of the Department of Chemistry for their support. I also extend my acknowledgment to all the non-teaching staff of the Chemistry department from whom I have received help in one way or another, which was important right along the way. I thank the Central Research Facility (CRF) of NITK for providing characterization resources.

I want to express my gratitude to Dr. Debaprasad Shee, Professor at the Department of Chemical Engineering, IIT Hyderabad, for his valuable technical suggestions. I am also thankful to Mr. Pranay R. Chandewar, a Research Scholar at IIT Hyderabad, and Dr Anjana A.V. for their immense support. Their contributions were a vital part of my work, and I couldn't have completed my Ph.D. without their presence.

It would be unfair if I fail to recognize Mr. Muhammed Anees P K, Mr. Joydeep Mahapatra, and Mr. Bhimaraya Biradar, from whom I have received key help that helped me comprehend my research field better and motivated to flourish further in the research.

I am happy to thank my co-workers and friends from the chemistry, physics, and metallurgical departments at NITK for their timely help and motivation.

I am forever grateful to my parents, who stood me up here, and without them, it would not have been possible. I want to thank my siblings for their limitless love, cheers, motivation, and support, which made my backbone straight and chin up.

Madhusree J E

*This thesis is dedicated to my parents
For their endless love, support and encouragement*

ABSTRACT

The rapid industrial and societal evolution has led to a population boom and a deepening energy crisis, rapidly depleting non-renewable sources. This urgency has shifted focus towards renewable energy sources like solar and wind power, despite their intermittency issues due to their reliance on environmental conditions. To address these challenges, advances in energy storage technologies, including batteries, fuel cells, and supercapacitors, have become critical. These innovations are essential in ensuring a continuous energy supply from renewable sources, marking a significant step towards a sustainable and energy-secure future. All kinds of batteries, such as lead and lithium-ion batteries, are examples of devices that store electric energy and have a high energy density. Nevertheless, most batteries have a low power density, which prevents them from meeting the need for energy that is more powerful and faster. In order to bridge these gaps, a supercapacitor was designed to store and release energy at a rapid pace. Because of its high-rate capabilities, it is ideal for supplying energy to electric cars, tramways, diesel engine starters, wind turbines, computers, lasers, cranes, and so on. Nanostructured carbon materials such as activated carbon, graphene, and carbon nanotubes have long been utilized as electrodes due to their inherent properties. Recently, biomass-derived activated carbon has emerged as a promising option for electrode material due to its impressive mechanical strength, cost-effectiveness, and eco-friendliness. In this work, we have investigated using Polyoxometalates (POMs) based nanocomposites to enhance the performance of a wide range of supercapacitor devices. POMs are inorganic metal oxide cluster assemblies of high-valent transition metal (Mo, V, W) with exceptional redox properties, structural diversity, and stability. These pseudocapacitive POMs act as multi-electron transfer redox agents, effectively serving as an electron sponge. However, using POMs directly as an electrode material is not feasible due to their low conductivity and high solubility in water, which leads to leaching. To overcome this, POMs are often wired over high-conductive surfaces to improve their conductivity. Our nanohybrid approach successfully leverages the synergistic effects between the elements to deliver superior energy storage performance.

Keywords: Supercapacitor, Biomass-derived activated carbon, Polyoxometalates, Specific capacitance, Energy density, Power density, Cyclic stability.

CONTENTS

DECLARATION

CERTIFICATE

ACKNOWLEDGEMENT

ABSTRACT

CONTENTS i

List of Figures vii

List of Tables xiii

List of Schemes xv

Nomenclature xii

List of abbreviation xix

CHAPTER 1

1.1 Introduction..... 1

1.2 Construction of Supercapacitor..... 4

1.3 Taxonomy of Supercapacitor 5

 1.3.1 Electric Double-layer supercapacitor (EDLC) 5

 1.3.2 Pseudocapacitor..... 7

 1.3.3 Hybrid Supercapacitor 8

 (i) Composite Hybrid Supercapacitor..... 9

 (ii) Asymmetric Hybrid Supercapacitor 10

 (iii) Battery type Hybrid Supercapacitor 10

1.4 Brief overview of "Technical terminologies intricate in the supercapacitor" 11

 1.4.1 Capacitance (C) 11

1.4.2 Energy Density (ED)	11
1.4.3 Power Density (PD)	12
1.4.4 Coulombic Efficiency	12
1.4.5 Cycle Life	12
1.5 Current Collectors	12
1.6 Separator	13
1.7 Electrolytes	13
1.7.1 Aqueous Electrolyte.....	14
1.7.2 Non-Aqueous Electrolyte.....	14
1.7.3 Solid Electrolyte.....	15
1.8 Electrode material.....	15
1.8.1 Electric double-layer capacitor	15
1.8.1.1 Biomass-derived Activated carbon (BDAC).....	18
1.8.1.2 Synthesis of Biomass-derived activated carbon.....	19
1.8.1.3 Carbonization.....	20
1.8.1.4 Activation Method	20
1.8.2 Polyoxometalates	24
1.8.2.1 Formation of Polyoxometalates	26
1.8.2.2 Keggin Polyoxometalates	26
1.8.2.3 Wells-Dawson Polyoxometalates	28
1.8.2.4 Properties.....	29
1.9 Applications	30
1.9.1 Public sector applications	30
1.9.2 Military and Defence application.....	30
1.9.3 Transport and Automobiles application.....	31
1.9.4 Memory backup chips.....	31

1.9.5 Medical and industrial application	31
CHAPTER 2	
2.1 Literature Review	33
2.2 Scope of the Work.....	36
2.3 Objectives.....	37
2.4 Organization of the Thesis	37
2.5 Materials and Methodology	39
2.5.1 Materials	39
2.5.2 Synthesis.....	39
2.5.2.1 Pyrolysis of orange peels produces activated carbon (OPAC)	39
2.5.2.2 Preparation of phosphomolybdic acid–orange peel-derived activated carbon (OPAC-PMA) nanohybrids	40
2.5.2.3 Synthesis of AC-P ₂ W ₁₈ composite	41
2.5.2.4 Synthesis of Alkaline Lignin derived activated carbon (LDAC).....	42
2.5.2.5 Synthesis of septadecatungstovanadodiphosphate K ₇ P ₂ VW ₁₇ O ₆₂ .xH ₂ O (P ₂ VW ₁₇)	42
2.5.2.6 Synthesis of the LDAC-P ₂ VW ₁₇ composite	43
2.5.2.7 Synthesis of pomegranate peel-derived activated carbon (PDAC)	43
2.5.2.8 Synthesis of diphosphovanadoseptamolybdate K ₇ P ₂ VMo ₁₇ O ₆₂ .xH ₂ O (P ₂ VMo ₁₇)	44
2.5.2.9 Synthesis of P ₂ VMo ₁₇ -PDAC	44
2.5.2.10 Synthesis of PVMo ₁₁ -PDAC	45
2.5.2.11 Synthesis of combined P ₂ VMo ₁₇ /PVMo ₁₁ in PDAC	45
2.5.3 Electrode Preparation	46
2.6 Characterization Techniques	46
2.6.1 Physical Characterization.....	46

2.6.1.1 Fourier transforms infrared spectroscopy (FTIR)	46
2.6.1.2 Thermal Gravimetric Analysis (TGA).....	47
2.6.1.3 Field emission scanning electron microscope (FESEM) and Energy dispersive X-ray analysis (EDS)	48
2.6.1.4 X-ray photoelectron spectroscopy (XPS).....	49
2.6.1.5 Powder X-ray diffraction (PXRD)	49
2.6.1.6 Brunauer-Emmett-Teller (BET) Analysis.....	50
2.6.2 Electrochemical Studies	51
2.6.2.1 Cyclic Voltammetry (CV).....	52
2.6.2.2 Galvanostatic charge and discharge studies (GCD).....	52
2.6.2.3 Electro Impedance Spectroscopy (EIS)	53
CHAPTER 3	
3. Result and Discussion	55
3.1 Structural, chemical, and morphological characterizations	55
3.1.1 FTIR.....	55
3.1.2 TGA.....	56
3.1.3 PXRD	57
3.1.4 XPS.....	58
3.1.5 FESEM	59
3.1.6 BET	60
3.2 Electrochemical Characterization	61
3.2.1 CV	61
3.2.2 GCD	63
3.2.3 EIS.....	65
3.2.4 Cycle Stability	66
3.4 Summary	67

CHAPTER 4

4. Results and discussion	69
4.1 Physical Characterization.....	69
4.1.1 FTIR.....	69
4.1.2 PXRD	70
4.1.3 XPS.....	71
4.1.4 BET	72
4.1.5 FESEM	73
4.2 Electrochemical Studies	74
4.2.1 CV	74
4.2.2 GCD	76
4.2.3 EIS.....	78
4.3 Summary	81

CHAPTER 5

5. Results and Discussion.....	83
5.1 Structural and Morphological Studies	83
5.2 Electrochemical Studies	89
5.3 Cyclic Stability	97
5.4 Summary	99

CHAPTER 6

6. Results and Discussion.....	101
6.1 FTIR	101
6.2 PXRD.....	102
6.3 FESEM.....	103
6.4 BET.....	105

6.5 Electrochemical Characterizations.....	106
6.6 Summary.....	115
CHAPTER 7	
7.1. Summary.....	117
7.2 Conclusions.....	119
7.3 Scope for Future Work.....	120
References.....	121
LIST OF PUBLICATION.....	137
Journal Publications from this thesis work.....	137
Workshop and conference attended.....	138
Curriculum Vitae.....	139

List of Figures

Figure 1.1: Ragone plot for the different electrochemical energy storage devices (Wayu 2021).....	2
Figure 1.2: Schematic diagram of supercapacitor (Samantara and Ratha 2018)..	4
Figure 1.3: Taxonomy of supercapacitor.....	5
Figure 1.4: Mechanism of the electrochemical double-layer capacitor(Roy et al. 2021).	6
Figure 1.5: Schematic representation of EDLC formation(Davies and Yu 2011). .	7
Figure 1.6: Schematic representation of Pseudocapacitors(Hossain et al. 2020). 8	
Figure 1.7: Classification of Hybrid Supercapacitor.	9
Figure 1.8: Schematic representation of Hybrid Supercapacitor(Liu et al. 2020). 9	
Figure 1.9: Crystal lattice in three dimensions of Graphite and Activated carbon(Harris et al. 2008).	17
Figure 1.10: Different types of biomass feedstocks (Bedia et al. 2018).	18
Figure 1.11: Schematic representation of synthesis of biomass-derived activated carbon.....	19
Figure 1.12: Schematic representation of types of Activation methods(Reza et al. 2020).	21
Figure 1.13: Graphical representation of Polyoxometalates material in supercapacitor year-wise(Source Scopus).....	25
Figure 1.14: Pie chart representation of Polyoxometalates based material in different applications(Khalilpour et al. 2021).	25
Figure 1.15: a) Keggin ($XM_{12}O_{40}$) b) Different addenda atom substituted Keggin POMs ($XM_{11}M'O_{40}$).	27
Figure 1.16: Graphical view of positions of Wells-Dawson POMs.	28
Figure 1.17: Plausible mechanism representation of changing parent POMs into lacunary POMs species and inserting different metal atoms.....	29
Figure 1.18: A diagrammatic illustration of the fundamental structure of a supercapacitor device and its multiple applications as an energy storage(Şahin et al. 2022).	32

Figure 2.1: Schematic representation of orange peel-derived activated carbon (OPAC) preparation.	40
Figure 2.2: Schematic representation of the synthesis of infusing phosphomolybdic acid into orange peel-derived activated carbon.	41
Figure 2.3: Schematic representation of the formation of AC-P ₂ W ₁₈ composite.	42
Figure 2.4: Schematic representation of impregnated septadecatungstovanadodiphosphate in lignin-derived activated carbon (LDAC-P ₂ VW ₁₇).	43
Figure 2.5: Schematic representation of infused Wells-Dawson and Keggin Polyoxometalates in pomegranate-derived activated carbon.....	45
Figure 2.6: Schematic representation of two electrode configuration setups.	46
Figure 2.7: FTIR setup (Image courtesy: Chemistry department, NITK, Surathkal).	47
Figure 2.8: TGA setup (Image courtesy: Chemistry department, NITK, Surathkal)...	48
Figure 2.9: FESEM and EDS setup (Image courtesy: Central research facility (CRF), NITK, Surathkal).	49
Figure 2.10: XPS setup (Image courtesy: Advanced Material Research Center. IIT Mandi).....	49
Figure 2.11: Powder XRD setup (Image courtesy: Central research facility (CRF), NITK, Surathkal).	50
Figure 2.12: BET setup (Image courtesy: Central research facility (CRF), NITK, Surathkal).....	51
Figure 2.13: Electrochemical workstation setup (Image courtesy: (Chemistry department, NITK, Surathkal).	51
Figure 3.1: FTIR Spectra of OPAC, OPAC-PMA, and PMA.....	56
Figure 3.2: The TGA graph of a) OPAC-PMA and OPAC, DTA Curves of b) OPAC-PMA and c) OPAC.....	57
Figure 3.3: Powder XRD spectrum of OPAC-PMA, PMA and OPAC.	58
Figure 3.4: XPS Analysis a) C1s b) O1s c) Mo 3d d) P2p.	59

Figure 3.5: a) FESEM image of OPAC, b) OPAC-PMA & c) EDS of OPAC, d) OPAC-PMA.....	60
Figure 3.6: N ₂ Adsorption and desorption Isotherm & b) Pore diameter of OPAC-PMA.....	61
Figure 3.7: Cyclic voltammetry graphs a) OPAC b) OPAC-PMA c) PMA d) Combination graph of OPAC, OPAC-PMA, and PMA.	62
Figure 3.8: GCD graph of a) OPAC b) OPAC-PMA c) Current densities vs Specific capacitance for all systems d) current density vs specific capacitance for OPAC & OPAC-PMA at 1 A g ⁻¹ e) Ragone plot for OPAC & OPAC-PMA and f) GCD graph of PMA.....	65
Figure 3.9: a) Nyquist plot b) Fitting the Nyquist plots requires using an equivalent circuit.	66
Figure 3.10: The cyclic stability response of (a) OPAC and (b) OPAC-PMA for 4000 cycles at a fixed current density of 6 A g ⁻¹ and (c) The fabricated supercapacitors are energizing red light-emitting diodes.	67
Figure 4.1: a) FTIR image of 5 wt%, 10 wt% and 15 wt% of AC-P ₂ W ₁₈ and Pure P ₂ W ₁₈ and b) PXRD image of 5 wt%, 10 wt%, 15 wt% of AC-P ₂ W ₁₈ and Pure P ₂ W ₁₈	70
Figure 4.2: XPS Analysis of AC-P ₂ W ₁₈ a) C1s b) O1s c) W4f and d) P2p.	72
Figure 4.3: a) N ₂ Adsorption and Desorption Graph of AC and 5 wt% AC-P ₂ W ₁₈ b) Pore Volume Distribution of AC and 5 wt% AC-P ₂ W ₁₈	72
Figure 4.4: a) FESEM image of Pure P ₂ W ₁₈ , b) 5 wt% AC-P ₂ W ₁₈ and EDS images of c) Pure P ₂ W ₁₈ and d) 5 wt% AC-P ₂ W ₁₈	74
Figure 4.5: Cyclic Voltammetry Graphs a) 5 wt% AC-P ₂ W ₁₈ , b) 10 wt% AC-P ₂ W ₁₈ , c) 15 wt% AC-P ₂ W ₁₈ , d) comparison graph of all three symmetric SC cells and e) Pure P ₂ W ₁₈	76
Figure 4.6: GCD graphs of a) 5 wt% AC-P ₂ W ₁₈ , b) 10 wt% AC-P ₂ W ₁₈ and c) 15 wt % AC-P ₂ W ₁₈ , d) Specific capacitance vs Current Density for 5 wt%, 10 wt% and 15 wt% of AC-P ₂ W ₁₈ , e) Ragone plot for all three nanohybrids and f) comparison graph for all three symmetric SC cell.	78

Figure 4.7:a) Nyquist plot and Cyclic stability of b) 5 wt% AC-P₂W₁₈, c) 10 wt% AC-P₂W₁₈ and d) 15 wt% AC-P₂W₁₈ and LED images of e) blue f) Yellow and f) Red light using the 5 wt% Ac-P₂W₁₈ Electrode material..... 81

Figure 5.1:FTIR Spectra of a) LDAC, b) P₂VW₁₇, c) 15 wt% of LDAC- P₂VW₁₇, d) 20 wt% of LDAC- P₂VW₁₇ and e) 30 wt% of LDAC- P₂VW₁₇. 84

Figure 5.2:PXRD Pattern of LDAC, P₂VW₁₇, 20 wt% of LDAC- P₂VW₁₇,*KOH impurities. 85

Figure 5.3:FESEM image of a) LDAC, b) P₂VW₁₇, and c) 20 wt% of LDAC-P₂VW₁₇ and EDS image d) LDAC e) P₂VW₁₇ and f) 20 wt% of LDAC-P₂VW₁₇..... 87

Figure 5.4:XPS Spectra of 20 wt% LDAC-P₂VW₁₇ a) C1s b) W4f c) V2p d) P2p.... 88

Figure 5.5:N₂ adsorption-desorption isotherm of LDAC and 20 wt% LDAC-P₂VW₁₇. 89

Figure 5.6:Cyclic Voltammetry graph of a) LDAC, b) P₂VW₁₇, c) 15 wt% LDAC- P₂VW₁₇, d) 20 wt% LDAC-P₂VW₁₇, e) 30 wt% LDAC-P₂VW₁₇ and f) comparison graph of specific capacitance vs. scan rate. 92

Figure 5.7:Galvanostatic charge and discharge graph of a) LDAC, b) P₂VW₁₇, c) 15 wt% LDAC-P₂VW₁₇, d) 20 wt% LDAC-P₂VW₁₇, e) 30 wt% LDAC-P₂VW₁₇, f) Ragone plot, g) Comparison graph of different wt% of LDAC-P₂VW₁₇, and Specific capacitance and Columbic efficiency vs current density graph of h) 15 wt% LDAC- P₂VW₁₇, i) 20 wt% LDAC-P₂VW₁₇ j) 30 wt% LDAC-P₂VW₁₇..... 95

Figure 5.8:a) Nyquist plot and b) Fitted Nyquist plot require an equivalent circuit... 97

Figure 5.9:Cyclic stability of a) 15 wt% LDAC-P₂VW₁₇, b) 20 wt% LDAC-P₂VW₁₇, c) 30 wt% LDAC-P₂VW₁₇, realistic application of 20 wt% LDAC- P₂VW₁₇ d) Series LED image, e) Red, Blue, Green LED image and f) piezoelectric buzzer image. 99

Figure 6.1:FTIR spectra of PDAC, PVMo₁₁, P₂VMo₁₇, and all nanocomposites..... 101

Figure 6.2:PXRD pattern of PDAC, PVMo₁₁, P₂VMo₁₇, 20 wt% PDAC- P₂VMo₁₇/PVMo₁₁, 40 wt% PDAC-P₂VMo₁₇/PVMo₁₁, 20 wt% PDAC-P₂VMo₁₇, 20 wt% PDAC-PVMo₁₁, and 40 wt% PDAC-PVMo₁₁..... 102

Figure 6.3:FESEM image of a) PDAC, b) 20 wt% of PDAC-P₂VMo₁₇ /PVMo₁₁, c) P₂VMo₁₇, and Elemental mapping image of 20 wt% of PDAC-P₂VMo₁₇/PVMo₁₁ d) Carbon e) Vanadium, f) Oxygen, g) Molybdenum and h) Phosphorous..... 104

Figure 6.4:a) N₂ adsorption-desorption isotherm of PDAC and 20 wt% PDAC-P₂VMo₁₇/PVMo₁₁ and b) Pore size distribution graph of PDAC and 20 wt% PDAC-P₂VMo₁₇/PVMo₁₁. 105

Figure 6.5:Cyclic Voltammetry graph of a) Pure PDAC, b) Pure PVMo₁₁, c) Pure P₂VMo₁₇, d) 20 wt% PDAC-PVMo₁₁, e) 40 wt% PDAC-PVMo₁₁, f) 20 wt% PDAC-P₂VMo₁₇, g) 20 wt% PDAC-P₂VMo₁₇/PVMo₁₁ h) 40 wt% PDAC-P₂VMo₁₇/PVMo₁₁ and i) comparison cyclic graph of 20 wt% PDAC-P₂VMo₁₇/PVMo₁₁, 20 wt% PDAC-P₂VMo₁₇ and 20 wt% PDAC-PVMo₁₁. 108

Figure 6.6:Galvanostatic charge and discharge graph of a) Pure PDAC, b) Pure P₂VMo₁₇, c) Pure PVMo₁₁, d) 20 wt% PDAC-PVMo₁₁, e) 40 wt% PDAC-PVMo₁₁, f) 20 wt% PDAC-P₂VMo₁₇, g) 20 wt% PDAC- P₂VMo₁₇/PVMo₁₁, h) 40 wt% PDAC-P₂VMo₁₇/PVMo₁₁, i) comparison graph of all nanocomposites specific capacitance versus current density at 0.2 A g⁻¹ and j) Ragone plot of all nanocomposites. 110

Figure 6.7:a) Nyquist plot and b) Fitted Nyquist plot require an equivalent circuit. 113

Figure 6.8:Cyclic Stability graph of a) 20 wt% PDAC- P₂VMo₁₇/ PVMo₁₁ b) 20 wt% PDAC- P₂VMo₁₇ and 40 wt% PDAC- PVMo₁₁ c) LED images of 20 wt% PDAC-P₂VMo₁₇/PVMo₁₁ d) red, e) green and f) blue..... 115

List of Tables

Table 1.1: Comparison of Energy Storage devices(Babu et al. 2020).	2
Table 4.1: Surface area and Porosity of 5 wt% AC-P ₂ W ₁₈ nanohybrid and AC.	73
Table 4.2: Equivalent circuit elements of all three nanocomposites plotted using Nyquist plots.	79
Table 5.1: Surface area and porosity of LDAC and 20 wt% LDAC-P ₂ VW ₁₇ .	89
Table 5.2: Fitted data from Nyquist plots of equivalent circuit elements of LDAC-P ₂ VW ₁₇ of 15 wt%, 20 wt%, and 30 wt%.....	96
Table 6.1: Surface area and porosity of PDAC and 20 wt% PDAC-P ₂ VMo ₁₇ /PVMo ₁₁ .	106
Table 6.2: Fitted data from Nyquist plots of equivalent circuit elements of 20 wt% PDAC-P ₂ VMo ₁₇ , 20 wt% PDAC-P ₂ VMo ₁₇ /PVMo ₁₁ , 40 wt% PDAC-P ₂ VMo ₁₇ /PVMo ₁₁ , and 20 wt% PVMo ₁₁ & 40 wt% PDAC-PVMo ₁₁	112

List of Schemes

Scheme 1.1: Schematic representation of the formation of Polyanions.	26
Scheme 5.1: Plausible reduction mechanism for P_2VW_{17} immobilized on LDAC surface.	91

Nomenclature

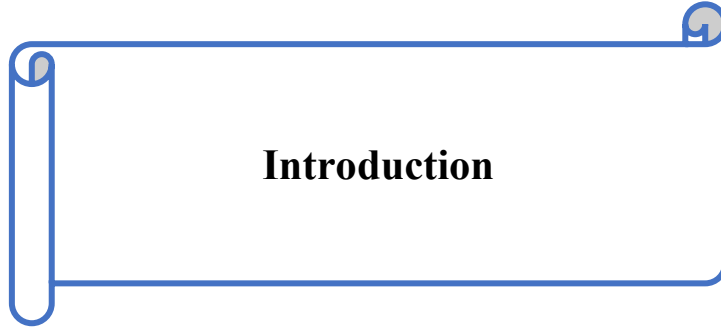
Symbol	Description
ϵ_r	Relative permittivity of the electrolyte
ϵ_0	Permittivity of free space
A	Surface area of the electrode
d	Thickness of HDL
Q	Electrical charge
V_R	Voltage
I	Discharge current
m	Mass of active material
ν	Scan rate
ΔV	Potential Window
C_s	Specific capacitance
X	Heteroatom
M	Addenda atom
Δt	Discharge time
$R_e(C)$	Real part of the capacitance
$I_m(C)$	Complex part of the capacitance
ω	Angular frequency
f_0	Cutt-off frequency
R_s	Series resistance
R_{ct}	Charge transfer resistance

List of abbreviations

Abbreviation	Full Form
PD	Power density
ED	Energy density
SC	Supercapacitors
EDLC	Electric double-layer capacitor
PC	Pseudocapacitor
HSC	Hybrid supercapacitor
OHP	Outer Helmholtz plane
IHP	Inner Helmholtz plane
PSD	Pore size distribution
POMs	Polyoxometalates
IPA	IsoPolyoxometalates
HPA	Heteropolyoxometalates
LED	Light-emitting diode
UPS	Uninterruptible power supply
SSAC	Soybean straw-derived activated carbon
FTIR	Fourier transforms infrared spectroscopy
PXRD	Powder X-ray diffraction
FESEM	Field emission scanning electron microscope
EDS	Energy dispersive X-ray analysis
BET	Brunauer-Emmett-Teller
TGA	Thermal Gravimetric Analysis
AC	Activated carbon
DMF	Dimethylformamide
ESCs	Electrochemical supercapacitors
PMA	Phosphomolybdic acid

PTA	Phosphotungstic acid
PDAC	Pomegranate peel-derived activated carbon
LDAC	Lignin-derived activated carbon
OPAC	Orange peel-derived activated carbon
PVDF	Polyvinylidene fluoride
NMP	N-Methylpyrrolidone
HPLC	High-performance liquid chromatography
CV	Cyclic voltammetry
GCD	Galvanostatic charge-discharge
EIS	Electrochemical Impedance spectroscopy
CNTs	Carbon nanotubes
XPS	X-ray photoelectron spectroscopy

CHAPTER 1



Introduction

1.1 Introduction

The energy demand has been increasing rapidly in recent years due to the growth of urban civilization and industrialization. However, the conventional approach of using non-renewable sources such as fossil fuels and natural gas is no longer sustainable due to their depletion and contribution to air pollution and global warming. The ecology and the global economy are both seriously threatened by this. Therefore, it has become necessary to identify and adopt alternative sources of renewable energy that are economically viable and environmentally friendly. Numerous studies have been conducted to find sources that can replace fossil fuels (Rajaitha et al. 2022; Iordache et al. 2013).

To produce energy responsibly, fossil fuels must be replaced by renewable energy sources like solar and wind power. While sustainable energy is accessible and environmentally friendly, it faces a significant challenge in its storage capacity due to its irregularities. Therefore, it is essential to store the energy available in a ready-to-use manner. Several energy storage devices, such as capacitors, supercapacitors, batteries, and fuel cells, are available to store energy and release it ready-to-use (Luo et al. 2015; Midilli et al. 2005).

Batteries are one of the most commonly known energy storage technologies capable of storing significant amounts of energy and supplying power to consumer electronics and automobiles. However, they have a low power density (PD), making them unsuitable for vehicle use. In contrast, capacitors have high power density but less energy density (ED) (Panwar et al. 2011; Baek et al. 2014).

However, supercapacitors are the most effective technology for bridging the gap between batteries and capacitors. Like capacitors and batteries, they have high power and energy density, making them perfect for renewable energy systems, electric cars, and other applications. Finally, supercapacitors are promising technological advancements that may contribute to developing a more efficient and sustainable energy system (**Table 1.1**) (Winter and Brodd 2004; Babu et al. 2020).

A Ragone plot (**Figure. 1.1**) is a graph that compares the energy density (ED) of an energy storage system with its power density (PD). The ED is the amount of energy stored in a unit of mass or volume, while the PD is the amount of power that can be delivered in a unit of time. The Ragone plot is a useful tool for comparing the performance of different energy storage systems (Kötz and Carlen 2000).

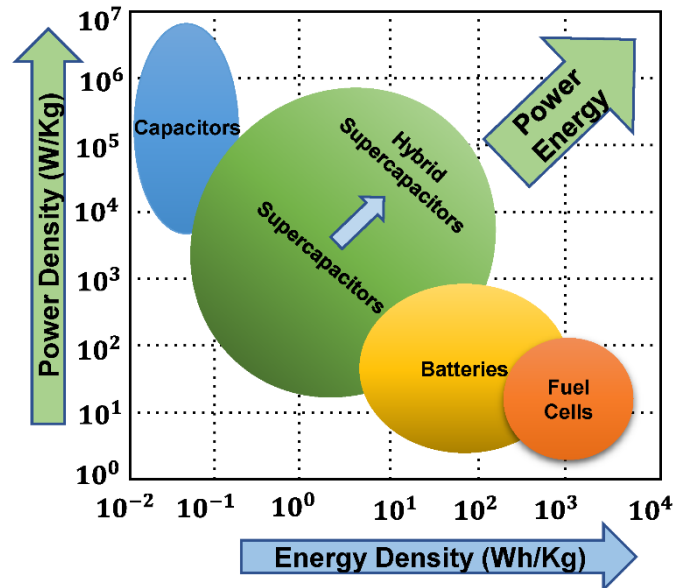


Figure 1.1: Ragone plot for the different electrochemical energy storage devices (Wayu 2021).

Table 1.1: Comparison of Energy Storage devices (Babu et al. 2020).

Parameters	Capacitor	Supercapacitor	Battery	Fuel Cells
Cycle Life	More than 1,000,000	1,000,000	500-2000	Not Applicable
Energy Density (Wh kg ⁻¹)	0.001-.03	0.5-20	30-265	500-2000
Power Density (W kg ⁻¹)	> 5,000	5000-10000	100-3000	1000
Operating Voltage (V)	6-800	1-5.5	1.2-4.2	0.6-0.7

Operating temperature (°C)	-20°C to 100°C	-45°C to + 85°C	-20°C to +65°C	+65°C to +1000
Cost per Wh	0.10-1	10-20	01-02	0.035-0.005

Fuel, like hydrogen, has chemical energy, which can be converted into electrical energy using fuel cells to produce power. An electrochemical interaction between the fuel and an oxidizing agent, typically oxygen, occurs during conversion. Because of their high energy density and efficiency, fuel cells may be used in stationary power production and electric vehicle applications (Dodds et al. 2015).

Chemical energy is stored in batteries through a reversible process involving an electrolyte and two electrodes. The energy is released when the reaction is reversed, and electrons go from one electrode to the other via an external circuit. Batteries are more suited for applications requiring a constant and continuous power output, such as grid-scale energy storage and portable devices; batteries have high energy density and less power density than supercapacitors (Sazali et al. 2020).

The insulating layer separates the two conducting parallel plates, providing the electric field that stores energy in capacitors. Compared to batteries, supercapacitors have a lower energy density but a higher power density. Applications that need brief, high-power bursts, including power conditioning systems and camera flashes, frequently employ capacitors (Wang et al. 2012). An electrochemical energy storage device known as a supercapacitor (SC) uses reversible ion absorption and desorption between the electrode material and electrolyte to store and distribute charge (**Figure. 1.2**). Electrochemical capacitors and ultracapacitors are other names for SCs. Unlike batteries, they can withstand several cycles of charging and discharging. SCs are environmentally friendly, with extended cycle lives, high power densities, specific capacitance, and flexible operating temperatures. They may replace traditional capacitors and charge fast with rapid power transfer. It can close the gap between the fuel cells, batteries, and capacitors (Devillers et al. 2014; Simon et al. 2014; Zhang et al. 2018).

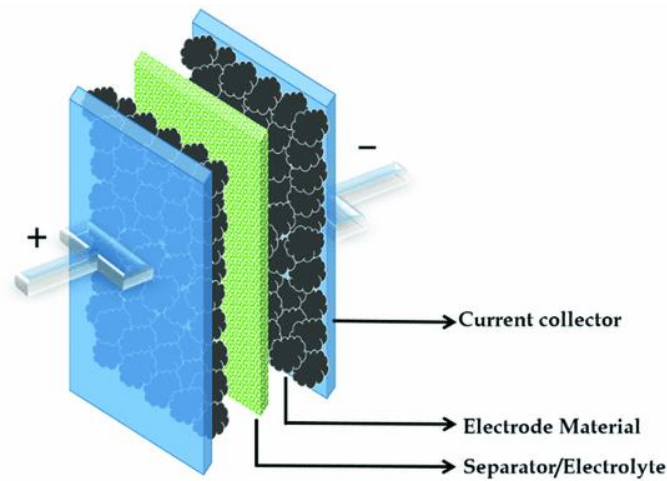


Figure 1.2: Schematic diagram of supercapacitor (Samantara and Ratha 2018).

1.2 Construction of Supercapacitor

Supercapacitor is a device that stores electrical charge efficiently, similar to batteries. It has three main elements: a separator, an electrolyte, and two electrodes. The most important of these elements is the electrode material, usually made up of nanoscale components containing high surface area and porosity, allowing optimal energy storage. The charges store and separate between the interface of electrodes. The electrodes are composed of conductive particles, including carbon, conducting polymers, or metal oxides, while the electrolyte separates them. An electrochemical supercapacitor is an essential tool for energy storage with numerous potential applications (Wang et al. 2012). This system operates as a capacitor including an electric double-layer capacitance capability, which the **Equation (1.1)** can represent:

$$C = \epsilon_r A / d \quad (1.1)$$

C denotes the capacitance of the electric double-layer. A is represented by the electrode surface. The medium's dielectric constant, equal to 1 for a vacuum and greater than 1 for all other materials, including gases, is denoted by ϵ_r . The appropriate thickness of the electric double layer is represented by d . By optimizing these parameters, supercapacitors can be designed to achieve specific performance characteristics, including energy density, power density, and cycle life, making them a crucial component in many electronic devices (Conway and Pell 2003).

1.3 Taxonomy of Supercapacitor

The Supercapacitor cell stores and distributes ions from the electrolyte to the electrode's surface area. Supercapacitors are classified into three types based on their energy storage method:

- ✚ Electrochemical double-layer supercapacitor (EDLC),
- ✚ Pseudocapacitor (PC),
- ✚ Hybrid Supercapacitor (HSC).

To better understand the classification of supercapacitors, a flow chart is provided below that lists the supercapacitor materials.

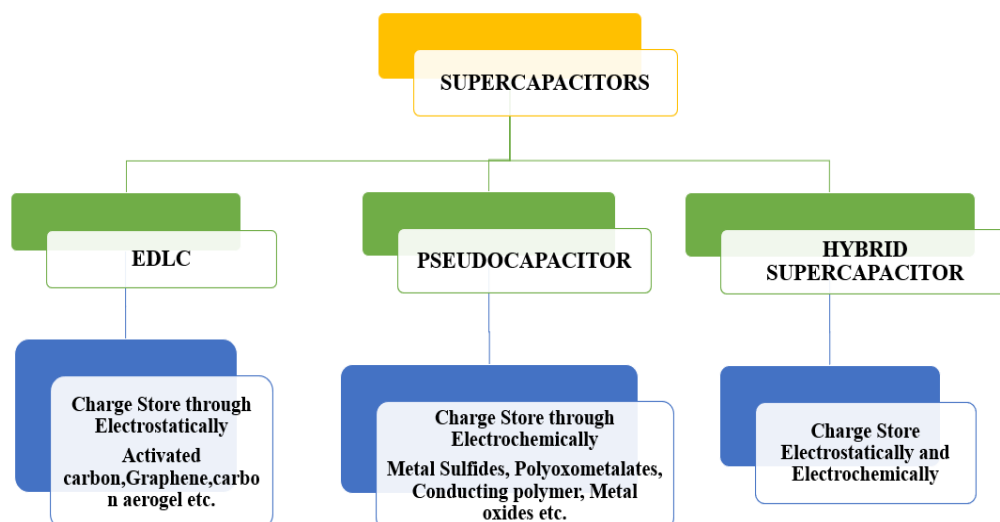


Figure 1.3: Taxonomy of supercapacitor.

1.3.1 Electric Double-layer supercapacitor (EDLC)

An electric double-layer supercapacitor (EDLC) functions through a mechanism that doesn't involve transfer of charge at the electrode-electrolyte boundary, known as a nonfaradic process. This type of supercapacitor relies on electrostatic storage, using the separation of ions will form a double layer at the interface between the electrolyte and electrode. When a supercapacitor cell is subjected to an external voltage, charge accumulation occurs on the electrodes, generating a voltage difference across the

electrolyte. This difference in potential drives the movement of ions toward electrodes of the opposite charge. At the same time, solvent molecules become polarized and attach to the electrode surface, which helps to prevent the recombining of these ions with electrodes. Consequently, an electrostatic double layer is established at the electrode surface. Each of these double layers operates like a traditional capacitor, with the oriented solvent molecules acting as the dielectric layer.(González et al. 2016). The specific capacitance of the electric double-layer capacitor was calculated by **Equation (1.2)**

$$C = \epsilon_0 \epsilon_r A / d \quad (1.2)$$

Where ϵ_r is the relative permittivity of the medium in the electrical double layer, ϵ_0 is the permittivity of the vacuum, A is the specific surface area of the electrode, and d is the thickness of the electric double layer (Zhi et al. 2013).

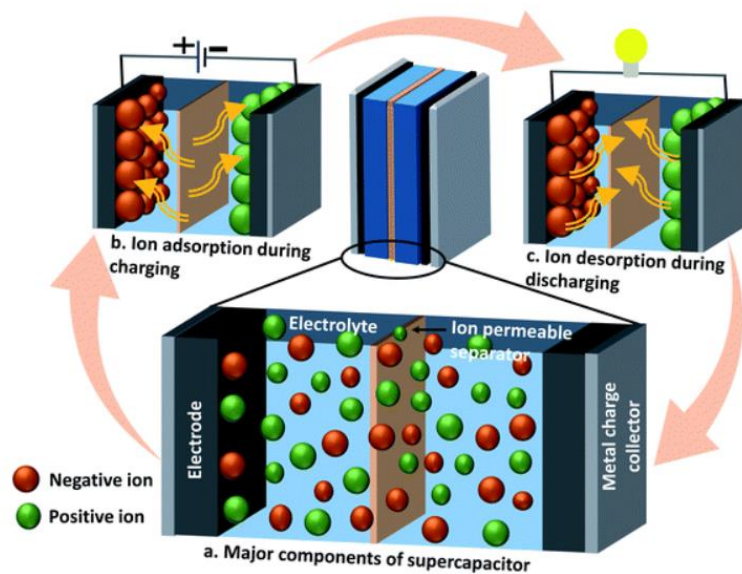


Figure 1.4: Mechanism of the electrochemical double-layer capacitor (Roy et al. 2021).

The Helmholtz model offers a straightforward explanation for the electric double layer by exploring how opposite charges disperse at the boundary of colloidal particles. This results in the formation of two layers of different charges at the electrode interface, separated by a distance of atomic order. The Gouy and Chapman model builds upon this explanation by introducing a constant distribution of cations and anions driven by

thermal motion in the electrolyte solution. However, this model has its limitations as it overestimates the capacitance by considering the point charge ion diffusion near the electrode surface. The Stern model combines the Helmholtz and Gouy-Chapman models and recognizes two distinct regions: the Stern and diffuse layers (Zhang and Zhao 2009). The Stern layer, also known as the adsorption layer, consists of two planes: the outer Helmholtz plane (OHP) and the inner Helmholtz plane (IHP). The outer Helmholtz plane is the distance from the electrode surface where the solvent molecules are highly oriented. In contrast, the inner Helmholtz plane is the distance where the specifically adsorbed ions come closest to the electrode surface. The Stern model provides a more accurate and detailed understanding of the electric double layer, making it an essential framework in electrochemistry medium (González et al. 2016).

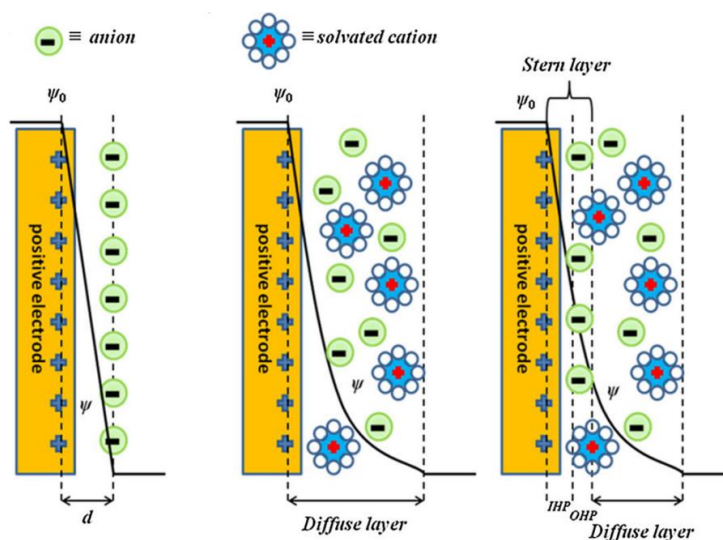


Figure 1.5: Schematic representation of EDLC formation (Davies and Yu 2011).

1.3.2 Pseudocapacitor

A pseudocapacitor is a type of capacitor that stores charge through faradic processes involving redox reactions that occur at or near the electrode surfaces. When an electric potential is applied to a system, the electrode material undergoes reduction and oxidation reactions, leading to the transfer of charge across the double layer and the generation of faradic current in the supercapacitor cell. The quantity of charge (q) stored is related to the electrode potential and the total faradic charge-discharge (Q) that the device undergoes. Pseudocapacitance can be identified by observing how the

charge-discharge (Q) varies with changes in the electrode potential, represented by the derivative dQ/dV . In contrast, the charge storage in an Electric Double Layer Capacitor (EDLC) is primarily based on surface charge accumulation without the involvement of chemical reactions. Meanwhile, in pseudocapacitors, it involves faradic in nature. Compared with the battery-type material, it involves faradic reactions occurring at a constant potential (Augustyn et al. 2014; Conway 1991; Conway and Pell 2003).

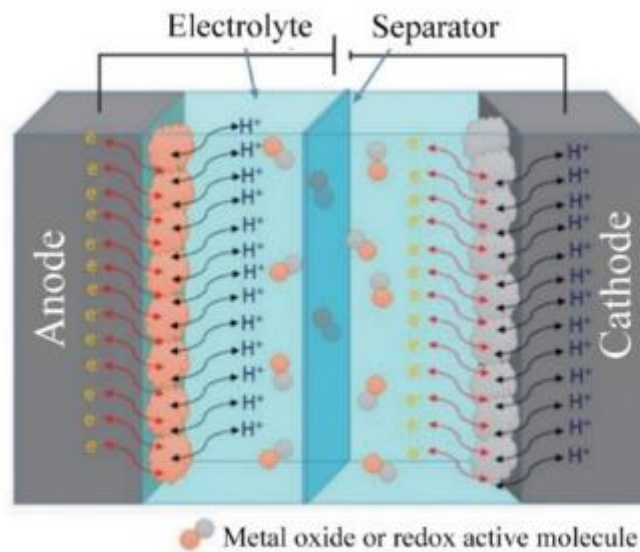


Figure 1.6: Schematic representation of Pseudocapacitors (Hossain et al. 2020).

1.3.3 Hybrid Supercapacitor

A hybrid supercapacitor is an advanced energy storage device that combines two types of capacitors: pseudocapacitor (PC) and electric double layer capacitor (EDLC) to achieve better performance (**Figure. 1.8**). The PC type utilizes faradic reactions, while the EDLC uses non-faradic reactions. By combining these two types, the hybrid supercapacitor overcomes the limitations of both types. It provides enhanced specific capacitance, energy density, and long cycle life without compromising the power density of the non-faradic type. To ensure a balanced charge-discharge process, choosing electrode materials of both types is crucial. The choice of electrode material

is crucial in achieving the kinetics of the hybrid supercapacitor. There are three types of hybrid supercapacitors, each with distinctive features and benefits.

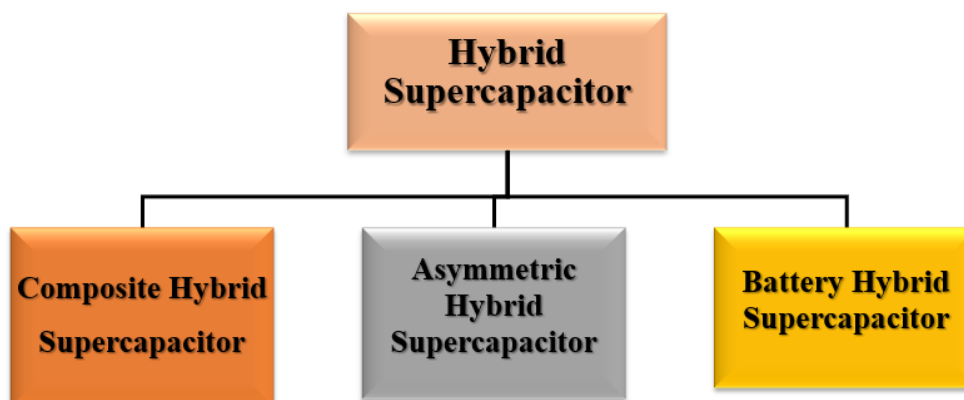


Figure 1.7: Classification of Hybrid Supercapacitor.

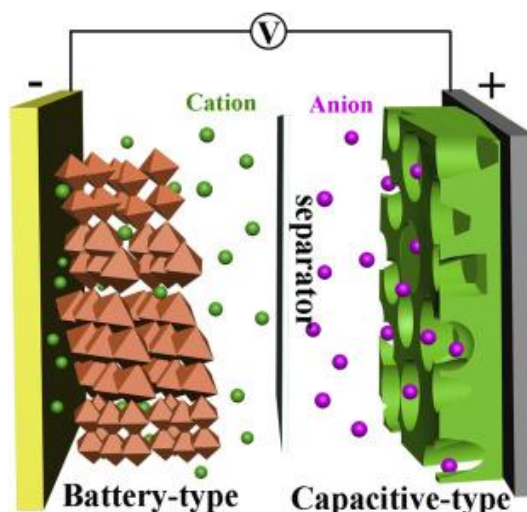


Figure 1.8: Schematic representation of Hybrid Supercapacitor (Liu et al. 2020).

(i) Composite Hybrid Supercapacitor

Composite electrodes have emerged as a highly promising development in energy storage. These electrodes are a breakthrough innovation combining Electric double-layer capacitors (EDLC) and pseudo-materials in a single electrode. Incorporating a conducting polymer or metal oxide material with a carbon material is the way to achieve a highly efficient energy storage solution. This solution provides both physical and chemical charge storage mechanisms in the same electrode. The composite electrode's carbon material plays a critical role in the overall effectiveness of this solution. It

enables the capacitive double layer of charge and provides a high surface area backbone, thus increasing the contact between the infused pseudocapacitive materials. This contact enhances the electrode material's capacitance.

On the other hand, the pseudocapacitive materials work to improve the electrode's specific capacitance further and expand the potential windows of the electrode material. This synergistic mechanism not only improves the corrosion stability of the electrode but also increases its overall effectiveness. In summary, composite electrodes offer a powerful and highly efficient solution for energy storage needs. They provide an innovative approach that integrates both physical and chemical charge storage mechanisms in a single electrode, making them a highly promising development in energy storage (K and Singh 2023; Low et al. 2019; Xue et al. 2017).

(ii) Asymmetric Hybrid Supercapacitor

Energy storage devices can achieve highly efficient electrode materials using faradic and non-faradic processes. Asymmetric hybrid supercapacitors combine electric double-layer materials like carbon with pseudocapacitor materials like metal oxides or conducting polymers. Typically, these supercapacitors have a positive electrode made of conducting polymer or metal oxide and a negative electrode made of carbon, which has a significant attraction towards the field. This balance of energy and power densities leads to superior performance compared to EDLC. Additionally, asymmetric hybrid supercapacitors have better cycling stability than similar symmetric pseudocapacitors (Laforgue et al. 2003).

(iii) Battery type Hybrid Supercapacitor

Battery-type hybrid supercapacitors and asymmetric hybrids are similar since they have two distinct electrodes. However, hybrids that combine battery and supercapacitor electrodes differentiate them from conventional hybrids. The demand for higher-energy supercapacitors is due to this configuration, which combines battery energy characteristics with supercapacitor power, cycle life, and recharge time. It is clear from the available experimental data that battery-type hybrids hold the potential to bridge the gap between supercapacitors and batteries, although there is less experimental data

available on them. Nevertheless, the full potential of these technologies must be determined through more research (Sharma and Chand 2023).

1.4 Brief overview of "Technical terminologies intricate in the supercapacitor"

1.4.1 Capacitance (C)

Supercapacitors are devices designed to store electrical energy through the combination of electric fields and electrostatic charges. Their storage capacity, known as capacitance, is the ratio of the electrical charge stored to the applied voltage, measured in Farads (F). This relationship is encapsulated by the **Equation (1.3)**.

$$C = Q/V. \quad (1.3)$$

To measure a supercapacitor's capacitance, the constant current discharge method is often utilized, which calculates capacitance based on the change in voltage over time during discharge, as shown by the equation (1.4).

$$C = (t_2-t_1)/(V_1-V_2) \quad (1.4)$$

This method assumes linear discharge behavior and uses the discharge current (I), discharge time (t), and the voltage difference (V_1-V_2).

1.4.2 Energy Density (ED)

Energy density refers to the amount of energy stored in a capacitor per unit of volume. Energy density in a capacitor, measured in watt-hours per liter (Wh L^{-1}) and per kilogram (Wh kg^{-1}), indicates the energy stored per volume or mass. The maximum energy (E_{max}) stored is calculated by the equation (1.5).

$$E_{\text{max}} = \frac{1}{2} C V^2 \quad (1.5)$$

where C is capacitance and V is the rated voltage. It's noted that capacitors can't be fully discharged to zero voltage; usable energy is calculated by discharging from the rated voltage to half of it, either at a constant current or power (Sarno et al. 2020).

1.4.3 Power Density (PD)

The speed at which energy is delivered or absorbed from the load is measured by power density. Power density is calculated either in kilowatts per kilogram (kW kg^{-1}) or kilowatts per liter (kW L^{-1}) by gravimetric or volumetric methods, respectively. The **Equation (1.6)** can be used to calculate the power density.

$$P = E/t_d \quad (1.6)$$

Where E is the cell's energy density (Wh kg^{-1}), and t_d is the discharge time in hours.

1.4.4 Coulombic Efficiency

Coulombic efficiency is used to calculate the efficiency of the supercapacitor device, which is defined as the ratio of discharging time and charging time at the same current densities. Coulombic efficiency is calculated by using the formula (1.7) given below:

$$\text{Coulombic Efficiency } (\eta) = \frac{\text{Discharge time}}{\text{Charging time}} \times 100 \quad (1.7)$$

1.4.5 Cycle Life

In supercapacitors, cycle life is crucial, with expectations of longevity even after thousands of cycles, although performance may slightly diminish. This durability largely holds for Electric Double-Layer Capacitors (EDLC) but is less certain for systems relying on faradic processes. The lifespan and performance degradation of supercapacitors depend on their construction, operating conditions, and particularly the choice of electrode materials. Lifespan testing involves charging and discharging at a set current within a predefined voltage range, often set to a fraction of the maximum rating. The supercapacitor's key metrics are periodically evaluated after numerous cycles, with a significant focus on any capacity reduction, typically ending the test if there's a 20-30% drop from the initial capacity. (Kotz et al. 2000).

1.5 Current Collectors

The active materials used in a supercapacitor cell may not conduct enough electricity. Current collectors can be added to the system to improve conductivity. These are essential functions of current collectors in electrochemical cells. They provide a

path for current to flow between the electrode and the power source and between the electrode and the external load. Another critical function is the dispersion of heat generated within the cell. They also play a role in the recharging process of the electrodes after use. It is interesting to note that different materials, such as aluminum, steel, iron, and alloys, can all be used as current collectors. Furthermore, current collectors have dual benefits for the cell. They not only have good electrical conductivity, but they also prevent the cell from chemical deterioration caused by the electrolytes (Lei et al. 2011; Wang et al. 2020).

1.6 Separator

A separator is a crucial factor for a supercapacitor device. It is used to prevent the transfer of electrons between two electrodes. To ensure device reliability, the separator should be mechanically robust and prevent the migration of electrons in the active material over time. The overall efficiency of a supercapacitor cell is influenced by the separator, and utilizing separators of poor quality can add additional resistance to the supercapacitor unit, or in extreme cases, cause the entire cell to short-circuit. Before selecting a separator, it should undergo essential characteristics such as being non-conductive, possessing excellent ion conductance, and having electronic insulating properties. It should also be chemically resistant, and the electrolyte should be able to wet it easily. Various materials, such as glass, paper, ceramic, and polymer-based separators, have been used as separators (Muzaffar et al. 2019a).

1.7 Electrolytes

Energy storage devices have a new promising solution in the form of supercapacitors. A vital role in determining several unique features of the device is played by the electrolyte. This includes cyclic stability, power density, energy density, equivalent series resistance (ESR), and potential window. To improve the quality of a supercapacitor, the electrolyte's properties must be carefully considered. The electrolyte should possess high conductivity, broad electrochemical stability, high thermal stability, a wide potential window, and low toxicity. High conductivity enables rapid charge and discharge cycles, while broad electrochemical stability allows high-voltage operation without degradation. A wide potential window is crucial in achieving a higher

voltage range, ultimately enhancing the supercapacitor's energy density. Low toxicity is critical in ensuring the safe operation and disposal of the device. Therefore, selecting the appropriate electrolyte is essential to achieving optimal performance and durability of a supercapacitor device (Saikia et al. 2020).

1.7.1 Aqueous Electrolyte

It is commonly utilized in supercapacitor (SC) applications because of its impressive specific capacitance and conductivity, which can reach as high as 1 S cm^{-1} . Due to their minimal pore size and atomic radius, these electrolytes readily engage with the electrode surface. When choosing a water-based electrolyte, it's important to take into account the size of both hydrated and unhydrated cations and anions. Additionally, the mobility of the charge carriers should be considered, as it influences the specific capacitance and the ionic conductivity. An aqueous electrolyte is easy to manage and requires no special conditions. However, their narrow potential window of around 1.2 V limits their use, reducing their energy density and specific capacitance. Aqueous electrolytes can be classified into three categories: acidic, basic, and neutral. Acidic electrolytes are excellent conductors of electricity, and 1M H_2SO_4 is the most commonly used acidic electrolyte. However, caution must be exercised when selecting the electrolyte and current collector due to the corrosive nature of acidic electrolytes. Basic electrolytes are non-corrosive, making them an ideal choice for low-cost metals like Ni^{2+} and Co^{2+} as the current collector. The most frequently utilized fundamental electrolyte is 6M KOH, which boasts a significant ionic conductivity of 0.6 S cm^{-1} . Other basic electrolytes like LiOH and NaOH can also be employed depending on the electrode materials. Neutral electrolytes are non-corrosive and have a broader potential window, making them a practical choice for SC use. Various electrolytes were used, like K_2SO_4 , KCl, LiClO_4 , Na_2SO_4 , NaCl, etc (Ramachandran and Wang 2018).

1.7.2 Non-Aqueous Electrolyte

Non-aqueous electrolytes, preferred for their wider voltage range (2.5 to 2.8 volts) and lower corrosiveness, enhance the energy and power density of supercapacitors. Commonly used organic electrolytes include triethylmethylammonium tetrafluoroborate (TEMABF_4), tetraethylammonium tetrafluoroborate (TEABF_4), and

spiro-(1,10)-bipyrrolidinium tetrafluoroborate (SBPBF₄), usually dissolved in solvents like acetonitrile. Despite their advantages, such as high energy and power densities, these electrolytes face limitations like poor conductivity, low capacitance, toxicity, flammability, and high cost, which restrict their widespread use. (Barzegar et al. 2015; Zhong et al. 2015).

1.7.3 Solid Electrolyte

In the current era, interest has grown in advancing electrochemical energy devices that utilize solid-state electrolytes. These electrolytes not only serve as ionic conductors but also function as electrode separators within the system. Compared to liquid electrolytes, solid-state electrolytes offer several benefits, including simplified packaging and fabrication methods for ESCs and the elimination of liquid leakage. Nonetheless, it is important to note that despite their potential, there has been limited research on inorganic solid materials, and most solid-state electrolytes developed for ESCs are still under the development stage (Kwon et al. 2018).

1.8 Electrode material

Supercapacitors store energy, but their energy storage characteristics assess their effectiveness. This limitation arises from the interaction between the internal structure of the electrode material, which is the critical determinant of supercapacitor properties. To achieve optimal energy storage characteristics, active electrode materials must have a large surface area and good electrical conductivity. There are two types of supercapacitors: electric double-layer capacitors (EDLCs) and pseudocapacitors. Carbon materials are the preferred electrode material for EDLCs since they do not interact with the electrolyte mechanism. In contrast, pseudocapacitors use metal oxides, conducting polymers, and other materials as electrode materials, which have been reported to be the most compelling electrode materials for enhanced electrochemical performance.

1.8.1 Electric double-layer capacitor

Carbon is an elemental constituent of life and an integral ecosystem component. It is abundantly available in nature in various forms, including the two primary allotropes,

diamond and graphite. Materials like carbon nanotubes, fullerenes, and graphene are derived from graphite carbon to develop sustainable energy sources, such as energy storage devices. In applications involving energy storage, carbon compounds are often used to support other substances, such as metal oxides and conductive polymers, due to the necessity for materials that possess high power density and extended cycle life. However, conducting polymers and metal oxides have limitations that impact their efficacy in these applications. Incorporating these materials over carbon material improves their performance and creates carbon nanocomposites with enhanced conductivity and cycle stability. Activated carbon, carbon nanotubes, carbon nanogel, and graphene are frequently utilized carbon materials for energy storage. These materials possess unique properties that make them appropriate for various energy storage devices. Activated carbon is highly porous, increasing its surface area and storing large amounts of energy. Carbon nanotubes have high electrical conductivity, which makes them suitable for high-performance batteries. Graphene has excellent mechanical strength and can be employed in flexible energy storage devices. Carbon and its derivatives are critical in ensuring a sustainable energy future. Activated carbon is widely recognized as the best choice among various carbon materials due to its exceptional characteristics, such as larger surface area, higher pore volume, and cost-effectiveness (Sevilla and Mokaya 2014; Zhai et al. 2022).

AC is a non-graphitic carbon that has a highly disordered microstructure. Unlike crystalline graphite, AC contains more interlayer space and irregular arrangement in the aromatic sheet stacks. Compared to interlayer spacing, the graphite spacing is 0.335 nm, whereas AC has a difference between 0.34 and 0.35 nm. AC has a microcrystalline structure, which will be harder due to the strong cross-linking between the crystallites. This is due to the presence of oxygen in the raw material, which shows a well-developed micropore structure. AC has high adsorption capacity due to its porous characteristics. The characteristics of porosity are primarily influenced by factors such as the size of the pores, the volume of pores, the distribution of pore sizes, and the overall surface area. In applications involving energy storage, particularly during charging and discharging, the broad distribution of pore sizes in AC significantly boosts its electrochemical efficiency. Macropores, which are 50 nm or larger, act as reserves for

ions for both mesopores and micropores. Mesopores, with sizes ranging from 2 to 50 nm and also referred to as transition pores, facilitate effective diffusion of ions, whereas micropores, smaller than 2 nm, are utilized for charge storage. Within porous carbon, these various pore sizes are interconnected, enabling the smooth movement of electrolyte ions through the channels. Traditionally, AC has been prepared from mineral precursors like coal, peat, wood, and coconut shells. However, due to concerns about the environmental impact, sustainability, and the finite nature of these resources, researchers have indeed shifted towards biomass feedstocks to produce AC. Biomass feedstocks such as agricultural residues, wood waste, and various plant materials offer a more sustainable and renewable source for activated carbon production. Using biomass helps reduce the dependence on non-renewable resources and aligns with the principles of green and sustainable chemistry. Therefore, the shift towards biomass feedstocks for AC production is a trend in the field, driven by both environmental considerations and the desire for more sustainable practices in material synthesis. The AC derived from biomass features an interconnected, multi-channeled, and porous architecture, essential for the development of superior supercapacitors (“Crystallite growth in graphitizing and non-graphitizing carbons” 1951; Harris et al. 2008).

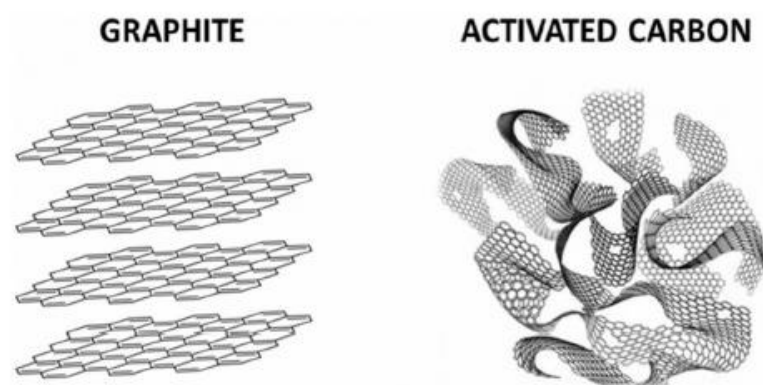


Figure 1.9: Crystal lattice in three dimensions of Graphite and Activated carbon (Harris et al. 2008).

1.8.1.1 Biomass-derived Activated carbon (BDAC)

AC is a versatile material used in numerous applications, from water and air purification to energy storage and catalysis. Traditionally, coal has been the dominant precursor for preparing activated carbon because it contains a high carbon percentage and is cost-effective. However, coal is a finite fossil fuel, and its depletion is inevitable. In recent years, researchers have shifted their attention to preparing AC from biomass-derived raw materials (**Figure. 1.10**), which are renewable, abundant, and environmentally friendly. Biomass encompasses organic materials derived from plants or animals, such as wood, agricultural waste, and food scraps. Employing biomass as a precursor for AC production offers several advantages. Firstly, it is a renewable and inexhaustible source of raw materials. Secondly, biomass can be obtained from various sources, including waste products, which can be converted into valuable products, thereby reducing waste management issues. This shift towards renewable and sustainable sources of raw materials is essential to address the environmental challenges the world is facing today for a sustainable future (Dubey et al. 2020).

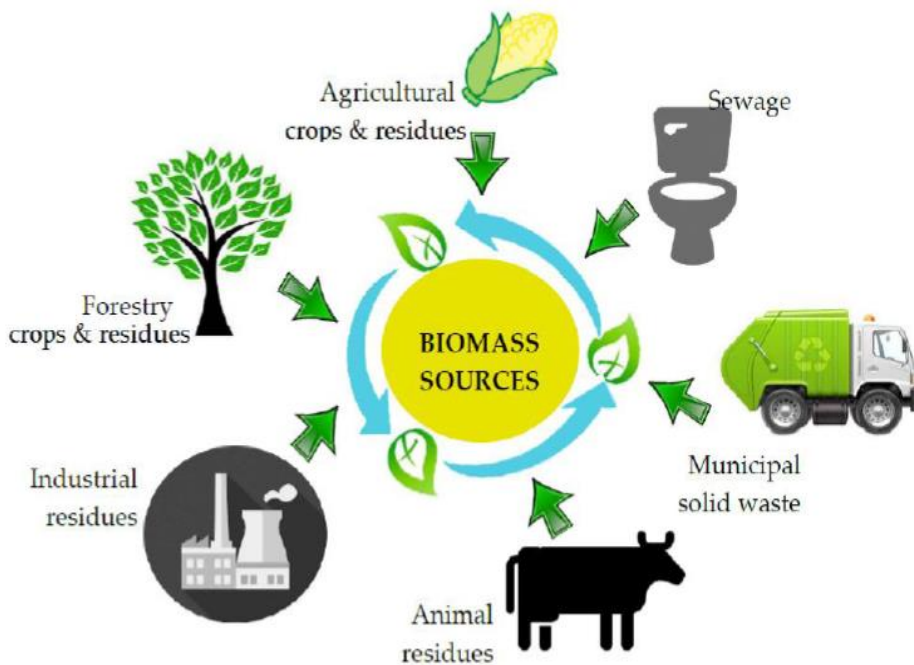


Figure 1.10: Different types of biomass feedstocks (Bedia et al. 2018).

1.8.1.2 Synthesis of Biomass-derived activated carbon

Recycling biomass waste into AC involves two main processes: carbonization and activation. In the carbonization step, the thermal conversion method breaks down the biomass feedstock and removes all elements except carbon. This step ensures that the resulting AC has a high carbon content. Enhancing the active surface of the carbon, increasing its specific surface area, and expanding its pore volume during the activation step can improve its ability to adsorb impurities. There are various carbonization and activation techniques that can be employed to create activated carbon from biomass waste. These processes are illustrated in **Figure. 1.11** and involve different methods of heating, cooling, and activating the carbon. By recycling biomass waste into AC, we can effectively reduce waste and provide a sustainable solution for various applications, such as air and water purification, gas storage, and energy storage.

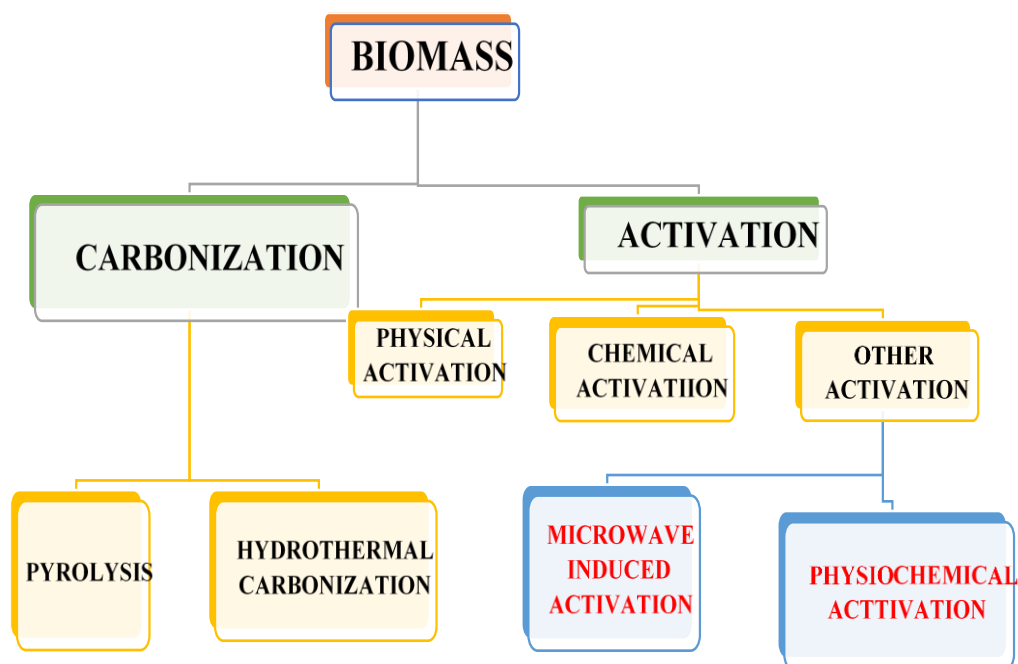


Figure 1.11: Schematic representation of synthesis of biomass-derived activated carbon.

1.8.1.3 Carbonization

(i) Pyrolysis

The pyrolysis process involves the thermal decomposition of biomass feedstock into charcoal, bio-oil, and gases. This transformation occurs at high temperatures and in an inert atmosphere, ensuring that oxygen is absent to facilitate the process. For converting biomass feedstock into charcoal at an industrial maximum, they preferred the pyrolysis process. In biomass feedstocks, three main constituents, like cellulose, hemicelluloses and lignin, were present. Thermal gravimetric analysis was undergone to understand the decomposition stages of biomass materials. This will undergo three stages: the first stage will be the pre-carbonization step, at this stage, the temperature will be between 120 to 200 °C. At this initial phase, only a slight reduction in weight is expected as it involves some internal changes like the breaking of bonds and the emergence of free radicals. This process leads to the formation of carbonyl groups through the release of water, carbon monoxide, and carbon dioxide. Following this, the primary step of pyrolysis occurs where there's a substantial decrease in weight due to the decomposition of solids. The last phase involves the ongoing devolatilization of char, resulting from the breaking of C-H and C-O bonds (Zhang et al. 2010).

(ii) Hydrothermal Carbonization

Hydrothermal carbonization is a process that was initially discovered in 1913 by Bergius and then further developed by Berl and Schmidt in 1932. The process involves transforming biomass material into carbonaceous material using mild conditions. This is done by heating the biomass feedstocks in an aqueous medium in a closed container at a specific temperature, typically in the range of 130 °C to 250 °C, for about 2 to 24 hours. Following this, the resulting solid product is retrieved through filtration, washed with distilled water, and dried at 120 °C for four hours (Bagheri et al. 2015; Hu et al. 2010).

1.8.1.4 Activation Method

The activation process is vital in optimizing biochar's porosity, which helps eliminate any disruptive regions or blockages by breaking down volatile substances. The porosity achieved primarily depends on the characteristics of the biomass source,

along with the specific carbonization and activation techniques used. These techniques involve physical, chemical, and physiochemical methods that merge both physical and chemical methods and a microwave-induced approach (**Figure. 1.12**) (Reza et al. 2020).

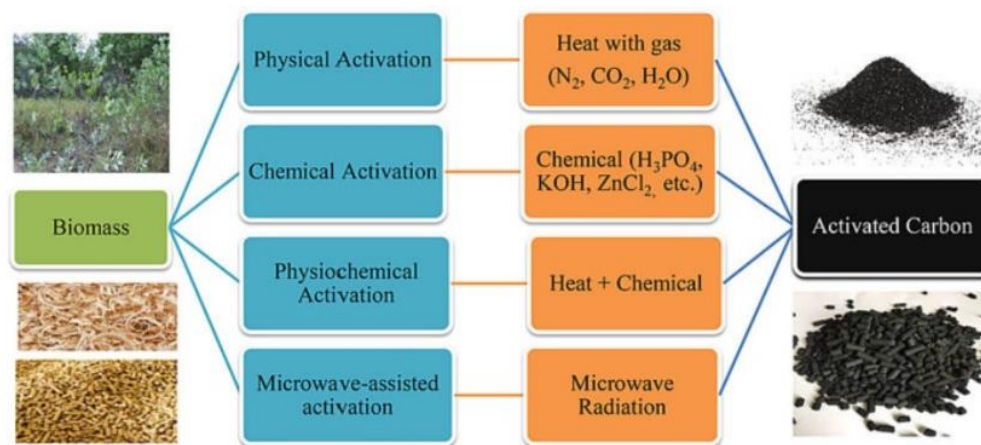


Figure 1.12: Schematic representation of types of Activation methods (Reza et al. 2020).

(i) Physical activation method

AC derived from a carbon precursor material involves two crucial steps in the physical activation process. The first step is pyrolysis, where the material is subjected to a high-temperature range of 400-900 °C in an inert atmosphere, causing volatile compounds to be removed and solid residue to remain. The second step is gasification, where the solid residue is partially gasified using an oxidizing gas like air or oxygen at a temperature range of 350-1000 °C (Dawson et al. 2003; Yang et al. 2018).

During gasification, the oxidizing gas reacts with the remaining products from the pyrolysis step, thus opening some closed pores within the material and resulting in a microporous structure that allows for the release of CO and CO₂ gases, producing activated carbon. The quality and properties of the AC, including its porosity, surface area, and type of oxygen groups present, depend on various factors such as the carbon precursor material used, the oxidizing agent employed during gasification, and the degree of activation and temperature.

Using oxidizing agents like air or oxygen during the activation process leads to an exothermic reaction that produces a lot of heat. However, controlling the process can

be difficult due to the reaction's speed, which may cause excessive burn-off and reduce the AC yield. To ensure energy efficiency and cost-effectiveness, high reactivity of oxygen is preferred over other oxidizing agents like steam or carbon dioxide due to its high reactivity. Factors like biochar pore size distribution, activation times and temperatures also influence the physical and chemical nature of the activated carbon (Sevilla and Mokaya 2014).

(ii) Chemical Activation method

The chemical activation method is a highly efficient technique that involves using an inert gas atmosphere to pyrolyze a biomass feedstock at high temperatures ranging from 300 to 550 °C. The resulting biochar is then mixed with chemical activators and subjected to high temperatures in the same inert gas environment. The chemical activation method has several advantages over other activation methods. It shortens the activation period and simplifies reaction control while increasing specific surface area and enhancing pore volume (Heidarinejad et al. 2020; Osman et al. 2021; Suárez and Centeno 2020).

The activating agents used in this method are classified into three groups: alkaline, neutral, and acidic. The alkaline agents include KOH, NaOH, K₂CO₃, K₂SiO₃, and Na₂CO₃. The neutral agents include ZnCl₂, FeCl₃, KCl, MgCl₂, and KMnO₄. Finally, the acidic agents include H₃PO₄ and H₄P₂O₇. These agents penetrate deeply into the carbon structure and enhance porosity. Several factors significantly affect the process, including the impregnation ratio of biochar to activators, temperature, atmospheric conditions, and the type of biomass feedstock. ZnCl₂, H₃PO₄, and KOH are the preferred activators. KOH acts as an oxidant, while ZnCl₂ and H₃PO₄ act as dehydrating agents. Dehydrating agents reduce particle dimensions, remain in the pores during thermal treatment, and act as templates for microporosity creation. ZnCl₂ leads to fewer micropores, while KOH, acting as an oxidant, undergoes a redox reaction with carbon to generate pores. This etches the carbon framework, generating pores through oxidation and intercalation, with subsequent removal during washing steps. The generation of CO₂ from the breakdown of K₂CO₃ at temperatures exceeding 700 °C aids in increasing porosity by means of carbon gasification. (Gao et al. 2020; Luo et al. 2022).

The quantity of activating agents used in the process affects porosity development, with higher amounts resulting in greater porosity (surface area and pore volume) and a broadening of the pore size distribution (PSD). Porosity development initially focuses on microporosity, becoming more heterogeneous with increasing activating agent quantity. The nature of the activating agent influences the heterogeneity, as observed in studies using KOH, ZnCl₂, and H₃PO₄. The activation temperature significantly influences porosity, with the ideal temperature varying based on the activating agent and the type of carbon used. As the temperature increases, porosity initially rises, reaching a peak before it starts to decline due to the structure shrinking or collapsing at higher temperatures. For activating agents like ZnCl₂ and H₃PO₄, which lack strong thermal stability, there's a noticeable breakdown and reformation of carbon structures, leading to the shrinking or collapse of pores. Conversely, when using KOH, optimal porosity is observed at elevated temperatures (700–900 °C), indicating that the cross-linking reactions facilitated by KOH activation are more resistant to heat. This is attributed to the formation of micropores as a result of volatile substances being released between 500 to 800 °C (Jin et al. 2018; Salitra et al. 2000; Wang et al. 2013).

When the temperature goes beyond 800 °C, CO₂ is released from K₂CO₃ created during carbonization, leading to carbon gasification, which causes the opening up of closed pores and the enlargement of existing micropores. This event results in a broadening of the PSD. Moreover, metallic potassium is generated, which then intercalates within the graphite-like laminar structure, creating wider spaces between carbon atomic layers and increasing the pore volume. KOH is a favored activating agent because it facilitates the synthesis of activated carbons with narrow PSD and high surface areas of up to ~4000 m² g⁻¹. Different parameters, such as the mixing process, activation time, gas flow rate, type of gas during heat treatment, and heating rate, can affect the development of porosity. By controlling the activating conditions, it becomes possible to adjust the PSD of KOH-activated carbons (Elmouwahidi et al. 2017; Han et al. 2022; Luo et al. 2022; M. Malarvizhi et al. 2019). Chemical activation has the following advantages compared to the physical activation method:

- (1) the pores are well developed, and pore size is controllable
- (2) materials with a high surface area are produced

(3) yield carbon is high

(4) it has a lower pyrolysis temperature

1.8.2 Polyoxometalates

Polyoxometalates (POMs) are an intriguing class of anionic polynuclear inorganic metal oxygen clusters with unique nanoscale structures and properties. POMs consist of early transition metals such as vanadium (V), tungstate (W), and molybdenum (Mo), as well as less frequently used metals like niobium (Nb), tantalum (Ta) and palladium (Pd). These polyanion complexes are characterized by octahedral structures of metal-oxygen (MO_6) corner-sharing, edge-sharing, and face-sharing. The oxides act as a ligand and coordinate with a metal atom to give a bridged framework. The remarkable redox properties of POMs are closely related to their structure and composition. There are currently dozens of different structural types and stoichiometries of POMs known to date. Polyoxometalates (POMs) can be categorized based on their chemical composition into two main groups: isopolyanions, denoted as $[\text{M}_m\text{O}_y]^{p-}$, which occur when the POM structure does not include any heteroatoms (Lindqvist type), and heteropolyanions, represented as $[\text{X}_x\text{M}_m\text{O}_y]^{q-}$, the presence of one or more heteroatoms within the structure, which include Keggin, Wells-Dawson, Anderson-Evans, and Dexter-Silverton types. The addenda atom M in POMs contains its highest oxidation state (d^0 , d^1), such as Mo^{+6} , W^{6+} , V^{5+} , etc., while X is the heteroatom located in the center of the polyanion, which can include elements such as P^{5+} , Si^{4+} , As^{5+} , Ge^{4+} , etc. POMs are multimetal oxide clusters composed of early transition elements that can be altered in shape, size, and composition. They are non-toxic, non-volatile, and have a relatively large molecular size and weight. Due to their unique structures and physicochemical properties, such as tunable structural compositions, rich redox chemistry, and precise atomic structures, POMs have emerged as promising materials for various multidisciplinary applications, including sensors, catalysis, optics, magnetism, medicine, and energy storage, etc. (as shown in **Figure. 1.14**)(Anderson 1937; Evans et al. 1975; Genovese and Lian 2017; Kozhevnikov 2002; Pope and Müller 1991).

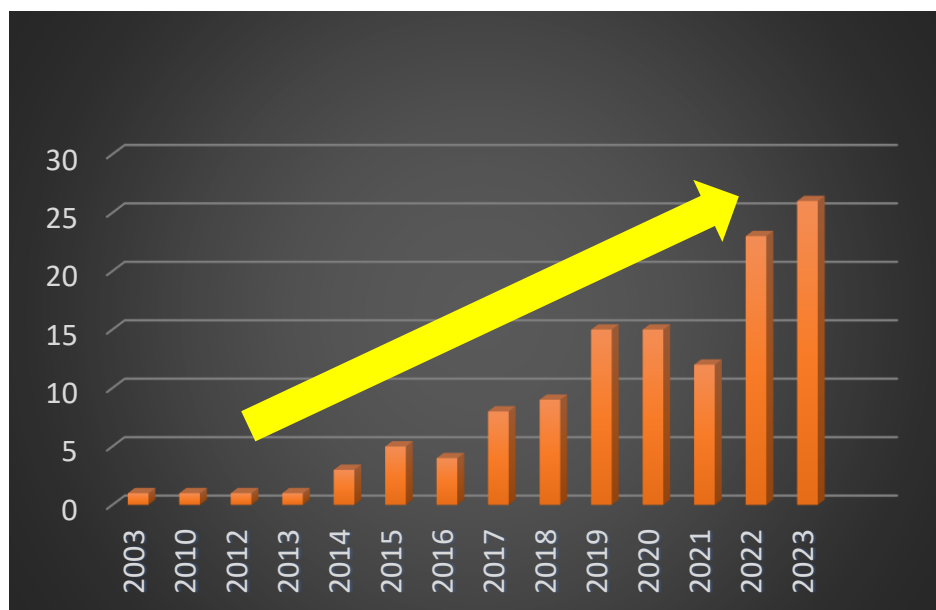


Figure 1.13: Graphical representation of Polyoxometalates material in supercapacitor year-wise (Source Scopus).

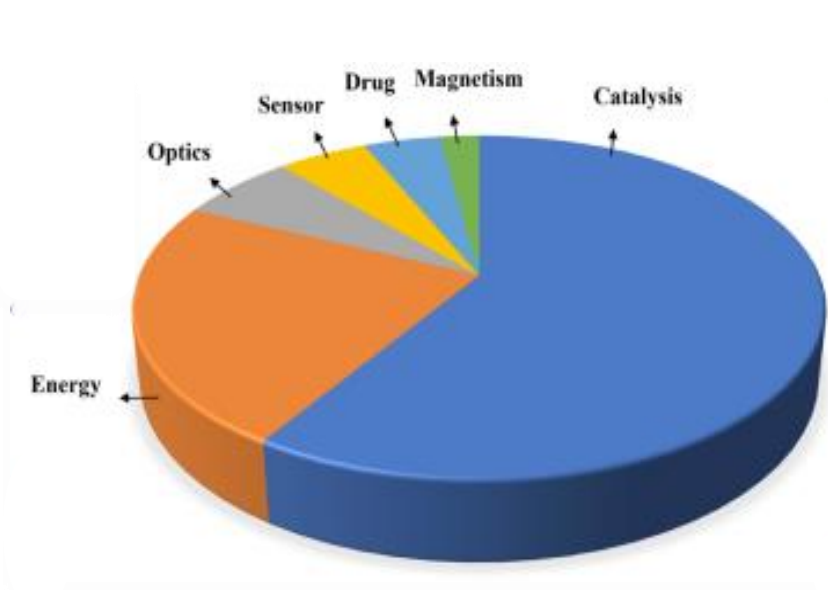


Figure 1.14: Pie chart representation of Polyoxometalates based material in different applications (Khalilpour et al. 2021).

1.8.2.1 Formation of Polyoxometalates

POMs are complex structures that are formed through a process of condensation or self-assembly. Oxyanions such as MO_4^{2-} will undergo condensation under specific conditions, such as pH, concentration, and temperature. This leads to a process of polycondensation, which results in the formation of even more complex structures known as polyanions.



Scheme 1.1: Schematic representation of the formation of Polyanions.

Isopolyanions (IPA) are formed when similar species of $\text{M} = \text{Mo}, \text{W}, \text{Nb}, \text{Ta}, \text{etc.}$, with oxygen (MO_4) undergo condensation. On the other hand, heteropolyanions (HPA) are formed when the addenda atom with oxygen occurs around a heteroatom, which is $\text{X} = \text{Si}, \text{P}, \text{As}, \text{Ge}$, and undergoes the condensation reaction. The kinetic forms of heteropolyanions are mainly composed of the stoichiometry of the addenda atom and heteroatom, which plays a vital role in the structure of polyanions. Mineral acids like HCl and H_2SO_4 are typically used in the acidification process of polyanion synthesis. Heteropolyanions like Keggin and Wells-Dawson are stable enough to allow crystallization from an aqueous solution, and the stability of the Polyoxometalates is generally measured by their ability to retain their structural identities and avoid degradation in other forms. Hence, this thesis primarily focuses on Keggin and Wells-Dawson based POMs for energy applications (Ammam 2013; Gumerova and Rompel 2018; Hill 1998; Song 2018).

1.8.2.2 Keggin Polyoxometalates

In 1926, Berzelius discovered a yellow precipitate that forms when an excess of ammonium molybdate $(\text{NH}_4)_2\text{MoO}_4$ is added to phosphoric acid H_3PO_4 . Although the precipitate was identified as $(\text{NH}_4)_3[\text{PMo}_{12}\text{O}_{40}] \cdot x\text{H}_2\text{O}$ as a heteropoly compound, Berzelius was unable to characterize this compound fully. In 1929, Pauling proposed a

structural hypothesis to understand the composition of heteropoly ion clusters that are shared metal-oxygen polyhedra. Later, in 1933, Keggin was able to solve the crystal structure of $\text{H}_3[\text{PW}_{12}\text{O}_{40}]\cdot 5\text{H}_2\text{O}$ using single powder X-ray diffraction (Keggin 1933). These Keggin structures and some of their derivatives are highly important for energy storage applications. Its structures have a general formula of $[\text{XM}_{12}\text{O}_{40}]^{x-8}$, where X is the heteroatom (P, Si, Ge, As, etc.), and M is the addenda atoms (W, Mo, V, etc.). It consists of a primary heteroatom at its center, surrounded by four oxygen atoms that form a tetrahedral unit (XO_4). The heteroatom is caged by twelve octahedral MO_6 units of addenda atoms, connected by a common edge to give rise to four M_3O_{13} units. The entire structure contains 40 close-packed oxygen atoms, which are of four types: twelve terminal $\text{M}=\text{O}$, twelve edge bridging $\text{M}-\text{O}-\text{M}$, twelve corner-bridging $\text{M}-\text{O}-\text{M}$, and four terminal $\text{X}-\text{O}-\text{M}$ (Kamiya et al. 2013; Kozhevnikov 2002). The basic structure, known as $\text{XM}_{12}\text{O}_{40}$, can be transformed into lacunary POMs by treating it with an alkaline solution under controlled experimental conditions, such as pH, temperature, and concentration. This transformation leads to the loss of one or more metal atoms. If a single metal atom is lost, the resulting formula is $\text{XM}_{11}\text{O}_{40}$, while losing three metal atoms results in the formation of XM_9O_{40} . The other transition metals, M' , can be filled with lacunary POMs, resulting in stable Keggin POMs like $\text{XM}_9\text{M}'_3\text{O}_{40}$ (Figure. 1.15) (Ammam 2013; Du et al. 2013).

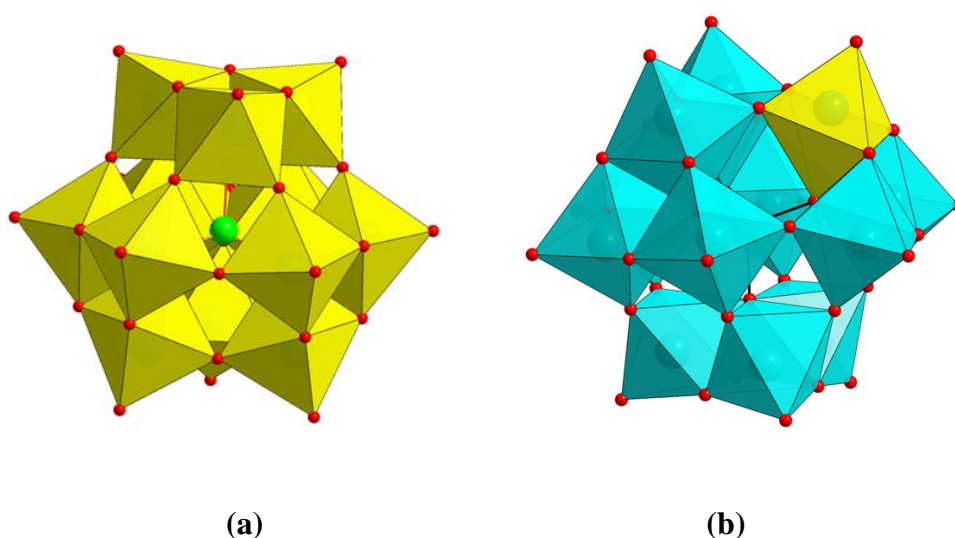


Figure 1.15: a) Keggin ($\text{XM}_{12}\text{O}_{40}$) b) Different addenda atom substituted Keggin POMs ($\text{XM}_{11}\text{M}'\text{O}_{40}$).

1.8.2.3 Wells-Dawson Polyoxometalates

In 1945, Wells-Dawson proposed a structure that is widely known as the Wells-Dawson POMs. Later, in 1953, this structure was confirmed by Dawson by proposing the structure of $\alpha\text{-K}_6\text{P}_2\text{W}_{18}\text{O}_{62}\cdot 14\text{H}_2\text{O}$. This structure is composed of two Keggin fragments that are linked together through the sharing of oxygen ligands at the corners. The Wells-Dawson POMs structure is characterized by an 18:2 ratio of the metal atom (M) to the heteroatom atom (X). This is generally represented by the formula $[\text{X}_2\text{M}_{18}\text{O}_{62}]^{2x-16}$, where M is Mo^{6+} or W^{6+} and X is P^{5+} or As^{5+} etc. The belt of twelve addenda is formed by joining two M_3O_{13} groups via corner-sharing of oxo ligands. In **Figure. 1.16**, it is shown that the hetero-anion, $[\text{XO}_4]^{n-}$, is attached to the three metals of a M_3O_{13} cap and six of the belt octahedra. (Briand et al. 2003; Dawson 1953). Like Lacunary Keggin type, lacunary Dawson is also possible by partial degradation in suitable alkaline treatment in a proper condition. In lacunary Dawson POMs, one or more vacant sites could be removed by removing the MO_4 . Then, according to the availability of vacant sites, the different metal oxides were incorporated over the lacunary Dawson POMs (**Figure. 1.17**) (Ueda et al. 2015; Ammam 2013; Mbomekalle et al. 2004).

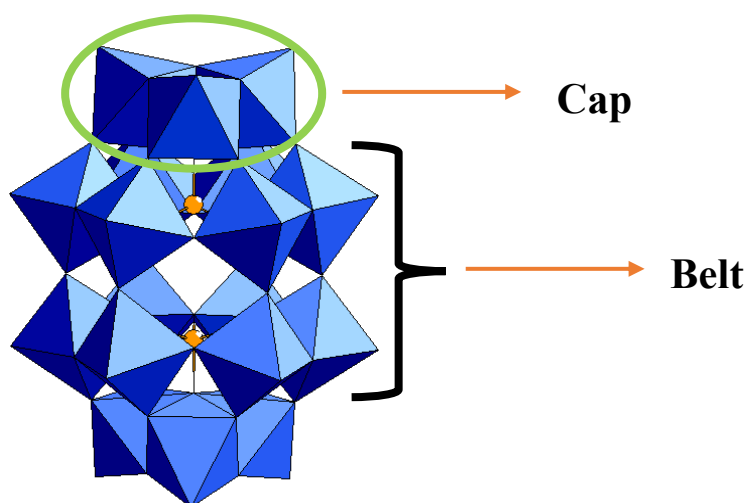


Figure 1.16: Graphical view of positions of Wells-Dawson POMs.

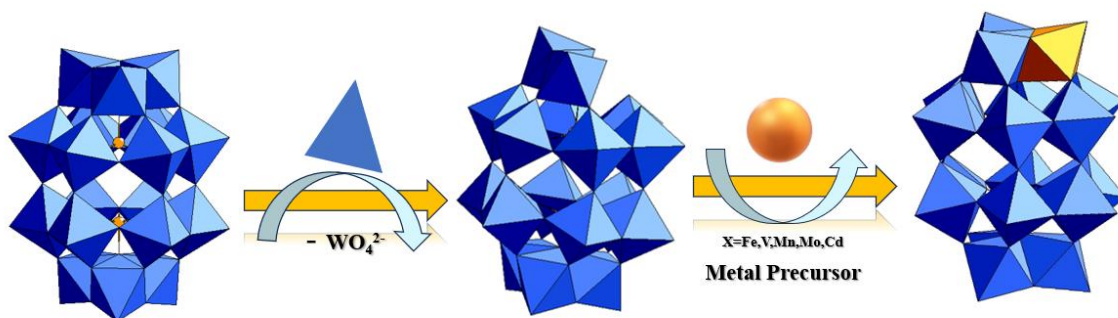


Figure 1.17: Plausible mechanism representation of changing parent POMs into lacunary POMs species and inserting different metal atoms.

1.8.2.4 Properties

Polyoxometalates (POMs) are commonly used in electrochemistry and catalysis due to their unique properties. However, their solubility is a crucial characteristic that varies significantly based on various factors like environment, structure, and chemical composition. Some POMs are highly soluble in polar solvents like water or alcohol. To modify the solubility of POMs, chemical modification can be used, which involves changing counterions or adding organic ligands. This modification is crucial for solution-phase reactions as dissolved POMs play a vital role in catalysis, redox, and self-assembly reactions. Solubility is also important in electrochemical applications as it influences the selection of solvent and electrolyte systems and the types of electrodes used. Understanding the variables that affect POMs solubility is crucial for determining the material's stability. Thus, considering solubility along with other important properties is essential for a better understanding of POMs and their range of applications (Kozhevnikov 2002). POMs display a wide range of chemical properties when it comes to redox reactions. It is interesting to note that these POMs undergo frequent reversible reduction-oxidation reactions, leading to the formation of mixed valence species that retain the structure of the parent oxidized anion. Due to their easy reversible redox reactions, these heteropoly compounds are of great significance in the field of electrochemistry (Pope et al. 2013; Pope and Müller 1994).

1.9 Applications

In recent times, energy storage applications have been significantly impacted by the availability of energy sources. This has opened up endless opportunities for electrochemical energy devices such as batteries and supercapacitors. Supercapacitors have advantages over batteries, such as better cycle life and power density. They can improve the performance of applications from portable electronics to hybrid electric vehicles. Researchers are working on developing supercapacitor devices with better performance and lower costs. The following are some of the various applications of supercapacitor devices that have been discussed (Muzaffar et al. 2019).

1.9.1 Public sector applications

The demand for user-friendly applications has grown with civilization's progress. Researchers have developed various devices, including those by Maxwell Technologies, which manufactures remote control products using supercapacitors. These devices, found in digital cameras and portable speakers, offer quick charging times and are utilized in memory backup and actuator applications. Supercapacitors also stabilize wind and solar power sources, control wind turbine blades, and power airline cable car systems. In Japan, supercapacitors coupled with solar energy are used in LED lamps, providing an eco-friendly energy solution. Additionally, Coleman Company Inc. has introduced a cordless screwdriver powered by supercapacitors, offering rapid charging and efficient operation compared to batteries (Muzaffar et al. 2019; Cameron 2012).

1.9.2 Military and Defence application

Hybrid supercapacitors have become increasingly popular as a power source for various devices such as navigators, sensors, and communication tools. They are also used to operate more complex devices like radar systems, electromagnetic pulse weapons, torpedoes, and other military equipment. In order to power applications that require high power density, such as phased array radar antenna, avionics display gadgets, airbag deployment, and missiles, a fit assemblage of hybrid supercapacitors is needed. The Tecate group of companies is a significant supplier of supercapacitor devices for defense and military applications (Muzaffar et al. 2019).

1.9.3 Transport and Automobiles application

In the transport and automobile sectors, electrochemical energy storage systems are used for several applications, such as ignition, security, lighting, start-up, and transmission. Hybrid supercapacitors are now widely used in internal combustion engines and electric vehicles. They provide energy for starting up the engine and power the fuel-saving mechanism, resulting in faster acceleration. This integration reduces maintenance costs and increases lifespan compared to batteries. Companies like Toyota follow this strategy. Nowadays, electric buses in China run on hybrid supercapacitors with charging capacity made of AC with Ni (OH)₂. Not only buses, but tram cars also use electric double-layer capacitor arrangements with a charging time of 30 seconds for 3-5 km. The primary goal of making hybrid supercapacitor buses is to reduce the heat energy emitted while the engine runs, but the vehicle is still at a halt. This will help save the environment by limiting the emission of CO₂ (Miller and Burke 2008; Park et al. 2016; Bian et al. 2017).

1.9.4 Memory backup chips

Hybrid supercapacitors have become increasingly popular in electronic devices as memory backups, as they guarantee power stability and provide emergency power during shutdowns. They are superior to traditional UPS systems in terms of safeguarding against voltage drops and are crucial for seamless operations in solid-state drives. By enabling cache cleansing and smooth shutdowns during power outages, they prevent data loss and ensure uninterrupted performance. (Chen and Xue 2016; Endo et al. 2001).

1.9.5 Medical and industrial application

In the medical field, technology has made tremendous advancements. We now have well-equipped devices to solve various health problems. Hybrid supercapacitors play a significant role in the medical field, as they can serve as a high voltage pulsed delivery application. They are commonly used in defibrillators, which help in cases where the heart's rhythm becomes unstable. It provides instant energy to the zap, helping to restore the proper heart rhythm. These are also used in other fields like dental

sciences and serve as backup sources for medical imaging equipment and ventilators. In the industrial sector, they are widely used in industrial electronics, such as automated meter readings and emergency power backup sources (Wang et al. 2016).

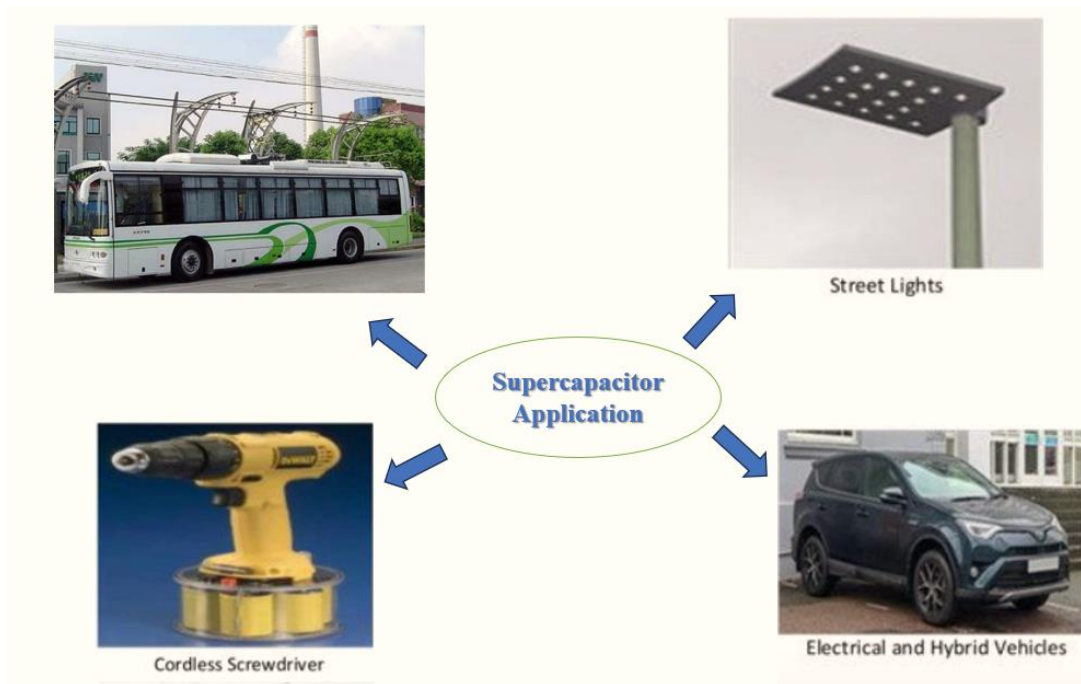


Figure 1.18: A diagrammatic illustration of the fundamental structure of a supercapacitor device and its multiple applications as an energy storage (Şahin et al. 2022).

CHAPTER 2



Literature Review

2.1 Literature Review

There has been a growing interest in using pseudocapacitor materials, particularly Polyoxometalates (POMs), to enhance the specific capacitance of electrochemical double-layer capacitors (EDLCs). POMs has been doped or infused into EDLC materials to achieve this, forming nanohybrids. These nanohybrids enhance specific cell capacitance without compromising other essential device parameters such as energy and power densities. However, POMs alone cannot be used as an electrode material due to its low conductivity and leaching properties. POMs has been doped with EDLC material, specifically in activated carbon, to overcome these issues and make nanohybrids. This section will discuss using POMs-impregnated activated carbon nanohybrids as electrode materials.

In 2012, Ruiz et al. explored supercapacitor cells with activated carbon and PMo_{12} phosphomolybdate. The prepared electrode material was tested in 1M H_2SO_4 electrolyte solution. The specific capacitance was achieved at 183 F g^{-1} at a current density of 2 A g^{-1} for AC- PMo_{12} , which is 29% higher than the unmodified AC substrate.

In 2014, Ruiz et al. developed hybrid electrodes using a combination of Phosphotungstic acid ($\text{H}_3\text{PW}_{12}\text{O}_{40}$ or PW_{12}) and activated carbon (AC). These electrodes have been found to be highly durable and produce superior performance in aqueous supercapacitors. The combination of double-layer and redox activity increased specific capacitance by 254 F g^{-1} at 10 mV s^{-1} .

In 2015, Mu Anqi et al. discovered the potential of using AC and Wells-Dawson Polyoxometalates (P_2Mo_{18}) as an electrode material for supercapacitors. They conducted electrochemical studies on this material and found that it exhibited a specific capacitance of 275 F g^{-1} at a current density of 6 A g^{-1} . Furthermore, they assessed the material's cycle stability, finding that it maintained an excellent capacitance retention of 89% even after 2000 cycles.

Chenchen Hu et al. (2016) developed a new type of hybrid nanocomposite material by combining the properties of EDLC and pseudocapacitor. This hybrid material has high energy density, high power density and long cycle life by incorporating the Polyoxometalates redox material into activated carbon. The nanocomposite electrode material was tested in an aqueous electrolyte solution of ionic liquid, which resulted in the highest capacitance of 223 F g^{-1} at 1 mV s^{-1} . Moreover, it shows good capacitance retention of 10000 cycles.

In 2017, Mathew et al. synthesized Polyoxometalates-loaded pinecone shell-derived activated carbon for hybrid electrochemical applications. The pinecone shell was first cleaned and then dried. The shell underwent a pyrolysis step for 3 hours at $600 \text{ }^\circ\text{C}$ in the N_2 atmosphere. Chemical activation was done by adding KOH to the biochar into three different KOH : Carbon ratios (3:1, 4:1, 5:1) to enhance the surface area. This 5:1 ratio yielded the highest surface area of $2450 \text{ m}^2 \text{ g}^{-1}$. The Polyoxometalates $[\text{PMo}_{12}\text{O}_{40}]^{3-}$ loaded into the activated carbon showed an areal capacitance of 1.16 F cm^{-2} , which is 2.5 times larger than the unloaded carbon.

In 2017, Palomino Pablo et al. synthesized a new nanomaterial for use in supercapacitors. The electrode material was made up of three different ratios of activated carbon derived from the resorcinol-formaldehyde hydrogel. First, the resorcinol-formaldehyde hydrogel was carbonized, and then it was chemically activated using KOH in various ratios. The activated carbon was then anchored with PMo_{12} . The prepared electrode material underwent electrochemical testing, exhibiting a specific capacitance of 293 F g^{-1} , which was 35% higher than the unmodified activated carbon's gravimetric capacitance.

Chen Shai et al. explored a new electrode material in 2018. The material is made up of $\text{NiPW}_{12}\text{NP}$ Polyoxometalates infused into a nitrogen-doped mesoporous carbon matrix derived from orange juice. The electrochemical performance was tested using an asymmetric electrode setup, where $\text{NiPW}_{12}\text{NP}$ acted as the cathode, and MnO_2 acted as the anode. The asymmetric electrode demonstrated a high specific capacitance of 547 F g^{-1} and an energy density of 10.88 Wh kg^{-1} . Additionally, it showed good cycle stability with 92.8% retention after 5000 charge-discharge.

In 2020, Zhu et al. developed a hybrid material by impregnating faradic Polyoxometalates (PW_{12}) into AC using DMF as an organic medium. The team tested the hybrid material electrochemically in 1M TEABF₄ in an acetonitrile electrolyte. The results showed that the hybrid material had a specific capacitance of 82 F g⁻¹ at a current density of 0.5 A g⁻¹. Furthermore, the hybrid material demonstrated excellent cycle stability, with 93% retention of the initial capacitance after 10,000 cycles and a reasonable rate capability.

In 2021, Maity et al. synthesized hybrid electrode materials by combining activated carbon with Keggin-type vanadomolybdates (VMo_{11} and V_2Mo_{10}). The resulting composite materials, AC- VMo_{11} and AC- V_2Mo_{10} , demonstrated impressive electrochemical performance, with specific capacitances of 430 F g⁻¹ and 214 F g⁻¹, respectively, at a current density of 0.2 A g⁻¹. These measurements were taken using a two-electrode system in an ionic liquid electrolyte.

In a recent study by Maity et al. (2021), a novel SC electrode material was introduced by doping NiV₁₄ onto porous activated carbon (AC). The resulting compound, AC-NiV₁₄, exhibited significantly enhanced electrochemical properties for both symmetric and asymmetric SC cells, with the ability to operate at a notably higher potential of 1.2 V (in 0.5M H₂SO₄). Notably, a capacitance of 316 F g⁻¹ was observed for 15 wt% (AC-NiV₁₄) at a current density of 1 A g⁻¹.

Anjana A V et al. (2022) explored the Keggin-type Polyoxometalates (MnV_{11} & MnV_{13}) doped with activated carbon electrode nanomaterials. The electrode material's properties were studied using both structural (FTIR, BET, FESEM) and electrochemical studies. The electrochemical performance shows that AC- MnV_{11} has a remarkable specific capacitance of 479.73 F g⁻¹ at 0.6 A g⁻¹, whereas AC- MnV_{13} exhibits 357.33 A g⁻¹.

In 2023, Ge Yuanyuan et al. explored a new nanohybrid electrode material. This material was based on soybean straw-derived activated carbon (SSAC) infused with Polyoxomolybdate (PMo_{12}). Both structural and electrochemical studies characterized the electrode material. Based on electrochemical studies, it was proven that PMo_{12} /SSAC exhibits both electric double-layer capacitance and pseudocapacitance

characteristics. The nanohybrid has a specific capacitance of 397.02 F g^{-1} at a scan rate of 5 mV s^{-1} . It also shows an energy density of 23 Wh kg^{-1} with a power density of $1016.05 \text{ W kg}^{-1}$. Cyclic stability was also assessed, showing a retention of 97.96% after 10000 cycles at 3 A g^{-1} .

In the same year, 2023, Sara Goberna Ferron et al. developed a novel three-component nanohybrid electrode material that integrates Polyoxometalates, silver nanoparticles, and activated carbon. The material was characterized using UV-Vis, PXRD, XPS, and electrochemical studies. Cyclic voltammetry revealed a specific capacitance of 81 F g^{-1} at 20 mV s^{-1} .

2.2 Scope of the Work

Recent scientific research has found that the performance of EDLC systems can be significantly enhanced by combining them with pseudocapacitive materials. Among the various nanocarbon substances used for designing POMs composite electrodes, Single-Walled Carbon Nanotubes, Multi-Walled Carbon Nanotubes, Activated Carbon, and Graphene have gained significant attention due to their ability to conduct electricity efficiently, large surface area, and ease of surface modification.

Researchers have found that immobilizing heteroPolyoxometalates on nanocarbon materials is an effective way to increase the capacitance of POM-modified electrodes. However, due to their high cost, POMs hybrids on CNTs and graphene are not commonly used in commercial EC applications. On the other hand, activated carbon remains the most widely used commercial EDLC material because it is inexpensive and has a high double-layer capacitance. Recently, biomass-derived activated carbon has emerged as a cost-effective alternative.

This thesis explores the use of heteroPolyoxometalates such as Keggin and Wells-Dawson, with a particular focus on Wells-Dawson hybrids fabricated on activated carbon and biomass-derived porous carbon. These materials offer high capacitance and cost-effectiveness and hold great promise as a substitute for expensive designer nanomaterials.

2.3 Objectives

Given the extant literature regarding the electrochemical behavior of Polyoxometalates (POMs) in activated carbon and biomass-derived activated carbon, the present study outlines a series of objectives to be achieved. The aim is to carry out an in-depth examination of the electrochemical characteristics of POMs in these two types of carbon materials. By doing so, this study seeks to provide valuable insights into the potential of POMs as an effective electrochemical material.

1. Design and synthesize phosphomolybdic acid embedded into orange peel-derived activated carbon-based electrode materials and investigate the electrochemical properties of the electrode materials.
2. The study aimed to delve into the properties of a hybrid supercapacitor electrode material that exhibits high performance. The material consisted of Wells-Dawson-type diphosphodecaoctatungstate (P_2W_{18}) impregnated with activated carbon. The study focused on understanding the material's structural and electrochemical properties in greater detail.
3. Wells-Dawson type vanadodiphosphotungstate ($P_2VW_{17}O_{62}$) encapsulated in a lignin-based activated carbon electrode material and characterized using analytical and electrochemical methods.
4. A complete study of electrode material consisting of vanadium-based phosphomolybdic of Keggin $H_4[PVMo_{11}O_{40}]$ and Wells-Dawson $H_7[P_2VMO_{17}O_{62}]$ type Polyoxometalates incorporated over pomegranate peel-derived activated carbon.

2.4 Organization of the Thesis

The thesis is comprised of seven chapters.

Chapter 1 briefly introduces the various prevailing energy storage technologies, focusing on supercapacitors. The mechanism of supercapacitors is discussed in depth, and an overview of electrode materials, including both EDLC and PC, is provided. Furthermore, the text covers the electrolyte media and application of supercapacitors.

Chapter 2 explains the literature review, covering various materials used for SC applications based on POM-infused activated carbon. The scope and objectives of this thesis are then outlined, detailing the materials and methods utilized in this study, as well as the experimental methodologies employed to construct and analyze the SC electrode.

Chapter 3, a study was conducted to synthesize activated carbon from orange peels, a waste biomass material. The process involved a single-step reaction of infusing the activated carbon with phosphomolybdic acid (PMA). A nanohybrid electrode material's physical and electrochemical attributes that incorporated PMA on the orange peel-derived activated carbon were evaluated and reported. This investigation is significant as it can help to develop nanohybrid electrode materials with superior electrochemical properties.

Chapter 4 demonstrates results on Wells-Dawson type polyoxotungstate (P_2W_{18}) synthesized and infused on activated carbon. The prepared nanocomposites were studied electrochemical properties in acidic aqueous electrolyte media in two electrode symmetric cell configuration.

Chapter 5 elucidates a simple and efficient method for synthesizing diphosphovanadodecaheptatungstate (P_2VW_{17}) embedded into activated carbon derived from Lignin (LDAC) with varying weight percentages. The resulting nanocomposites were thoroughly investigated through structural and electrochemical analyses and implemented in practical applications.

Chapter 6 an innovative electrode material is discovered. The vanadophosphomolybdic acid of Keggin ($PVMo_{11}$) and Wells-Dawson (P_2VMo_{17}) was synthesized using a simple and effective method. By infusing both Keggin and Wells-Dawson vanadophosphomolybdic acid in pomegranate peel-derived activated carbon (PDAC), the infusing nanocomposites were subjected to extensive structural and electrochemical analyses and applied in real-world applications.

Chapter 7 comprehensively summarises the key research findings of this thesis work. Additionally, this section provides valuable insights and recommendations for future

research in this area and beyond, paving the way for further exploration and advancements in the field.

2.5 Materials and Methodology

2.5.1 Materials

Biomass feedstocks such as orange and pomegranate peel were procured from the local market in Mangalore and Alkaline Lignin from TCI. Sigma Aldrich was the source of Phosphomolybdic acid, Sodium tungstate (Na_2WO_4), and Sodium Molybdate (Na_2MoO_4). Analytical grade reagents from Loba Chemicals such as Potassium Chloride (KCl), Ammonium Chloride (NH_4Cl), Sulfuric acid (H_2SO_4), Distilled water and HPLC-grade water were used in this study without further purification. Polyvinylidene fluoride (PVDF) was obtained from Alfa Aesar.

2.5.2 Synthesis

2.5.2.1 Pyrolysis of orange peels produces activated carbon (OPAC)

The activated carbon from orange peels was prepared following the reported synthesis process described elsewhere (Kaipannan and Marappan 2019). The schematic representation of activated carbon synthesis from orange peels is shown in **Figure 2.1**. After collecting orange peels, they were washed thoroughly with water to remove dirt, dried under sunlight, and ground into fine powder. The powdered orange peel was pre-carbonized for 4 h at 550 °C in a tubular furnace under a nitrogen atmosphere. The resultant carbon material was chemically activated using KOH. During the chemical activation process, a mixture of powdered carbon material (1 g) and pelleted KOH (3 g) taken in a ratio of 1:3 was heat treated at 800 °C for 1 h in a flowing of nitrogen in a tube furnace. The KOH-activated carbon material was ground into powder, treated with 1 M HCl, washed thoroughly with distilled water, and dried at 110 °C overnight in a hot air oven. The obtained activated carbon sample was named OPAC.

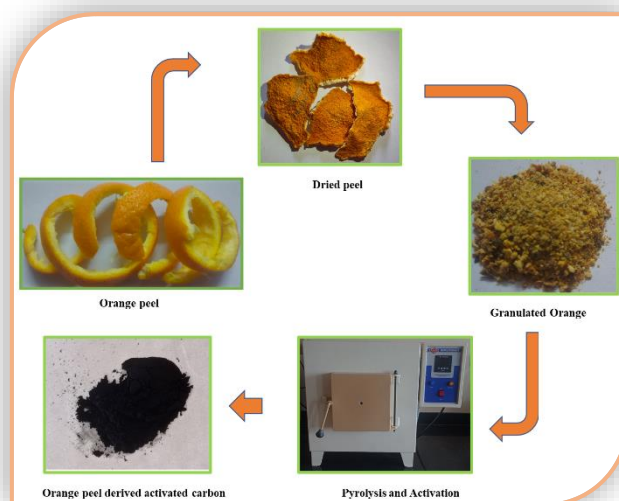


Figure 2.1: Schematic representation of orange peel-derived activated carbon (OPAC) preparation.

2.5.2.2 Preparation of phosphomolybdic acid–orange peel-derived activated carbon (OPAC-PMA) nanohybrids

The phosphomolybdic acid (40 wt%) was dissolved in 2 ml of distilled water taken in a glass vial. The required amount of OPAC (60 wt%) was taken in a round bottom flask. Then, the prepared aqueous phosphomolybdic acid (PMA) solution was slowly added to it (**Figure. 2.2**). The resulting solution was stirred for 24 h at room temperature. The obtained black residue was filtered and washed thoroughly with HPLC-grade water until a clear filtrate was obtained. The black OPAC-PMA was collected and dried before use.

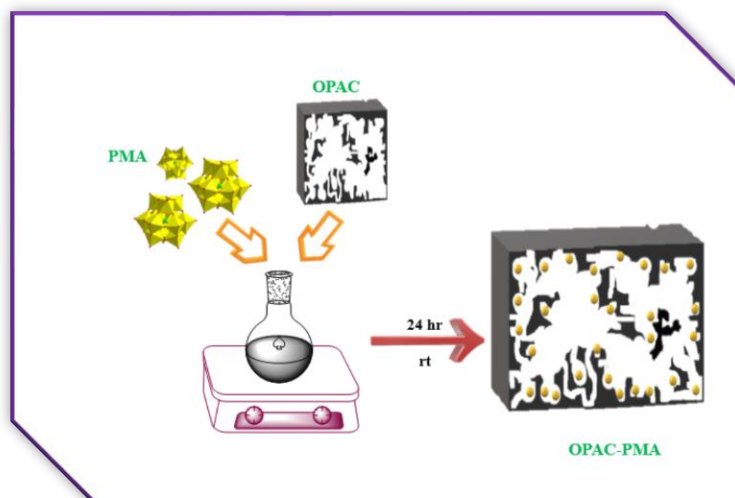


Figure 2.2: Schematic representation of the synthesis of infusing phosphomolybdic acid into orange peel-derived activated carbon.

2.5.2.3 Synthesis of AC- P_2W_{18} composite

The Wells-Dawson-type Polyoxometalates potassium octadecatungstate diphosphate $K_6[P_2W_{18}O_{62}] \cdot xH_2O$ was synthesized according to the literature (Graham and Finke 2008). In order to achieve different concentrations of P_2W_{18} on AC, the amount of P_2W_{18} was varied. The AC- P_2W_{18} was prepared using the procedure outlined below in varying amounts of P_2W_{18} of 5 wt%, 10 wt%, and 15 wt.%. 1 g of AC in 0.010 L of methanol was dispersed in a round bottom flask. The methanol solution was stirred for 10 minutes with a magnetic stirrer to ensure even distribution. In order to prepare the P_2W_{18} solution, a small amount of water (less than 5 ml) was dissolved and added gradually dropwise into the AC-methanol solution. The resulting solution was kept stirring for approximately 24 hours at room temperature. After drying under reduced pressure, the solution was washed with plenty of aqueous solution to remove the excess P_2W_{18} . The black residue was then collected and finally allowed to dry.

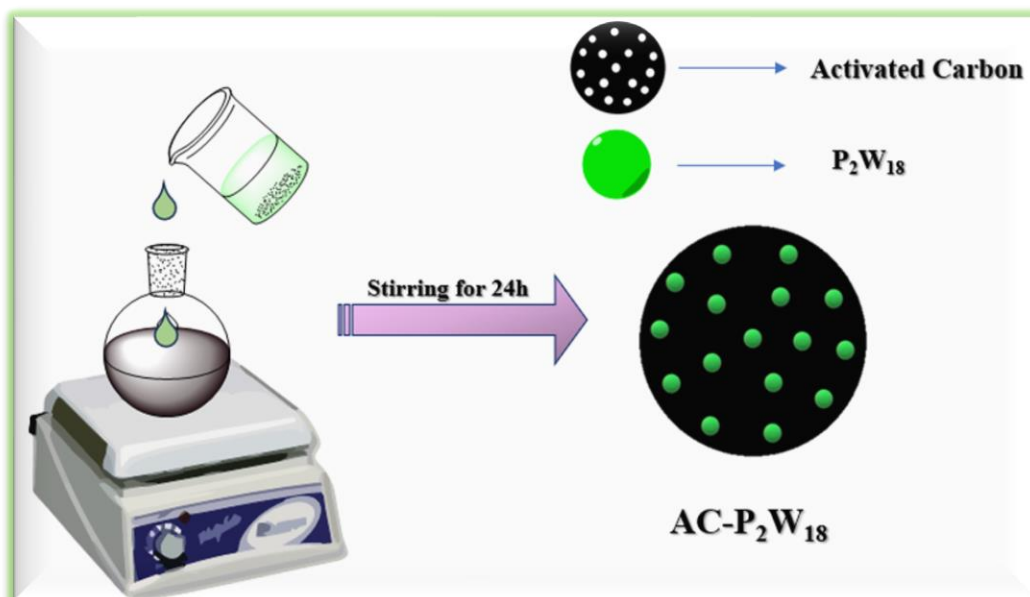


Figure 2.3: Schematic representation of the formation of AC-P₂W₁₈ composite.

2.5.2.4 Synthesis of Alkaline Lignin derived activated carbon (LDAC)

According to the procedure reported elsewhere (Babeł and Jurewicz 2008; Subramani et al. 2017), activated carbon was prepared from alkaline lignin. An atmospheric nitrogen atmosphere was used to pre-carbonize the powdered alkaline lignin for four hours at 550 °C. A chemical activation with KOH was performed on the resultant carbon material. A mixture of powdered carbon material (1 g) and pelleted KOH (3 g) was heat treated in a tube furnace at 800 °C for one hour, with nitrogen flowing through it during the chemical activation process. After grinding the KOH-activated carbon material into powder, treating it with 1M HCl, and washing it thoroughly with distilled water, it was dried in a hot air oven overnight at 110 °C. The sample of activated carbon obtained was referred to as LDAC.

2.5.2.5 Synthesis of septadecatungstovanadodiphosphate K₇P₂VW₁₇O₆₂.xH₂O (P₂VW₁₇)

The procedure involved in preparing a potassium salt of Lacunary Well-Dawson polyanion K₁₀P₂W₁₇O₆₁ was followed by the method described in the literature (Graham and Finke 2008). To prepare the solution, 10 ml of 0.5M NaVO₃ and 25 g of K₇P₂VW₁₇O₆₂.xH₂O (P₂VW₁₇) were added to the 140 ml of 0.5M HCl. Later, 22 g of

KCl was added to the above solution and stirred for 1 hour. After that, the precipitate was filtered off and recrystallized from 30 ml of 0.1M HCl (Abbasi et al. 1991).

2.5.2.6 Synthesis of the LDAC-P₂VW₁₇ composite

In order to obtain different concentrations of P₂VW₁₇ on LDAC (**Figure. 2.4**), the P₂VW₁₇ amount was varied. Following the method described below, LDAC-P₂VW₁₇ was prepared by varying the P₂VW₁₇ concentrations of 15, 20, and 30 wt%. In a round-bottom flask, LDAC was mixed with 10 ml of methanol and stirred for 10 minutes to achieve a consistent mixture. Subsequently, a solution of P₂VW₁₇ was made by dissolving P₂VW₁₇ in a small amount of water (no more than 5 ml) and then incrementally added to the methanol solution containing LDAC. This combination was stirred continuously for about 24 hours at room temperature, followed by drying under a vacuum. Later, the black residue was collected and kept for drying.

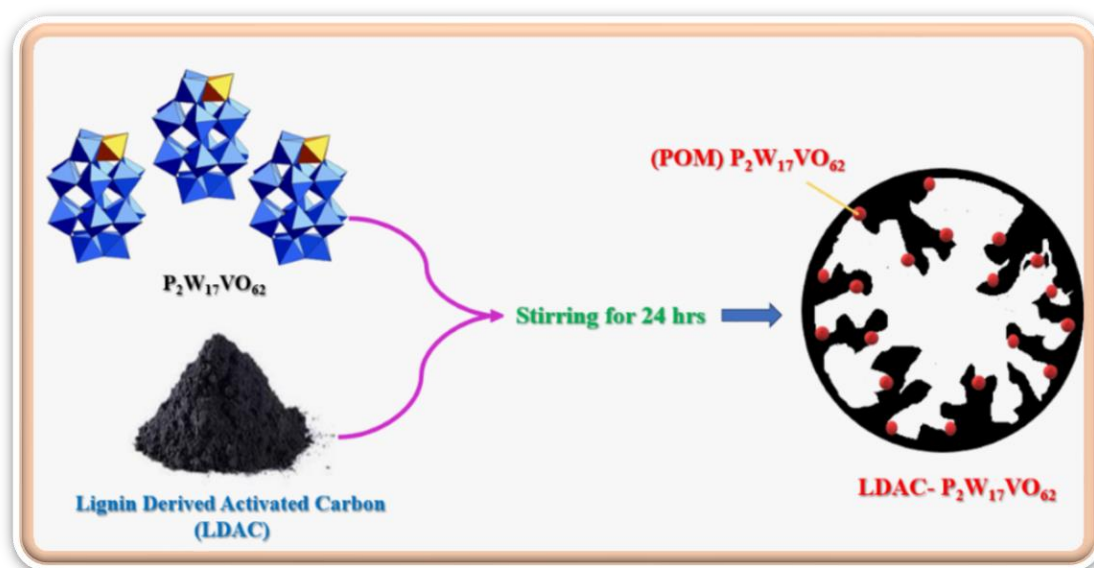


Figure 2.4: Schematic representation of impregnated septadecatungstovanadodiphosphate in lignin-derived activated carbon (LDAC-P₂VW₁₇).

2.5.2.7 Synthesis of pomegranate peel-derived activated carbon (PDAC)

The following procedure, which has been previously described (Choi et al. 2021), was used to prepare activated carbon from pomegranate peel. The peel of pomegranate

in powdered form was subjected to pre-carbonization at a temperature of 550°C for a duration of four hours, with the process being carried out in an atmosphere of nitrogen present in the surroundings. After completing this step, the resultant carbon material was chemically activated using KOH. A mixture of 1 g powdered carbon material and 3 g pelleted KOH was heated in a tube furnace at 800 °C for one hour while nitrogen flowed through the process. After grinding the KOH-activated carbon material into powder, it was treated with 1M HCl and washed thoroughly with distilled water. The activated carbon material was dried overnight in a hot oven at 110 °C. The resulting sample of activated carbon was named PDAC.

2.5.2.8 Synthesis of diphosphovanadoseptamolybdate $K_7P_2VMo_{17}O_{62}\cdot xH_2O$ (P_2VMo_{17})

The Wells-Dawson diphosphovanadododecaseptamolybdate was prepared using a literature review as a guide (Gao et al. 2018). In a 100ml three-necked round-bottom flask, $NaVO_3\cdot 2H_2O$ (1 mmol) and $Na_2HPO_4\cdot H_2O$ (2 mmol) were added to deionized water and stirred constantly. The pH of the mixture was maintained around 4 by adding sulphuric acid dropwise. $NaMoO_4\cdot 2H_2O$ (17 mmol) was then dissolved in a minimal amount of deionized water, and the resulting solution was added to the above mixture. The pH of the solution was again maintained around 4. The mixture was then refluxed at 120 °C for 8 hours. After 8 hours, the solution was allowed to cool to room temperature and extracted using diethyl ether.

2.5.2.9 Synthesis of P_2VMo_{17} -PDAC

To prepare the solution, a glass vial was used to dissolve 20% diphosphovanadododecaseptamolybdate in 2 ml of distilled water. Subsequently, a round bottom flask containing 80% PDAC dispersed in a 10-ml methanol solution was utilized. The aqueous solution was gradually combined with the PDAC mixture while continuously stirring for 24 hours at room temperature. This process resulted in the evaporation of the solution, which left a black residue that was collected and stored for future use.

2.5.2.10 Synthesis of $PVMo_{11}$ -PDAC

The procedure involved in preparing a phosphomolybdate of H_4PVMo_{11} was followed by the method described in the literature (Akba et al. 1997). In a glass vial, 2 ml of distilled water was used to dissolve 40 wt% vanadophosphomolybdic acid. The PDAC (60 wt%) was mixed with a methanol solution in a round bottom flask measuring 10 ml. Afterward, the aqueous $PVMo_{11}$ solution was added gradually to the PDAC mixture. The solution was stirred at room temperature for 24 hours. The solution evaporated, leaving a black residue collected and stored at room temperature.

2.5.2.11 Synthesis of combined $P_2VMo_{17}/PVMo_{11}$ in PDAC

In order to prepare the required amount of PDAC (80 wt %), it was dispersed in a round bottom flask containing 10 ml of methanol solution. In addition, a Polyoxometalates solution was formulated by taking both Keggin and Wells-Dawson POMs, specifically $PVMo_{11}/P_2VMo_{17}$, in a ratio of 1:1 in 20 wt%, and subsequently dissolved in distilled H_2O . The aqueous POM solution ($P_2VMo_{17}/PVMo_{11}$) was then carefully added to the PDAC methanol solution. The obtained solution was stirred vigorously for 24 hours at room temperature, and then evaporation was used to remove it. The black residue obtained was collected and kept at room temperature.



Figure 2.5: Schematic representation of infused Wells-Dawson and Keggin Polyoxometalates in pomegranate-derived activated carbon.

2.5.3 Electrode Preparation

To prepare efficient electrode materials, active materials, mesoporous carbon, and binders like PVDF are mixed in specific ratios. Two ratios were used: 8:1:1 and 9:1. In the 9:1 ratio, only active material and PVDF were used, while in the 8:1:1 ratio, active material, PVDF, and mesoporous carbon were used, respectively. The mixture is then blended thoroughly using a mortar and pestle. A few drops of N-methyl 2-pyrrolidone (NMP) solvent are added dropwise to the mixture to achieve a homogeneous slurry. The homogeneous slurry is then coated onto a carbon cloth (with a surface area of 1 x 1 cm²) using the pasting method. The coated fabric is set to dry for 12 hours in an oven maintained at 60 °C. A two-electrode symmetric cell configuration is employed to construct the electrodes. Stainless steel is utilized as the material for the current collector. The working electrodes are positioned on either side of the collector, with the side coated in slurry facing the separator and the uncoated side directed towards the current collector. The separator is soaked with electrolytes before being placed. Electrochemical performance is then carried out to assess the efficiency of the electrodes.



Figure 2.6: Schematic representation of two electrode configuration setups.

2.6 Characterization Techniques

2.6.1 Physical Characterization

2.6.1.1 Fourier transforms infrared spectroscopy (FTIR)

The Fourier transforms infrared spectroscopy analysis using Bruker 4000 USA was employed to gain insights into the functional groups present in the synthesized

composite material. This study focused on analyzing vibrational bands at certain wavenumbers to find details about the composite's chemical structure. The FTIR spectra were obtained through two distinct approaches: the ATR technique, spanning 600 cm^{-1} to 4000 cm^{-1} , and the KBr pellet technique, which encompasses a wavenumber range of 400 cm^{-1} to 4000 cm^{-1} . These two methods were used to capture all the necessary information about the functional groups in the composite (Smith 2011).

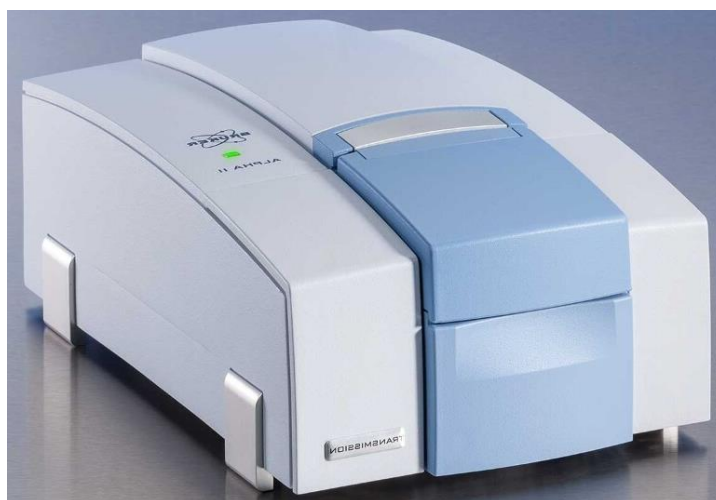


Figure 2.7: FTIR setup (Image courtesy: Chemistry department, NITK, Surathkal).

2.6.1.2 Thermal Gravimetric Analysis (TGA)

Thermal Gravimetric Analysis (PerkinElmer TGA 4000 to warm at $5\text{ }^{\circ}\text{C}/\text{min}$ and to infuse N_2 at 77K at $20\text{ ml}/\text{min}$) is a widely used technique to measure the change in mass of a sample over time or at different temperatures due to its composition. It involves controlling temperature, including ambient temperature to $1000\text{ }^{\circ}\text{C}$ and atmospheric conditions like nitrogen, argon, or helium. TGA provides insights into sample composition, thermal stability, and degree of cure or breakdown, including processes like volatile component evaporation, oxidative or thermal breakdown, heterogeneous chemical response, and phase shifts (Coats and Redfern 1963).



Figure 2.8: TGA setup (Image courtesy: Chemistry department, NITK, Surathkal).

2.6.1.3 Field emission scanning electron microscope (FESEM) and Energy dispersive X-ray analysis (EDS)

Field emission scanning electron microscope (Carl Zeiss Sigma, Germany) is a technique used to analyze the morphology and microstructure of compounds, providing structural information like nanomaterial topology, agglomeration, crystallinity, atomic arrangements, and particle size distribution. It also confirms elemental composition in nanocomposites through EDS analysis and weight percentage mapping.



Figure 2. 9: FESEM and EDS setup (Image courtesy: Central research facility (CRF), NITK, Surathkal).

2.6.1.4 X-ray photoelectron spectroscopy (XPS)

X-ray photoelectron spectroscopy (XPS) is a surface-sensitive quantitative spectroscopic method that relies on the photoelectric effect, commonly used to identify the elements within a composite or material (utilizing ThermoFisher Scientific equipment: Model Nexsa base). It can be discerning elements from the material's surface, providing insights into their chemical states, overall electronic structure, and more. Furthermore, this spectroscopic technique identifies the elements present in the material and those chemically bonded to it (Andrade 1985).



Figure 2.10: XPS setup (Image courtesy: Advanced Material Research Center. IIT Mandi).

2.6.1.5 Powder X-ray diffraction (PXRD)

The powder X-ray diffraction patterns were recorded using the (Malvern PANalytical, Netherlands; Model: Empyrean 3rd Gen) diffractometer. This technique was employed to confirm the synthesized nanocomposites' structural integrity qualitatively. The diffraction peaks were compared with their Miller indices, which were recorded in the JCPDS database for analysis. Additionally, the PXRD method

provided crucial insights into the nature of the synthesized complex's structure. It helped determine whether the synthesized material was crystalline or amorphous, thus giving valuable information about its structural properties (Epp 2016).



Figure 2.11: PXRD setup (Image courtesy: Central research facility (CRF), NITK, Surathkal).

2.6.1.6 Brunauer-Emmett-Teller (BET) Analysis

Brunauer-Emmett-Teller analysis measures the nanocomposite surface area and pore size distribution through nitrogen adsorption-desorption isotherm.



Figure 2.12: BET setup (Image courtesy: Central research facility (CRF), NITK, Surathkal).

2.6.2 Electrochemical Studies

The electrochemical performance of a supercapacitor cell was evaluated through multiple tests, including cyclic voltammetry (CV), galvanostatic charge and discharge studies (GCD), and electro impedance spectroscopy (EIS) (IVIUM Technologies BV co. Netherlands, Model: Vertex). The supercapacitor's electrochemical behavior was studied using a two-electrode cell configuration in an aqueous electrolyte. The analysis aimed to understand the cell's energy storage and transfer capabilities, and the results were evaluated to determine the cell's performance.

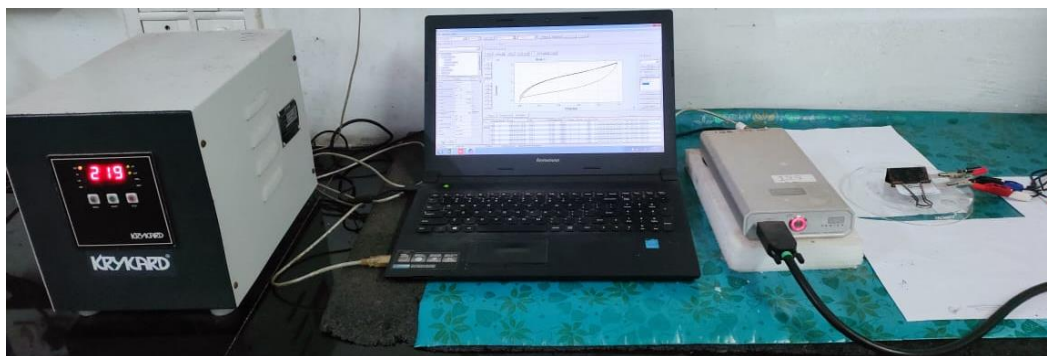


Figure 2.13: Electrochemical workstation setup (Image courtesy: (Chemistry department, NITK, Surathkal).

2.6.2.1 Cyclic Voltammetry (CV)

Cyclic Voltammetry is a highly significant electrochemical method that provides a detailed analysis of the redox behavior of various materials, including their oxidation and reduction processes, chemical kinetics, rate capability, and reversibility. The potential of a supercapacitor cell is influenced by the choice of electrode and electrolyte used in the system (Marken et al. 2010). The system's specific capacitance and energy density were determined by altering the scan rate from 10 to 100 mV s⁻¹ and capturing the relevant data. The specific capacitance of the supercapacitor cell was calculated using **Equation (2.1)**, which is an essential step in characterizing the performance and efficiency of the system.

$$\text{Specific capacitance } (C_s) = \frac{1}{2m \times v \times \Delta V} \int I(V) dV \quad (2.1)$$

where m , v , and ΔV are the mass of the active material, scan rate, and potential window, respectively.

2.6.2.2 Galvanostatic charge and discharge studies (GCD)

The galvanostatic charge and discharge studies provide valuable insights into the behavior of electrode materials in supercapacitors. These studies are conducted using the chronopotentiometry method, which allows for the analysis of the charging and discharging timing of the electrode material within a specific potential window by varying current density. GCD is a robust method for studying a supercapacitor cell's specific capacitance, energy density, and power density, enabling researchers to fully understand the performance of the materials in use (Chandran et al. 2020). The specific capacitance, energy density, and power density of the electrode material are calculated using **Equations (2.2)**, **(2.3)**, and **(2.4)**, which are essential in determining the potential of the supercapacitor in various applications. The galvanostatic charge and discharge studies were analyzed using the chronopotentiometry method. The GCD studies help study the electrode material's charging and discharge timing by varying current density at a definite potential window. GCD is the robust method for studying the supercapacitor cell's specific capacitance, energy, and power density.

$$\left. \begin{aligned} \text{Specific capacitance } C_s &= i * \Delta \frac{t}{m} * (\Delta V) V \\ \text{Specific Capacitance } C_s &= I * \Delta t / \Delta V \text{ F g}^{-1} \end{aligned} \right\} \quad (2.2)$$

where I is the current density (A g⁻¹), Δ t is the discharge time, and Δ V is the potential window (V).

$$\text{Energy (E)} \quad E = \frac{1}{2} \times C \times \Delta V^2 \times \frac{1000}{3600} \text{ Wh kg}^{-1}$$

$$\text{Energy density (E.D)} \quad E = i \int V dt \text{ Wh kg}^{-1} \quad (2.3)$$

$$\text{Power Density (P.D)} \quad P = \frac{E}{\Delta t(s)} \times 3600 \text{ W kg}^{-1} \quad (2.4)$$

$$\text{Coulombic Efficiency } (\eta) = \frac{\text{Discharge time}}{\text{Charging time}} \times 100 \quad (2.5)$$

where E is the energy density (Wh kg⁻¹), Δ t is the discharge time in seconds, Δ V is the potential window (V), and P is the power density (W kg⁻¹).

2.6.2.3 Electro Impedance Spectroscopy (EIS)

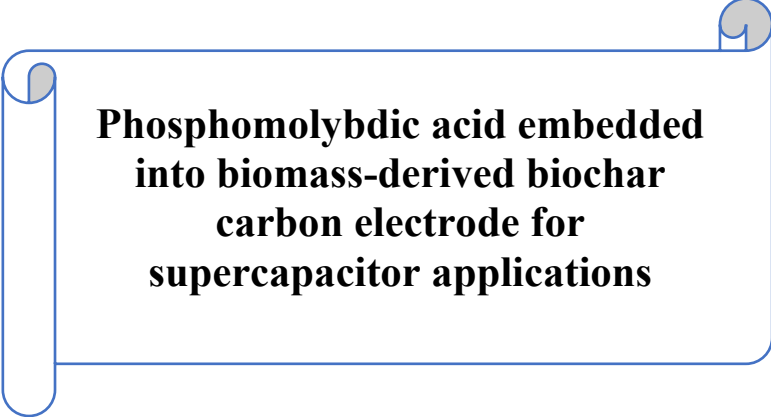
Electroimpedence Spectroscopy analysis was carried out to study the electrode material response to electrical signals over a frequency region of 0.01Hz to 100KHz at a potential of 10mV. The Nyquist plots, bode phase and angle plots, bode impedance plots, and capacitance variation with frequency plots were used to observe the impedance spectra. (Muzaffar et al. 2019). Nyquist plots were used to determine the internal resistance of electrode materials, capacitive nature, knee frequency, and rate capability. The impedance is a complex quantity consisting of a real part (Re(Z)) and an imaginary part (Im(Z)), each contributing uniquely to the system's electrical behavior. The capacitance of the real ($C'(\omega)$) and imaginary ($C''(\omega)$) portion was calculated using the following equation.

$$C'(\omega) = \frac{-Z''(\omega)}{\omega |Z(\omega)|^2}$$

$$C''(\omega) = \frac{Z'(\omega)}{\omega |Z(\omega)|^2}$$

Here, Z' and Z'' are the impedance of the real and imaginary portion, ω is the frequency in radians and C' and C'' are the capacitance of real and imaginary portions.

CHAPTER 3



**Phosphomolybdic acid embedded
into biomass-derived biochar
carbon electrode for
supercapacitor applications**

This chapter describes the synthesis of biomass waste orange peel-derived activated carbon (OPAC) and phosphomolybdic acid (PMA) infusing with OPAC through a one-pot reaction. The potential for using renewable biomass-derived activated carbon as an electrode material has been explored recently. Even though it is environmentally friendly and possesses intrinsic mechanical strength, it restricts its specific capacitance. Due to its fast multi-electron redox properties, it could be possible to enhance the energy density by combining capacitive materials like biomass carbon with redox-active inorganic metal oxides like Polyoxometalates. The present study reports and studies the electrochemical and physical properties of a nanohybrid electrode material embedded with phosphomolybdic acid (PMA) on orange peel-derived activated carbon (OPAC).

3. Result and Discussion

3.1 Structural, chemical, and morphological characterizations

3.1.1 FTIR

Fourier transforms infrared (FTIR, a Bruker 4000 (USA) spectrometer) spectroscopy was used to investigate the successful deposition of PMA on activated carbon; **Figure. 3.1** illustrates the FTIR spectra of bare orange peel-derived activated carbon (OPAC), pure PMA ($\text{H}_3[\text{PMO}_{12}\text{O}_{40}]$), and composite materials such as OPAC-PMA. In both PMA and OPAC, the FTIR bands correlate well with the literature. The FTIR bands of the PMA compound that appeared at 1062, 966, 867, and 797 cm^{-1} originated because of the vibration of the P-O, terminal Mo=O, corner Mo-O-Mo, and edge Mo-O-Mo bonds (Subramani et al. 2017). Similarly, IR bands at 3400 cm^{-1} , 1587 cm^{-1} , and 1407 cm^{-1} denote the presence of the O-H group, C=C group, and C=O, respectively. The IR band at 1105 cm^{-1} indicates the presence of the C-O-C (Murugan et al. 2003).

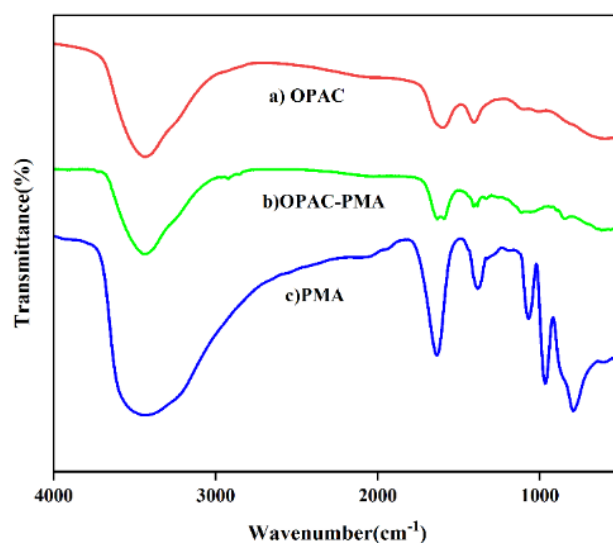


Figure 3.1: FTIR Spectra of OPAC, OPAC-PMA, and PMA.

3.1.2 TGA

The composite's thermogravimetric analysis (PerkinElmer TGA 4000) shows (**Figure. 3.2a**) that doping redox-active Polyoxometalates enhances the electrode's thermal stability. The thermal stability of the OPAC and OPAC-PMA was determined in the temperature ranging from room temperature to 900 °C at a scan rate of 10 °C. The DTG curve of OPAC-PMA depicts a water loss of 24% weight until 76.6 °C (**Figure. 3.2b**). The second stage weight loss of ~ 3% weight was observed at 551.5 °C, as shown in the DTG curve, which was attributed to the removal of structural water generated from acidic proton and oxygen present in the Keggin unit (Tirzhá L P Dantas et al. 2012). The OPAC released moisture at 71.36 °C, resulting in a weight loss of 21.05%. (**Figure. 3.2c**) shows further weight losses of 3% at 288.41 °C, which resembles the organic carbon structures, and a final loss of 2.6% at 714.77 °C due to either oxides or inorganic impurities, which corroborating the reported study (Tatibouët et al. 1997, Salgado et al. 2018).

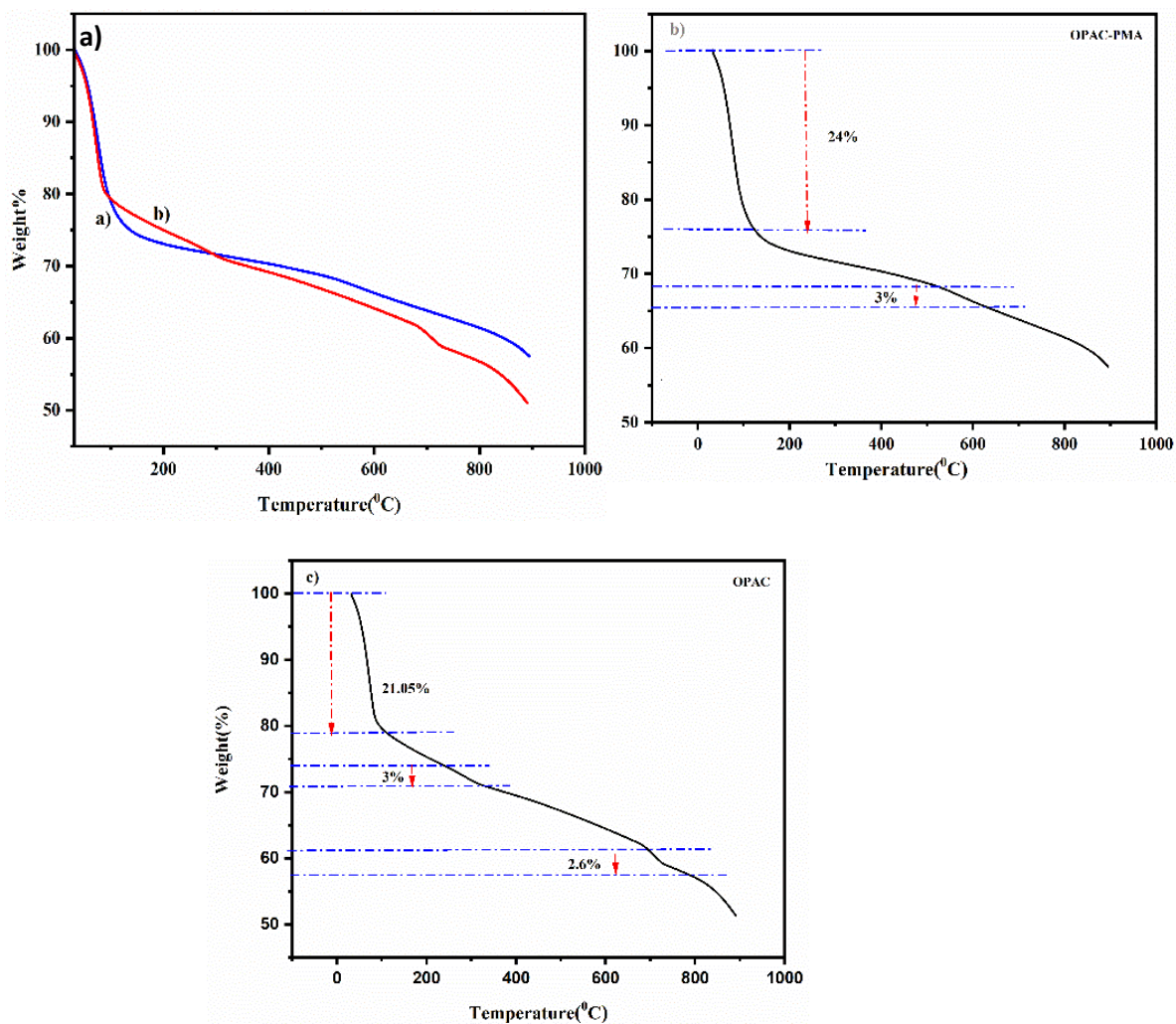


Figure 3.2: The TGA graph of a) OPAC-PMA and OPAC, DTA Curves of b) OPAC-PMA and c) OPAC.

3.1.3 PXRD

The PXRD (Rigaku Smart lab, Japan) patterns of OPAC and OPAC-PMA composite are presented in **Figure 3.3**. The OPAC demonstrates a broad, amorphous nature peak, as shown in **Figure 3.3**. The broad peaks showed around 24° (002) and 43.8° (100) are attributed to the graphitic carbon (Bazan et al. 2016). Due to the incorporation of PMA into the OPAC, the OPAC-PMA composite exhibits both amorphous and crystalline properties. The PMA features were confirmed by the JCPDS (00-043-0316).

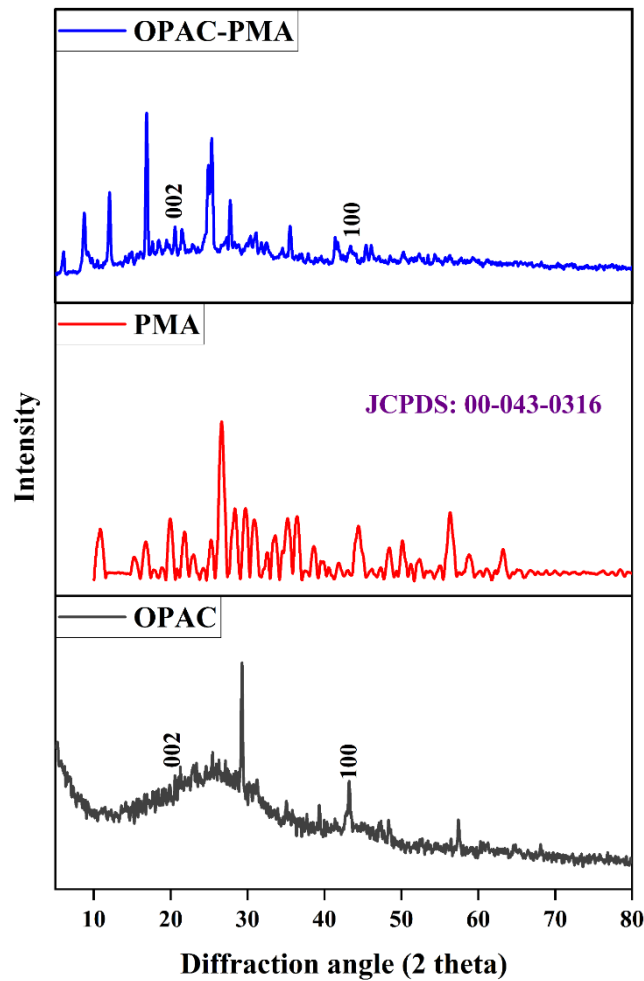


Figure 3.3: Powder XRD spectrum of OPAC-PMA, PMA and OPAC.

3.1.4 XPS

The electronic state of constituent elements on the surface was determined using XPS (X-ray photoelectron spectroscopy, Thermofisher scientific: Nexsa G2base). The individual XPS spectra of constituent elements of OPAC-PMA nanocomposites are presented in **Figure 3.4**. The C1s spectra of the OPAC-PMA nanocomposite revealed several peaks corresponding to element carbons of different characteristics, such as C=C at 284.5 eV, C-O-C at 285.4 eV, and C=O at 289.4 eV (**Figure 3.4a**) (Awitdrus et al. 2021). The O1s spectra revealed peaks for O atoms of the different environments at 532.1 eV for C-O (O₁), 533.6 eV for C=O (O₂), and 536 eV for H-O (O₃), and 529-530 eV for metal oxide (O₄) as shown in **Figure 3.4b**, (Awitdrus et al. 2021). Conversely, the OPAC-PMA nanocomposite exhibited two distinct peaks corresponding to 3d_{3/2} and 3d_{5/2} of Mo (+6) at 232.8 eV and 236.0 eV, respectively, as shown in **Figure 3.4c** (Wang

et al. 2015). The deconvoluted P spectra showed (**Figure. 3.4d**) a 2p peak at 135.2 eV assigned to the P atom (+5) in the Keggin anion (Wang et al. 2015).

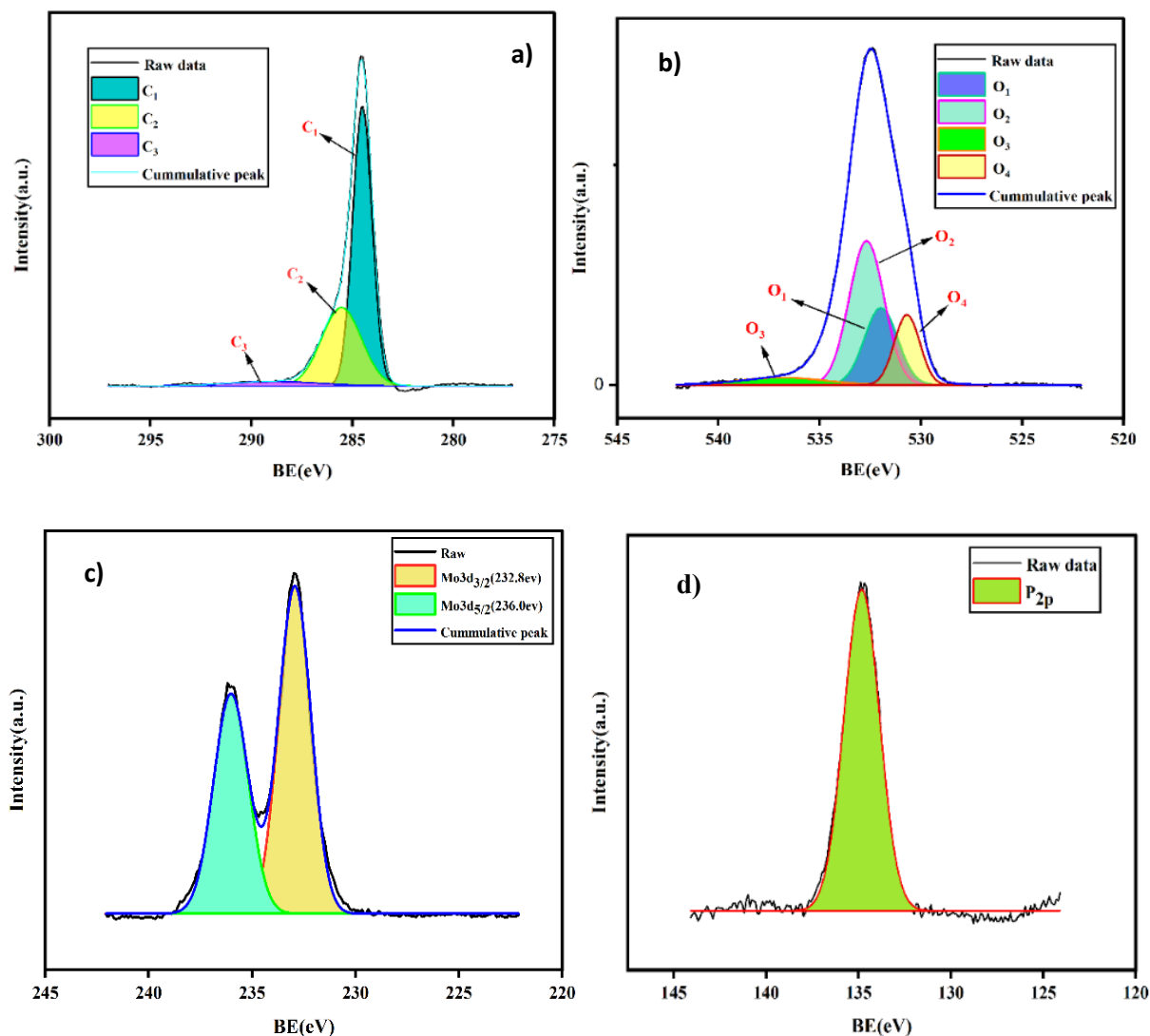


Figure 3.4: XPS Analysis a) C1s b) O1s c) Mo 3d d) P2p.

3.1.5 FESEM

The FESEM (Carl Zeiss Sigma FESEM, Germany) images of OPAC and OPAC-PMA composite electrode materials are presented in **Figure. 3.5**. FESEM imaging enables us to contrast the surface morphology between the two electrode materials. **Figure. 3.5(a)** shows the porous nature of OPAC, which is reminiscent of a honeycomb structure with a 7.5 μm size. Similarly, (**Figure. 3.5b**) represents the surface morphology of the composite (OPAC-PMA), which shows the deposition of

PMA with a size of approximately 2 nm and fits into the OPAC pores. FESEMs of OPAC have been previously reported in the literature (Kaipannan and Marappan 2019). The elemental composition of the OPAC-PMA composite was also performed using energy-dispersive spectroscopy (EDS), as shown in **Figure 3.5d**. The presence of C and O was confirmed by the EDS of the OPAC (**Figure 3.5c**). The composite's EDS confirms the occurrence of P, Mo, O, and C.

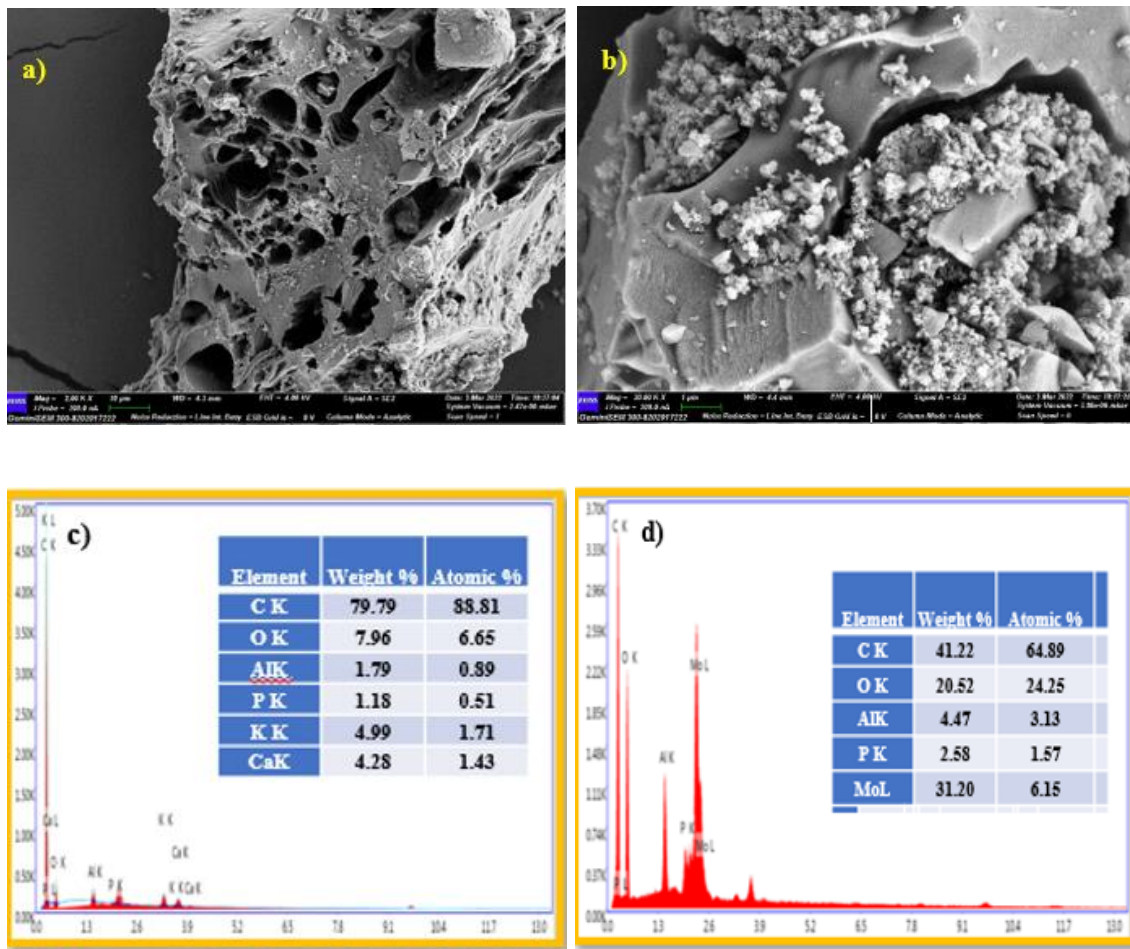


Figure 3.5: a) FESEM image of OPAC, b) OPAC-PMA & c) EDS of OPAC, d) OPAC-PMA.

3.1.6 BET

The BET surface area was estimated using a Micromeritics physisorption analyzer (Model ASAP 2020, USA). The N₂ adsorption-desorption study with the OPAC-PMA

composite material exhibited type I isotherm with pore-filling phenomena at a lower relative pressure ($P/P_0 < 0.1$), indicating the presence of micropores (**Figure. 3.6a**). The adsorption-desorption isotherm did not reveal well-defined hysteresis loop and capillary condensation characteristics of mesoporous pores. The micropore and BET surface area are estimated at $292 \text{ m}^2 \text{ g}^{-1}$ and $596 \text{ m}^2 \text{ g}^{-1}$, respectively. The average pore diameter estimated by the BJH method is $\sim 3.0 \text{ nm}$.

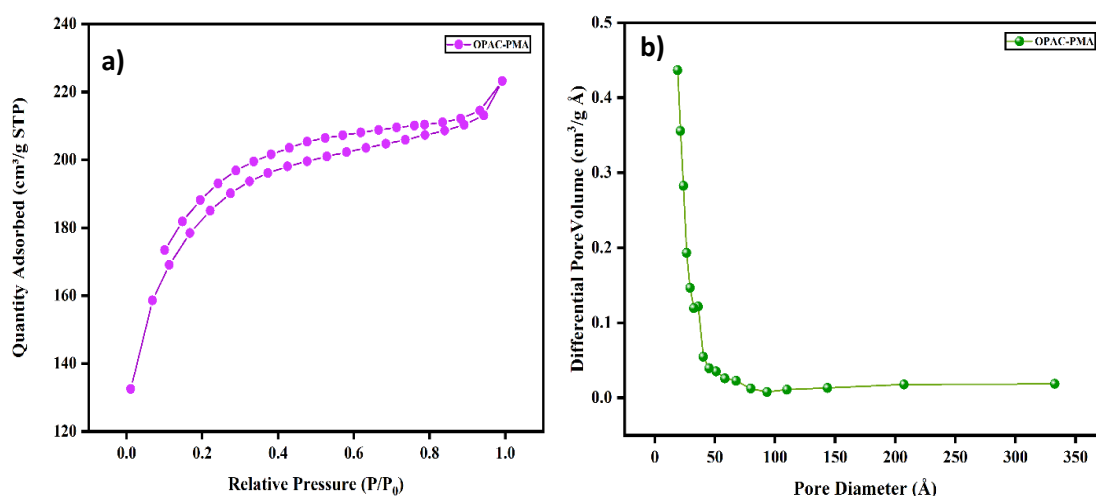


Figure 3.6: N₂ Adsorption and desorption Isotherm & b) Pore diameter of OPAC-PMA.

3.2 Electrochemical Characterization

3.2.1 CV

Cyclic voltammetry tests (IVIUM Technologies BV Co., The Netherlands, Model: Vertex) were conducted on both the OPAC and OPAC-PMA materials in a $0.5 \text{ M H}_2\text{SO}_4$ electrolyte solution. As shown in **Figure. 3.7a**, the CV curves collected at different scan rates (mV s^{-1}), such as 100, 70, 50, and 20, illustrate the rectangular shape of the OPAC material, indicating its EDLC behavior (Elgrishi et al. 2018). For the OPAC-PMA composite, the same scanning rates were applied, and the results are presented in **Figure. 3.7b**. The CV graph of OPAC-PMA observed irregular shape explains that the redox behaviour originates due to pseudocapacitive material on OPAC (**Figure. 3.7b**). Increasing the scan rate makes it even more difficult for the electrolyte ions to diffuse into the electrode's internal structure and pores as the movements of ions increase. A weak electrolyte and electrode materials interaction decreases specific capacitance

(Markoulidis et al. 2019). **Figure 3.7d** illustrates the combined CV curves of OPAC, PMA, and OPAC-PMA at 100 scan rates (mV s^{-1}). Here, we observed that bare OPAC exhibits the rectangular curve, suggesting EDLC behaviour. PMA is a pseudo-type material, showing oxidation/reduction peaks in the CV curves (**Figure 3.7c**). However, the OPAC-PMA display of a non-rectangular shape proves that the material undergoes the redox process. The redox peak current value is higher than the double-layer current. The OPAC-PMA composite shows a more significant increase in current density than the pure OPAC. The specific capacitance values were calculated by using **Equation (1.1)**. The bare PMA CV was performed at the same scan rates, and redox peaks are distinctively visible, as illustrated in **Figure 3.7c**.

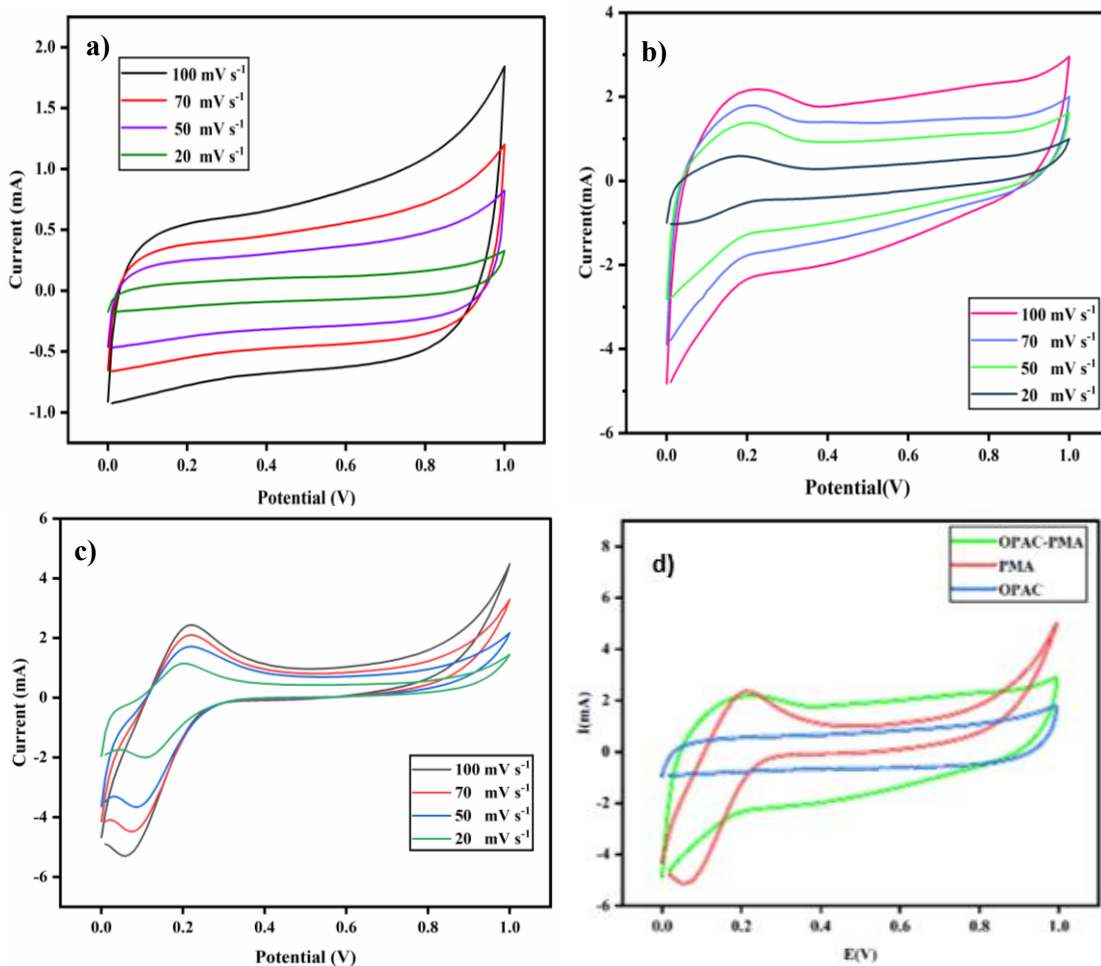


Figure 3.7: Cyclic voltammetry graphs a) OPAC b) OPAC-PMA c) PMA d) Combination graph of OPAC, OPAC-PMA, and PMA.

3.2.2 GCD

The galvanostatic charge-discharge characteristics under various current densities were studied to determine the electrode material's electrochemical behavior under a particular potential window. A galvanostatic charge-discharge (GCD) study was conducted using a 0.5M H₂SO₄ electrolyte solution in a two-electrode supercapacitor cell configuration. The composite showed a specific capacitance of 173.12 F g⁻¹ at a current density of 0.4 A g⁻¹ calculated using **Equation. (2.2)** with an energy and power density of 24.04 Wh kg⁻¹ & 800 W kg⁻¹ were calculated using **Equations (2.3)** and **(2.4)**. The OPAC-PMA exhibited a specific capacitance of 173.12 F g⁻¹, which is 66% higher than the bare OPAC's specific capacitance of 47.68 F g⁻¹ at the same current density. Ragone plots of OPAC and OPAC-PMA are represented in **Figure. 3.8e**. The Ragone plots demonstrate that composite OPAC-PMA has a higher energy density than OPAC. The GCD curve of OPAC exhibits the exact triangle shape, indicating high reversibility of the electrode material during the charge and discharge process, as described in **Figure. 3.8a** (Bohinc et al. 2001). However, the shape of the GCD curve of OPAC-PMA is not an ideal triangle, suggesting the oxidation/reduction process occurring in the presence of PMA, as shown in **Figure. 3.8b**. A perfectly nonlinear GCD graph of pseudocapacitive PMA because of the faradic process is shown in **Figure. 3.8f**, which has been performed in the same current density and electrolyte solution. The specific capacitance of OPAC and OPAC-PMA was compared at 1 A g⁻¹, as shown in **Figure. 3.8d**, indicating a drastic increase in specific capacitance resulting from the insertion of pseudocapacitive materials into non-faradic materials, which undergoes both redox reactions as well as charge accumulation mechanisms. The OPAC-PMA composite exhibits higher specific capacitance than the pure OPAC.

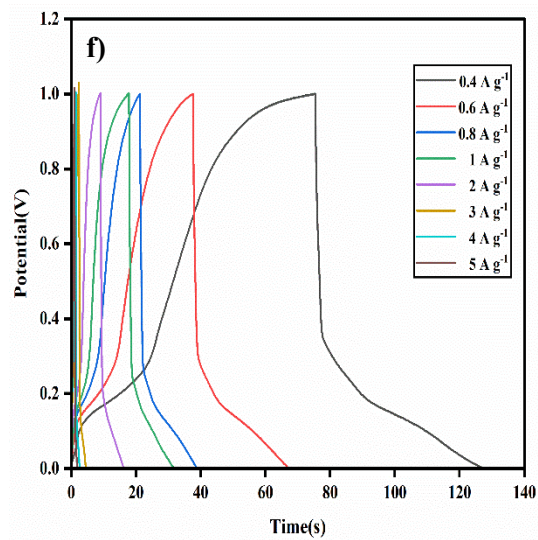
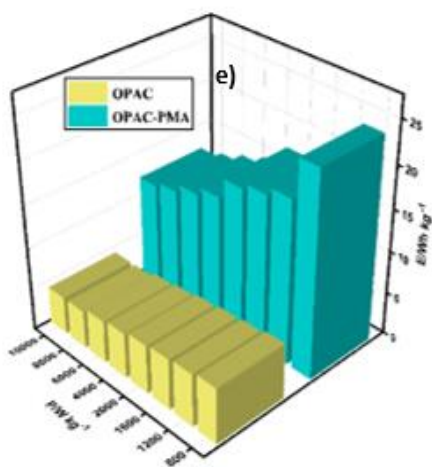
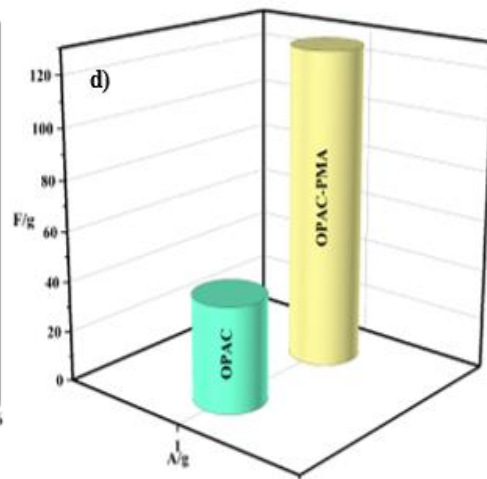
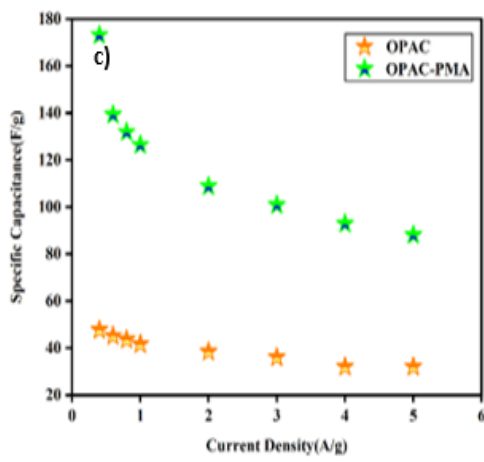
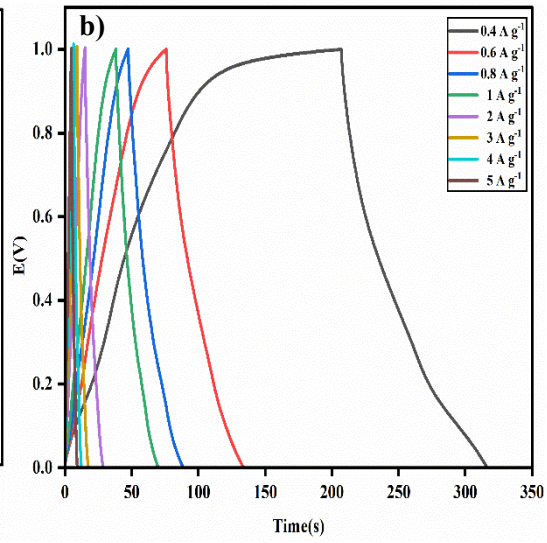
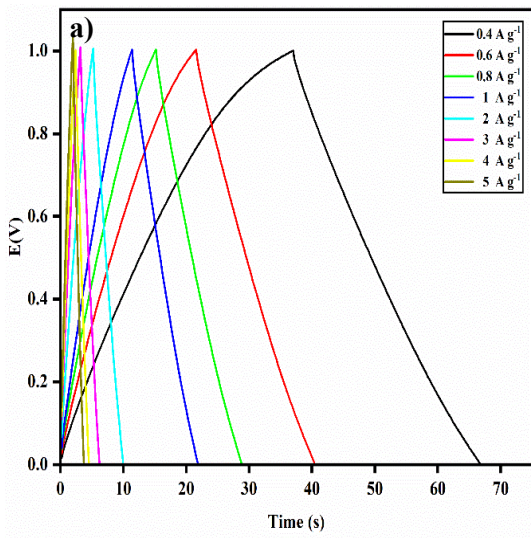


Figure 3.8: GCD graph of a) OPAC b) OPAC-PMA c) Current densities vs Specific capacitance for all systems d) current density vs specific capacitance for OPAC & OPAC-PMA at 1 A g^{-1} e) Ragone plot for OPAC & OPAC-PMA and f) GCD graph of PMA.

3.2.3 EIS

The composite (OPAC-PMA) electrodes performed an electrochemical impedance spectroscopy study. A Nyquist plot can be used to determine a composite's internal resistance and its charge transfer kinetics and ion diffusion processes (**Figure. 3.9a**) (Muduli et al. 2020). Over the high-frequency region, the impedance spectroscopy results demonstrate the semicircle arc for the electrodes. Because of limited mass transport, redox reactions mediated electron transfer kinetics are visualized by measuring the impedance of the electrode-electrolyte interface at lower frequencies. (Mousavi et al. 2017, Zhu et al. 2016). The appearance of the partial semicircle at higher frequencies indicates the resistance to charge transfer. Here, R_s represents the solution resistance, and the calculated R_s values for OPAC-PMA are $0.8989(\Omega)$. In contrast, the calculated polarized resistance (R_p) of OPAC-PMA is $5.025(\Omega)$, respectively. The charge transfer resistance (R_{ct}) values of OPAC-PMA are $4.126(\Omega)$, respectively. A schematic of the equivalent circuit for OPAC-PMA (symmetric) electrode material is presented in **Figure. 3.9b**. The equivalent series circuit was fitted using the software Zswipwim (3.21), where R_s represents the solution resistance, C_1 & C_2 correspond to the capacitance, R_1 & R_2 are the resistances, and W represents the Warburg coefficient, which is determined by the mass transportation that occurs.

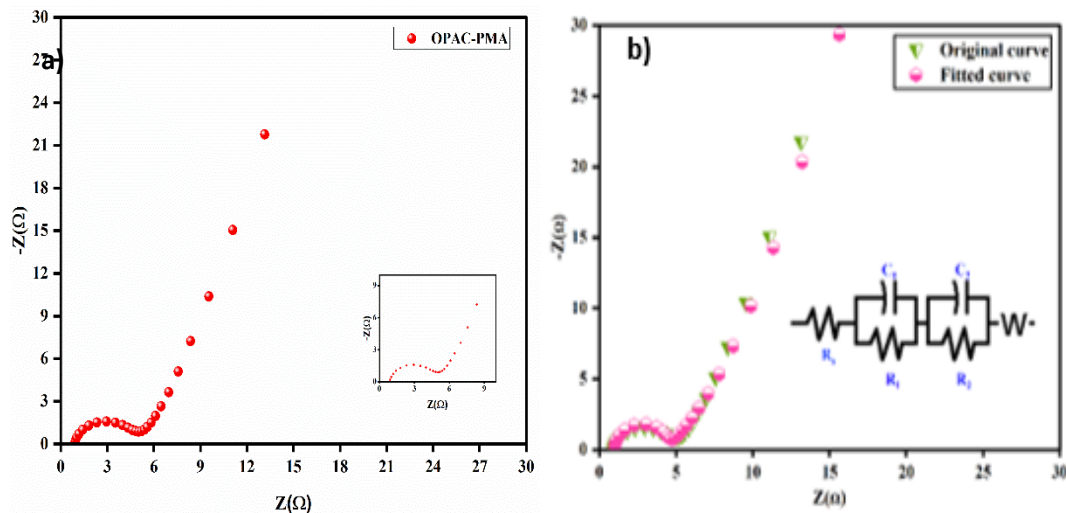


Figure 3.9: a) Nyquist plot b) Fitting the Nyquist plots requires using an equivalent circuit.

3.2.4 Cycle Stability

The supercapacitor cell's stability is the most imperative characteristic of a device's application. Symmetrical electrodes, such as OPAC and OPAC-PMA, have been tested for cycle stability using GCD (**Figure. 3.10**). In an electrochemical system, OPAC-PMA electrode material exhibited outstanding cycle stability of 88.23% after 4000 cycles at 6 A g^{-1} (**Figure. 3.10b**) for a symmetrical system, demonstrating that the long-term electrochemical capacitors are unaffected by subsequent cycles and similar to the first cycle. The insert pictured in **Figure. 3.10(a&b)** shows the nanocomposite's first and last four cycles. It has been observed that after 4000 cycles, the electrode materials are stable. Cycle stability of bare OPAC (**Figure. 3.10a**) and PMA was also performed for 4000 cycles at six current densities in $0.5\text{M H}_2\text{SO}_4$. To investigate the practical application of the composite material, four pairs of carbon clothes ($4 \text{ cm} \times 4 \text{ cm}$) were coated with OPAC-PMA following the fabrication method described above (160 mg of active electrode material coated), and they were connected in series. Using an electrochemical workstation, we charged a red LED (2V) in a high current density of around 20 A g^{-1} at a potential window 0-3V (**Figure. 3.10c**) and lit them up. The LED continued to glow for the 90s after removing the electrochemical workstation, taking energy from the device, which proves the device's incredible power density.

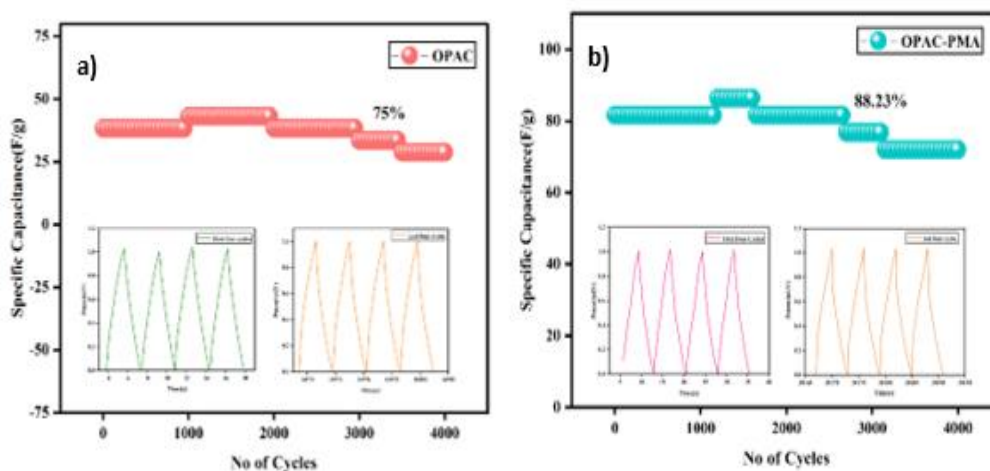


Figure 3.10: The cyclic stability response of (a) OPAC and (b) OPAC-PMA for 4000 cycles at a fixed current density of 6 A g^{-1} and (c) The fabricated supercapacitors are energizing red light-emitting diodes.

3.4 Summary

We successfully suffuse PMA into orange peel-derived activated carbon (OPAC) through an in-situ deposition. At a current density of 1 A g^{-1} , the electrode OPAC-PMA demonstrates a high specific capacitance of 126 F g^{-1} and the highest specific power and energy values, respectively, of 17.55 Wh kg^{-1} and 2000 W kg^{-1} . The OPAC-PMA electrode material has a capacitance value of 66.8% higher than the OPAC electrode. The cycle stability of OPAC-PMA shows 88.23% at 6 A g^{-1} in $0.5\text{M H}_2\text{SO}_4$ electrolyte

for 4000 cycles. Furthermore, the OPAC-PMA electrode can illuminate a red LED bulb for more than a minute.

CHAPTER 4

**High-performance hybrid
supercapacitor immobilized
Wells–Dawson Polyoxometalates
on activated carbon electrodes**

It is becoming increasingly significant to develop the nanofabrication of electroactive hybrid materials for the next generation of energy storage devices as supercapacitor (SC) technology develops rapidly. This describes using activated carbon (AC) templates reinforced with Wells–Dawson Polyoxotungstate (POMs) to produce nanohybrid electrodes for high-performance supercapacitors. This study aims to analyze Wells-Dawson Polyoxotungstate (P_2W_{18}) integrated with AC for the first time and to analyze its structural and electrochemical performances. An aqueous electrolyte containing 0.5M H_2SO_4 was used for the electrochemical studies to characterize the electrochemical performance of symmetric supercapacitors. It was observed that a supercapacitor cell containing the 5 wt% AC- P_2W_{18} hybrid symmetric displayed a noteworthy specific capacitance of $289 F g^{-1}$ and a remarkable energy density of $40 Wh kg^{-1}$. Furthermore, over a period of 4000 cycles, 5 wt% AC- P_2W_{18} symmetric supercapacitor cells showed 89% stability in terms of cyclic stability. Three LED lights were charged onto the electrode. It was observed that the LEDs continued to illuminate continuously for 160 seconds after removing the electrode from the electrochemical workstation, 20 seconds after removing the electrode from the electrochemical workstation, and 10 seconds after removing the electrode from the electrochemical workstation, demonstrating the device's power and energy density.

4. Results and discussion

4.1 Physical Characterization

4.1.1 FTIR

FTIR spectra were recorded on a Bruker 4000 spectrometer (USA) to determine the functional groups and different types of bonds present in the materials. **Figure. 4.1** represents the FTIR spectra of composites with different weight percentages and pure P_2W_{18} . The characteristic chemical bands in all three composite materials and pure P_2W_{18} correlated well with those reported in the literature. (Jarrah and Farhadi 2018) The bands at 1108, 824, 934, and $996 cm^{-1}$ of P_2W_{18} are induced by vibrations of the P–O, W–O_e–W, W–O_c–W, and terminal W=O bonds. C=C stretching causes intensity

bands at 1600 and 1700 cm^{-1} , while the broad peak at 3500–3650 cm^{-1} is due to the –O-H group.

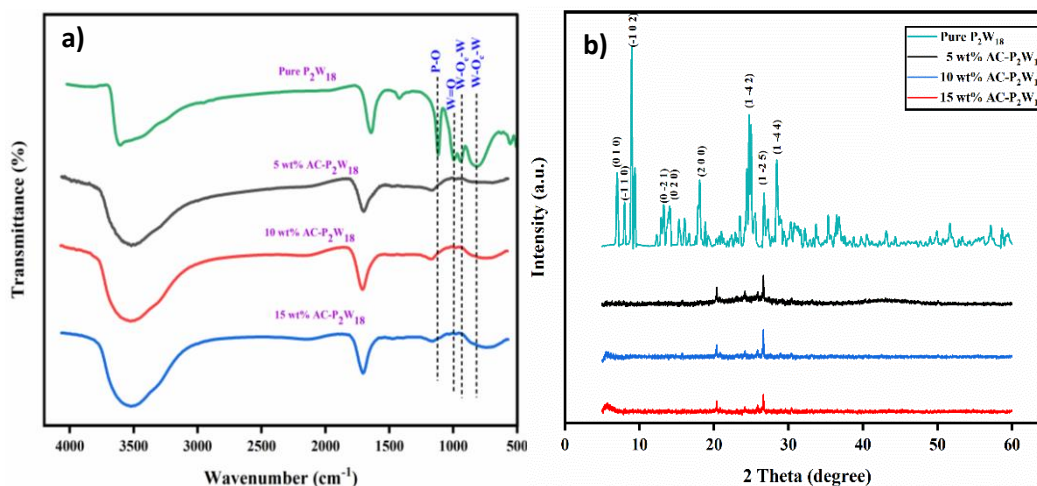


Figure 4.1: a) FTIR image of 5 wt%, 10 wt% and 15 wt% of AC- P_2W_{18} and Pure P_2W_{18} and b) PXRD image of 5 wt%, 10 wt%, 15 wt% of AC- P_2W_{18} and Pure P_2W_{18} .

4.1.2 PXRD

The powder XRD patterns of AC- P_2W_{18} composites of different weight percentages are shown in **Figure 4.1b**. AC exhibits a broad pattern, indicating an amorphous nature. The broad peaks observed at about 24° and 43.8° are due to graphitic carbon (002) and (100), respectively. The crystalline nature of P_2W_{18} has been confirmed from the literature (**Figure 4.1b**) (Jarrah and Farhadi 2018) and JCPDS (card no: 01-073-6183). AC- P_2W_{18} exhibits amorphous and crystalline characteristics as a result of P_2W_{18} being incorporated in AC. The sharp peaks at about 20.35° , 24.13° , 25.85° , and 26.63° are due to P_2W_{18} . Pure P_2W_{18} shows more intense peaks due to its well crystalline nature (**Figure 4.1b**). Conversely, in AC- P_2W_{18} , only a few intense peaks of P_2W_{18} are visible because the carbon content is more in the nanohybrid than P_2W_{18} and exhibits both amorphous and crystalline nature. The diffraction planes (002), (100), and (200) correspond to 2 theta of 24° , 43.8° , and 20.35° , respectively, for AC and P_2W_{18} .

4.1.3 XPS

X-ray photoelectron spectroscopy (XPS, Thermo Fisher Scientific: Nexsa G2base) was used to probe the electronic states of the nanohybrids. **Figure. 4.2** displays the high-resolution XPS spectra of 5 wt% AC- P_2W_{18} . A single strong peak of C1s measured at 285.3 eV, as shown in **Figure. 4.2a**, is consistent with the literature. (Maity et al. 2021) A Gaussian function centered at 531.2 eV, 532.1 eV, and 533.6 eV due to W=O, O–W–O, and O–H, respectively, are satisfactorily fitted to the O1s spectrum (**Figure. 4.2b**) of Wells–Dawson Polyoxometalates, which differs from the fit of Keggin Polyoxometalates. A similar pattern applies to W, which is in the highest oxidation state of +6 (**Figure. 4.2c**), with peaks at 35.68, 37.5, and 42.71 eV, which correspond to $4f_{7/2}$, $4f_{5/2}$, and $5p_{3/2}$, respectively. (Zhu et al. 2019) Finally, a Wells–Dawson anion in P_2W_{18} is attributed to the deconvoluted P $2p_{3/2}$ at 134.2 eV in **Figure. 4.2d**.

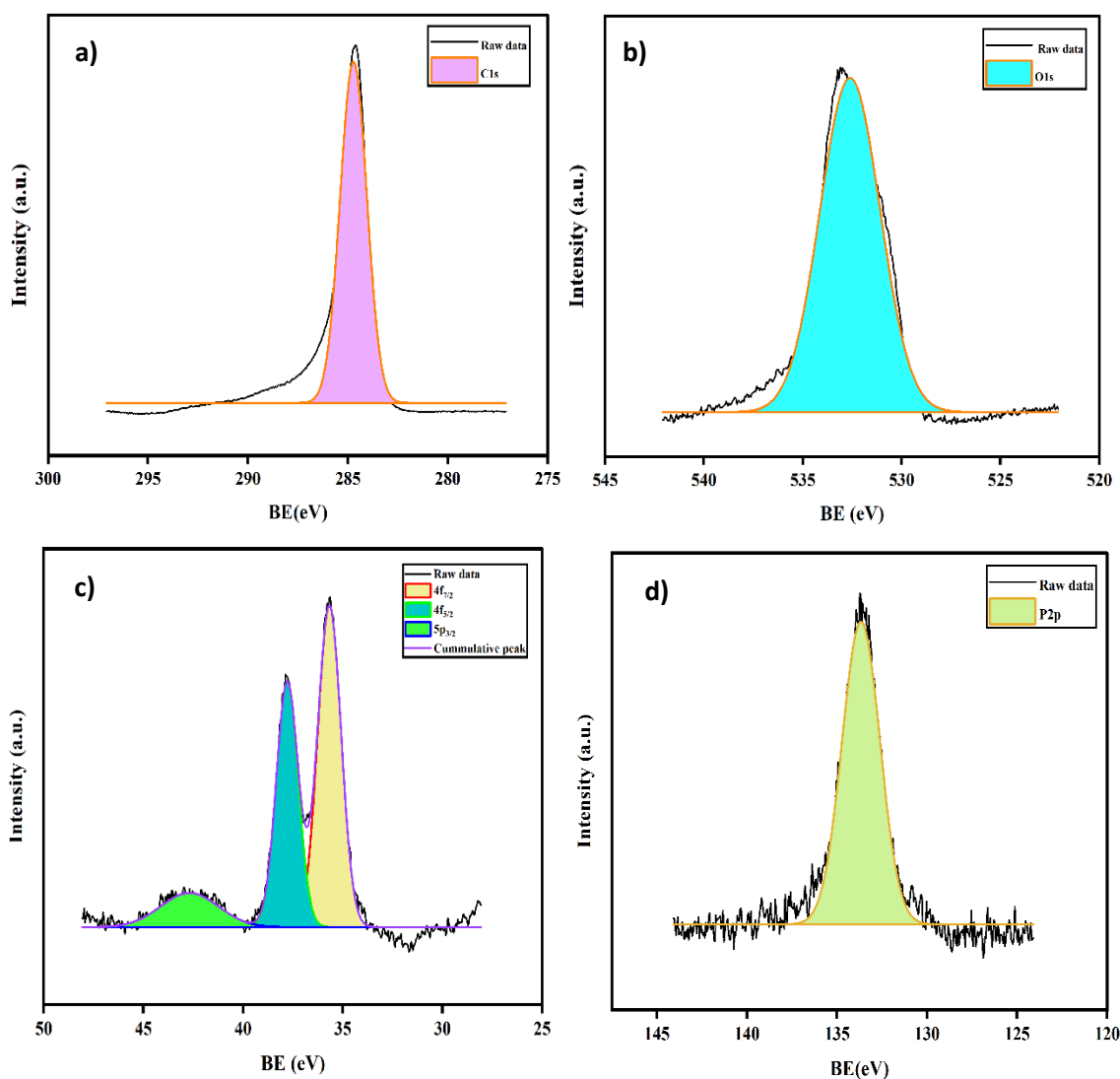


Figure 4.2: XPS Analysis of AC-P₂W₁₈ a) C1s b) O1s c) W4f and d) P2p.

4.1.4 BET

During electrochemical charge storage, electrode materials have an essential role in porosity and surface area. To characterize the AC and 5 wt% AC-P₂W₁₈ nanohybrids, N₂ adsorption/ desorption isotherms data were collected using the Micromeritics physisorption analyzer (Model ASAP 2020, USA). The AC possesses the highest surface area of 1340 m² g⁻¹ with the highest pore volume of 0.37 cm³ g⁻¹ (Table 4.1). A surface area of 1298 m² g⁻¹ and a pore volume of 0.25 cm³ g⁻¹ were observed for 5 wt% AC-P₂W₁₈, which clarifies that P₂W₁₈ is deposited on AC surfaces. The 5 wt% AC-P₂W₁₈ composite exhibited type-IV adsorption–desorption isotherms (Figure 4.3a) with ill-defined hysteresis loops, suggesting the absence or less fraction of mesopores. The step rise in volume adsorbed at low relative pressure indicates the presence of micropores. According to Figure 4.3b, 5 wt% AC-P₂W₁₈ exhibits a pore size distribution peak at a higher pore diameter, indicating the presence of mesopores. As a result, most micropores and some mesopores are covered by P₂W₁₈ on the AC surface.

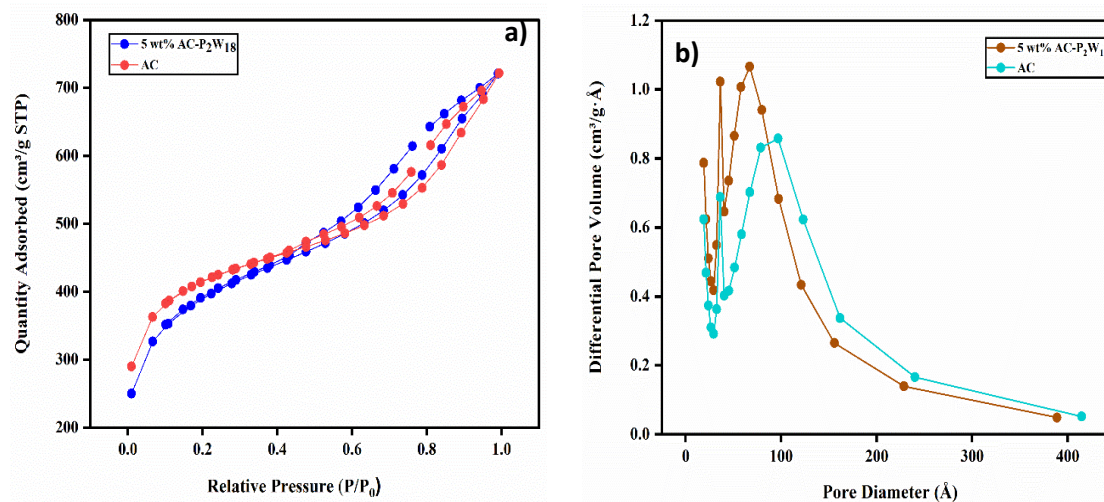


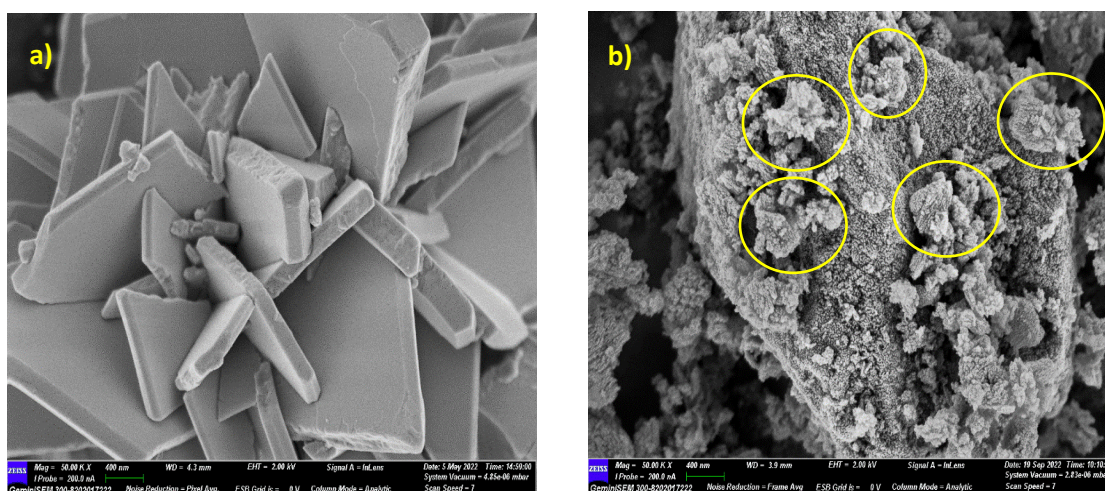
Figure 4.3: a) N₂ Adsorption and Desorption Graph of AC and 5 wt% AC-P₂W₁₈ b) Pore Volume Distribution of AC and 5 wt% AC-P₂W₁₈.

Table 4.1: Surface area and Porosity of 5 wt% AC-P₂W₁₈ nanohybrid and AC.

Sample	BET Surface area (m ² /g)	Micropore Area (m ² /g)	Micropore Volume(cm ³ /g)	Mesopore Width(Å)	Average nanoparticle size (Å)
AC	1339.88	717.4	0.37	33.32	44.78
5 wt% AC-P ₂ W ₁₈	1297.99	487	0.25	34.36	46.22

4.1.5 FESEM

The surface morphology of the nanocomposites was measured by FESEM (FESEM, Carl Zeiss Sigma, Germany). **Figure. 4.4a** and **b** show the FESEM images of pure P₂W₁₈ and 5 wt% AC-P₂W₁₈ nanocomposites. It is clear from **Figure. 4.4a** that the pure P₂W₁₈ has a rock-like structure. The morphological study of pure AC has already been published in the literature by our group. (Vannathan et al. 2022) An analysis of the surface morphology of 5 wt% AC-P₂W₁₈ composite indicates that pure polyanions are inserted into the micropores of AC surfaces. Energy-dispersive spectroscopy (EDS) analysis was also carried out to identify the elements present in the composites. **Figure. 4.4c** shows the confirmed elemental compositions of pure P₂W₁₈ of K, O, P, and W. The elemental compositions of the composites (K, P, O, W, and C) are also confirmed by EDS results (**Figure. 4.4d**).



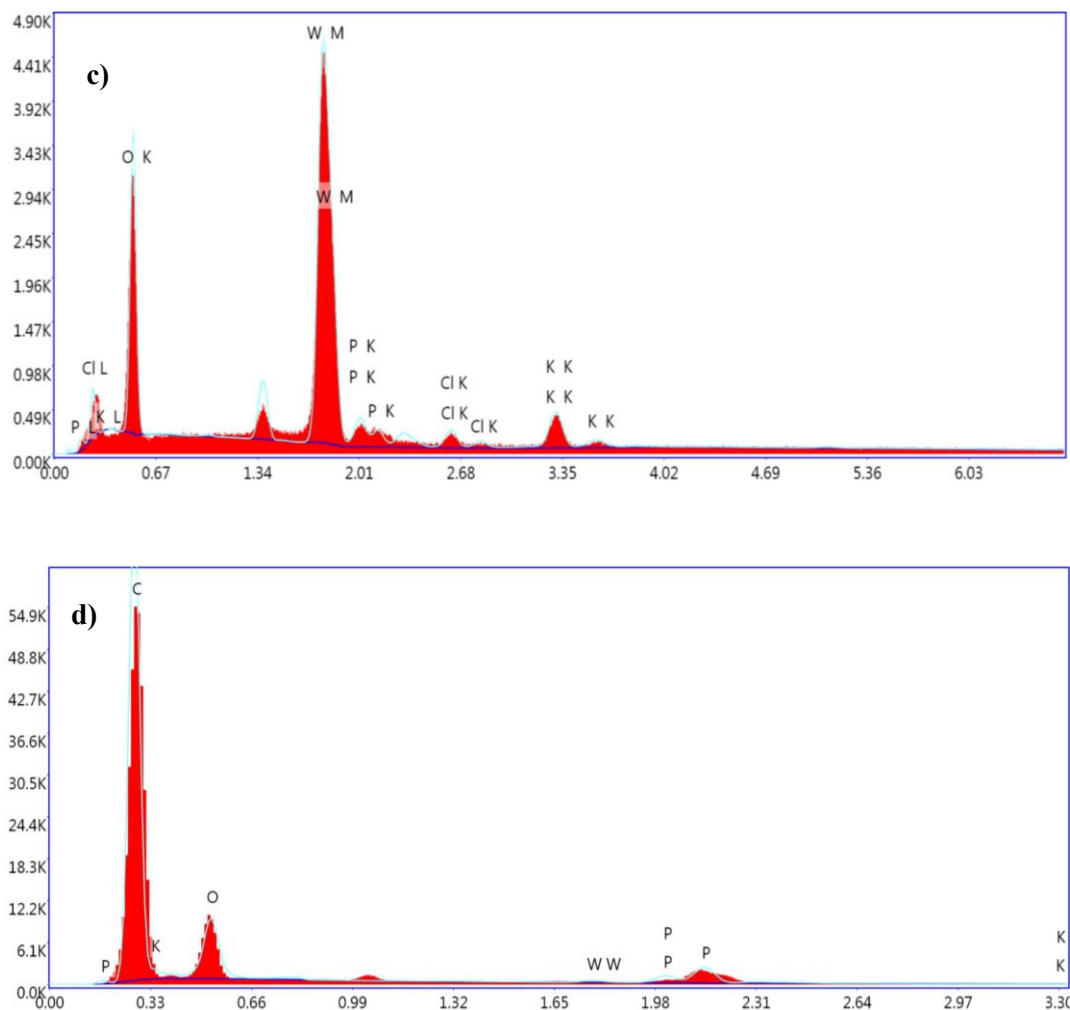


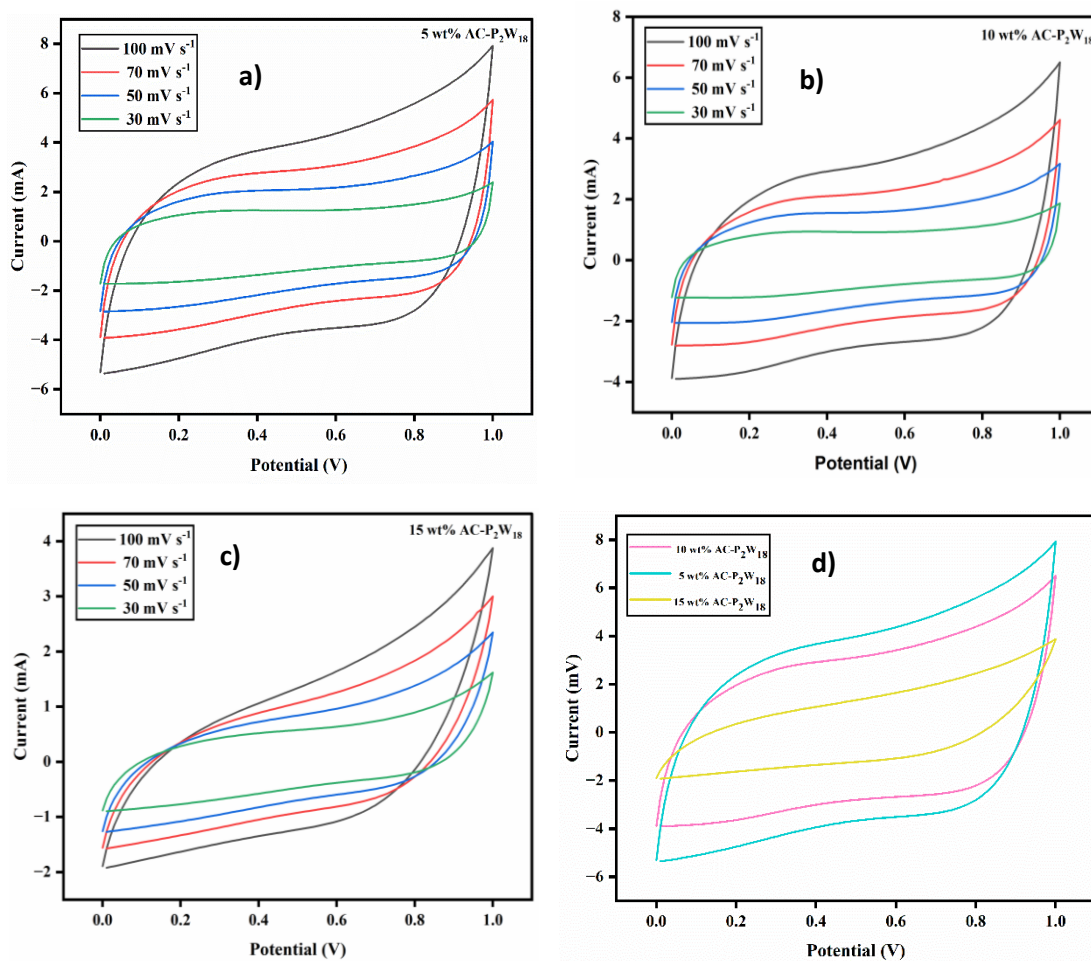
Figure 4.4: a) FESEM image of Pure P₂W₁₈, b) 5 wt% AC-P₂W₁₈ and EDS images of c) Pure P₂W₁₈ and d) 5 wt% AC-P₂W₁₈.

4.2 Electrochemical Studies

4.2.1 CV

A two-electrode system of cyclic voltammetry (CV) method was utilized to explore the electrochemical properties of the power cell. An experiment using cyclic voltammetry (CV) measurements was done to study the electrode material's chemical kinetics, degradation process, and specific capacitance. (Vannathan et al. 2022) The electrodes were tested in a cyclic (IVIUM Technologies BV Co., The Netherlands, Model: Vertex) setup using 5 wt% AC-P₂W₁₈, 10 wt% AC-P₂W₁₈, and 15 wt% AC-P₂W₁₈ composite materials in the potential window of 0–1 V using 0.5M electrolyte

solution at various scan rates. A CV graph measuring 5 wt% AC-P₂W₁₈, 10 wt% AC-P₂W₁₈, and 15 wt% AC-P₂W₁₈ has been presented in **Figure 4.5a–c** at different scan rates of 30, 50, 70, and 100 mV s⁻¹. CV analysis indicates that AC-P₂W₁₈ oxidation-reduction peaks of 5 wt% and 10 wt% indicate that P₂W₁₈ is present over AC surfaces. Notably, 15% AC-P₂W₁₈ shows a deformed curve compared to the other two, 5 wt% AC-P₂W₁₈ and 10 wt% AC-P₂W₁₈. To better understand the pseudo material's exact oxidation-reduction behavior, the bare P₂W₁₈ electrode was also used to perform CV (**Figure 4.5e**) in the same electrolyte at the same scan rate as the pseudomaterial. This indicates that the AC-P₂W₁₈ composite has an excellent capacitive response. An electrode's capacitance can be assessed using CV, such as the shape of the cathodic and anodic peaks and the current density area (**Figure 4.5d**). The specific capacitance of the power cell was calculated by using the **Equation (2.1)**. The specific capacitance increases when P₂W₁₈ is impregnated on AC surfaces.



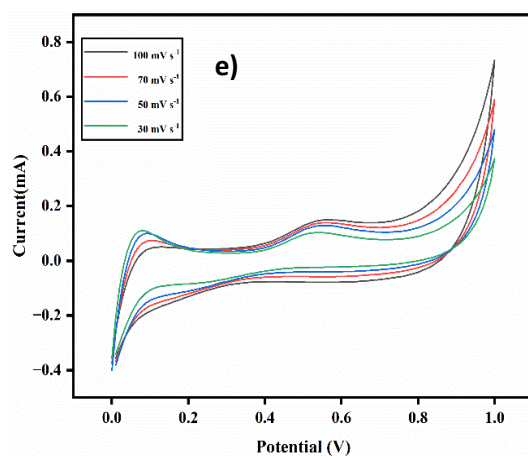
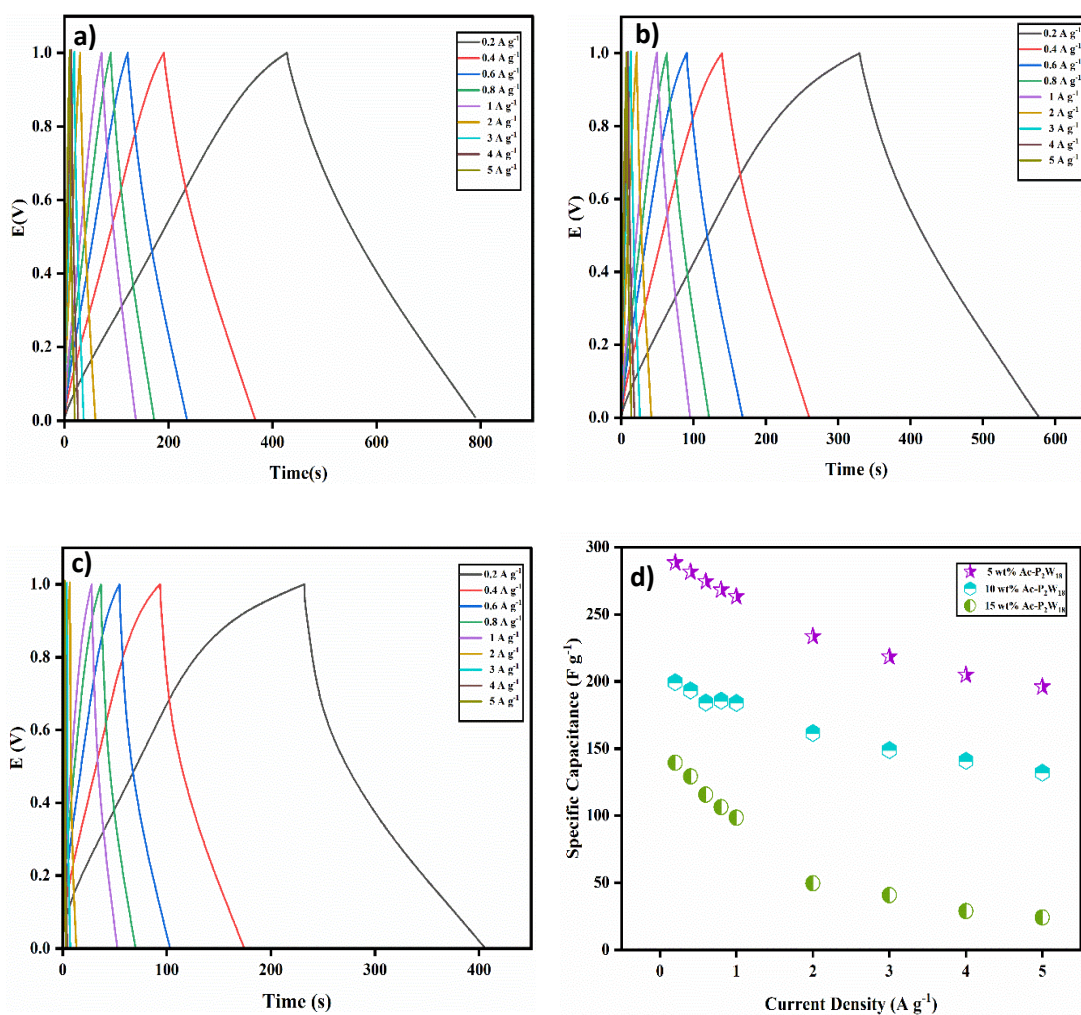


Figure 4.5: Cyclic Voltammetry Graphs a) 5 wt% AC-P₂W₁₈, b) 10 wt% AC-P₂W₁₈, c) 15 wt% AC-P₂W₁₈, d) comparison graph of all three symmetric SC cells and e) Pure P₂W₁₈.

4.2.2 GCD

Galvanostatic charge-discharge (GCD) at several current densities was examined to understand the electrochemical performance of the AC-P₂W₁₈ composite electrode materials under a defined potential window. In a galvanostatic charge and discharge study, three symmetric SC cells were examined with current densities in the range of 0.2 to 5 A g⁻¹ at a potential window of 0-1V. The charge-discharge outline was reshaped by immobilizing POMs onto the AC surface, which differs from EDLC behavior. The improper linear GCD curve was observed across lower current densities (Genovese and Lian 2017). At 0.2 A g⁻¹ current density (**Figure. 4.6a**), the 5 wt% AC-P₂W₁₈ electrode exhibited the specific capacitance of 289 F g⁻¹ with an energy density of 40Wh kg⁻¹. The GCD graphs of 5 wt% AC-P₂W₁₈ have been displayed, resembling the redox reaction while charging and discharging. In order to achieve higher energy density, the device's power must be compromised (Genovese and Lian 2017; Vannathan et al. 2022). In contrast to 10 wt% and 15 wt% of AC-P₂W₁₈, 5 wt% AC-P₂W₁₈ consistently shows high power and energy densities (**Figure. 4.6e**) in the current density range of 0.2 to 5 A g⁻¹. Meanwhile, the GCD response of 10 wt% AC-P₂W₁₈ and 15 wt% AC-P₂W₁₈ were recorded, which shows the specific capacitance value of 199 F g⁻¹ and 139 F g⁻¹ at 0.2 A g⁻¹ current density with specific power and energy density values are 28 Wh kg⁻¹, 1999 W kg⁻¹ and 19 Wh kg⁻¹, 1999 W kg⁻¹, respectively. The composites'

specific capacitance, energy, and power densities were calculated using **Equations 2.2, 2.3, and 2.4**. The GCD graph response of 10 wt% AC-P₂W₁₈ and 15 wt% AC-P₂W₁₈ were displayed in **Figure 4.6 b and c**. Based on the GCD results on three different symmetric SC cells with the same current density, it is concluded that the 5 wt% AC-P₂W₁₈-based electrode had a longer discharge time than the other two electrodes containing 10 wt% AC-P₂W₁₈ and 15 wt% AC-P₂W₁₈, resulting in a higher capacitance value for the former electrode. As a result, surface charge diffusion will be increased, leading to greater capacitance and energy density. In **Figure 4.6d**, specific capacitance versus current and power versus energy density are plotted (**Figure 4.6e**). It is observed that 5 wt% AC-P₂W₁₈ gives high specific capacitance, high energy, and power densities compared to the other two, and it explains that 5 wt% AC-P₂W₁₈ is exactly incorporated onto the AC surface. **Figure 4.6f** illustrates the 5 wt% AC-P₂W₁₈ shows 18% higher capacitance than 10 wt% AC-P₂W₁₈ and 45.5% higher than 15 wt% AC-P₂W₁₈.



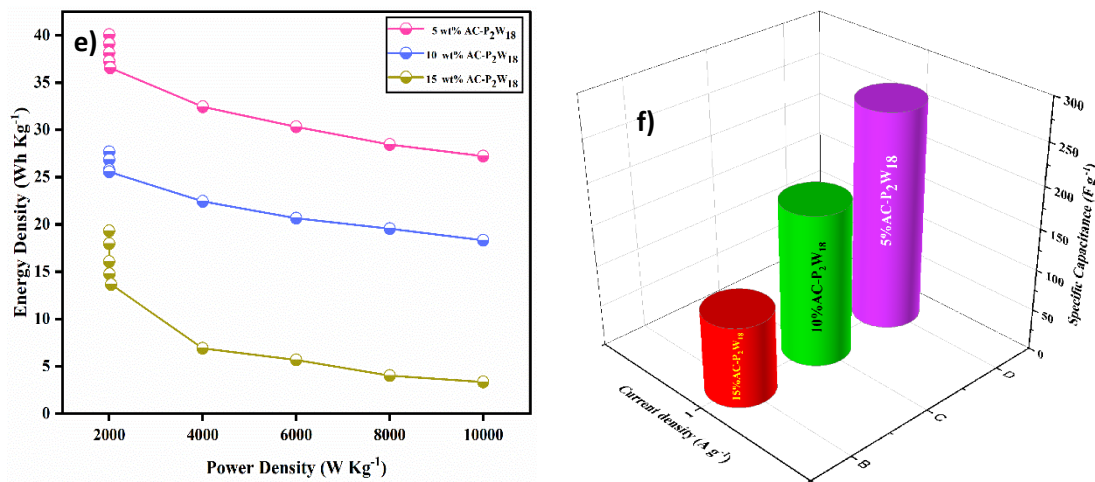


Figure 4.6: GCD graphs of a) 5 wt% AC-P₂W₁₈, b) 10 wt% AC-P₂W₁₈ and c) 15 wt % AC-P₂W₁₈, d) Specific capacitance vs Current Density for 5 wt%, 10 wt% and 15 wt% of AC-P₂W₁₈, e) Ragone plot for all three nanohybrids and f) comparison graph for all three symmetric SC cell.

4.2.3 EIS

Power-cell impedance was measured using a low-amplitude DC potential with electrochemical impedance spectroscopy (EIS). All three concentrations of P₂W₁₈ deposition on AC, AC-P₂W₁₈ nanocomposites, and electrochemical impedance spectroscopy measurements were carried out using a dc potential of 0.01V from 1 Hz to 100 kHz. Nyquist plots can be used to assess the internal resistance of composites, as well as their charge transfer kinetics and ion diffusion processes (Conway and Pell 2003). Impedance spectroscopy results for the high-frequency region show the electrodes to be arranged in a semicircle arc. Low-frequency measurements of electrode-electrolyte impedance provide a visual representation of electron transfer kinetics of redox reactions due to limited mass transport (Zhu et al. 2016, Augustyn et al. 2014). A partial semicircle was observed when the frequency increased, indicating the charge transfer resistance. As shown in **Table 4.2**, all three different concentrations of AC-P₂W₁₈ nanohybrids exhibit equivalent series and charge transfer resistance. In the higher frequency regime, the R_{ct} value is calculated from the diameter of the semicircle in the Nyquist plot (**Figure. 4.7a**). The R_{ct} value of 5 wt% AC-P₂W₁₈ is lower at 3.354 (**Figure. 4.7a**) (**Table 4.2**) than the other two, indicating that the smaller the

electrode diameter, the greater the charge stored (Conway and Pell 2003). Consequently, the 5 wt% AC-P₂W₁₈ electrode has the highest conductivity and kinetics of charging compared to the other two electrodes. In order to determine a supercapacitor device's application, it is essential to consider the cell's stability. Cycle stability has been tested on three symmetric electrodes composed of 5 wt% AC-P₂W₁₈, 10 wt% AC-P₂W₁₈, and 15 wt% AC-P₂W₁₈ (**Figure. 4.7b-d**). As a result, in 4000 cycles at 7 A g⁻¹ for a symmetrical electrochemical system with 5 wt% AC-P₂W₁₈ electrode material (**Figure. 4.7b**), the electrochemical capacitors exhibited outstanding cycle stability of 89%, demonstrating that subsequent cycles do not affect long-term electrochemical capacitors, but are similar to their initial cycle in terms of cycle stability. Based on the fabrication method described above, 5 wt% AC-P₂W₁₈ was coated on four pairs of carbon clothes of 4 cm x 4 cm in dimensions (149 mg of active electrode material coated), which connected in a series. At a potential window of 0-3V (**Figure. 4.7e-g**), the electrode was charged with three LEDs (red, yellow, and blue) at a high current density of around 20 A g⁻¹ in an electrochemical workstation and lit up. After disconnecting the electrochemical workstation, the LED continuously glows red until the 160s, yellow until the 20s, and blue until the 10s after removing it, proving the device's high energy and power density.

Table 4.2: Equivalent circuit elements of all three nanocomposites plotted using Nyquist plots.

Materials	R_s (Ω)	R_p (Ω)	R_{ct} (Ω)
5% AC-P₂W₁₈	1.313	4.667	3.354
10% AC-P₂W₁₈	0.959	5.395	4.435
15% AC-P₂W₁₈	1.528	8.210	6.682

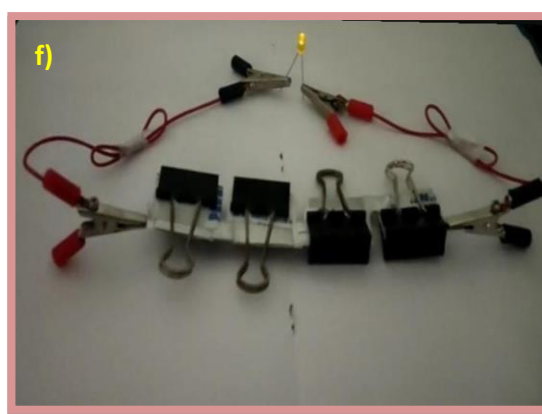
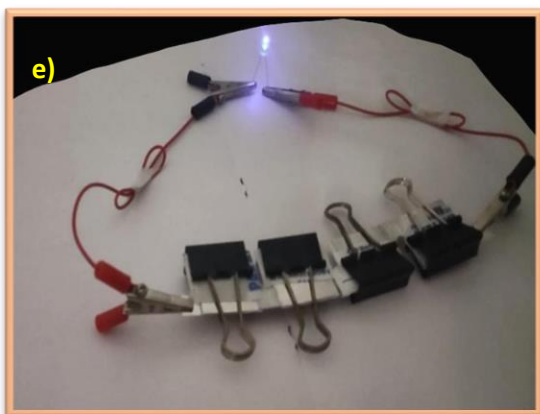
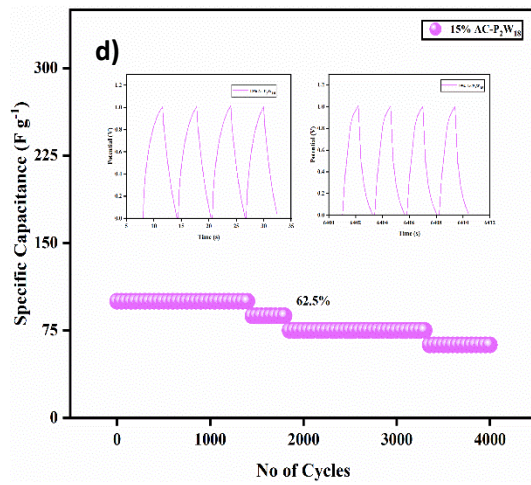
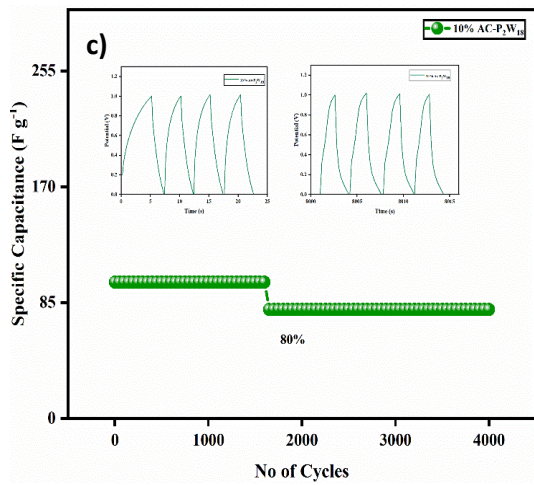
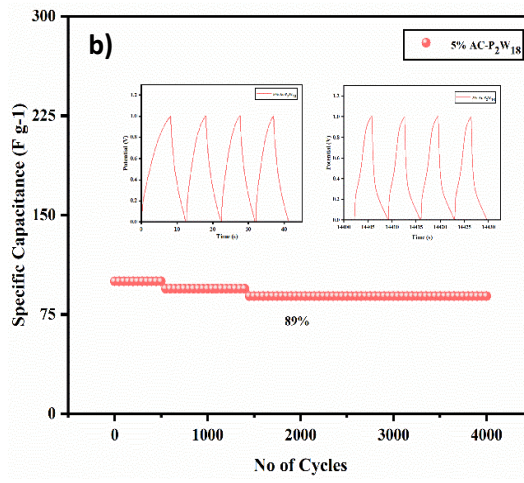
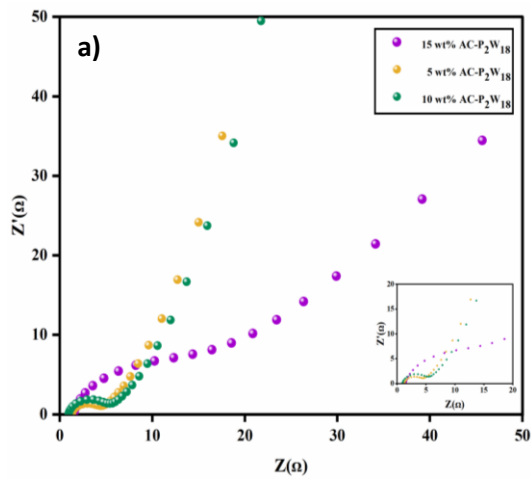


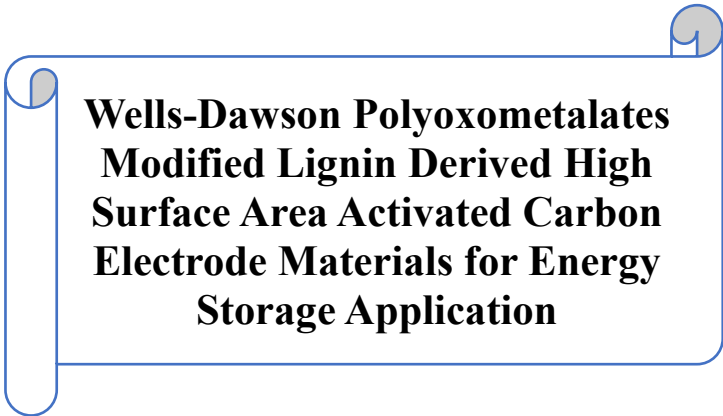


Figure 4.7: a) Nyquist plot and Cyclic stability of b) 5 wt% AC-P₂W₁₈, c) 10 wt% AC-P₂W₁₈ and d) 15 wt% AC-P₂W₁₈ and LED images of e) blue f) Yellow and f) Red light using the 5 wt% Ac-P₂W₁₈ Electrode material.

4.3 Summary

The novel electrode materials were produced in situ using simple adsorption methods. In this study, we developed a Dawson Polyoxometalates (P₂W₁₈) impregnated on AC surface hybrid electrode material for supercapacitor application. Furthermore, symmetric cells like 5% AC-P₂W₁₈, 10% AC-P₂W₁₈, and 15% AC-P₂W₁₈ nanostructures were electrochemically tested in a 0.5M H₂SO₄ electrolyte solution using the two-electrode configuration. The 5% AC-P₂W₁₈ symmetric cell shows an upgraded specific capacitance value of 289 F g⁻¹ with a high energy density of 40 Wh kg⁻¹. The 5% AC-P₂W₁₈ shows superior electrochemical faradic charge storage performance than other symmetric cells, which indicates that P₂W₁₈ is firmly incorporated onto the AC surface. To determine a supercapacitor's application, the 5% AC-P₂W₁₈ electrochemical capacitors achieved cycle stability of 89% over 4000 cycles.

CHAPTER 5



**Wells-Dawson Polyoxometalates
Modified Lignin Derived High
Surface Area Activated Carbon
Electrode Materials for Energy
Storage Application**

This chapter discusses the development of novel nanofabricated electrodes via physisorption by adding vanadium-substituted Wells-Dawson Polyoxometalates (P_2VW_{17}) to activated carbon produced from lignin. The unique nanohybrid materials were carefully investigated for their structural and electrochemical properties. The intrinsic mechanical stability of LDAC improves the conductivity and stability of the POMs. POMs have a high redox potential, which boosts the device's charge storage capability.

5. Results and Discussion

5.1 Structural and Morphological Studies

In order to determine the chemical structure of the materials, FTIR spectra were recorded on a Bruker 4000 spectrometer (USA). **Figure. 5.1** shows the FTIR spectra of composites with different weight percentages, LDAC, and P_2VW_{17} . In all three composite materials, LDAC and P_2VW_{17} , the characteristic IR bands are matched well with those reported in the literature. The FTIR bands of the P_2VW_{17} compound appeared at 1058, 961, 866, 786, and 728 cm^{-1} originated because of the vibration of the P-O, terminal W=O, edge W-O-W, corner W-O-W, and V-O bonds (Harmalkar et al. 1983). The IR bands at 3400 cm^{-1} , 1642 cm^{-1} , and 1101 cm^{-1} confirm the presence of three antagonistic groups of O-H, C=C, and C-O, respectively (Liu et al. 2020).

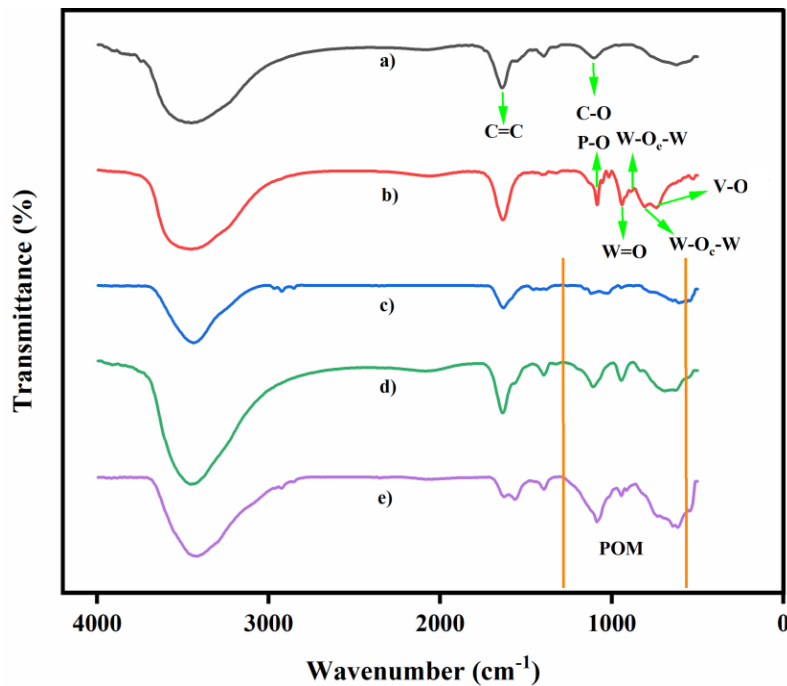


Figure 5.1: FTIR Spectra of a) LDAC, b) P₂VW₁₇, c) 15 wt% of LDAC- P₂VW₁₇, d) 20 wt% of LDAC- P₂VW₁₇ and e) 30 wt% of LDAC- P₂VW₁₇.

Figure. 5.2 displays the powder XRD patterns of LDAC, P₂VW₁₇, and 20 wt% LDAC-P₂VW₁₇. The broad pattern indicates the amorphous nature of pristine LDAC. The peaks observed at approximately 24° and 43.8° are attributed to the graphitic carbon (002) and (100), respectively (Babeł and Jurewicz 2008). The PXRD pattern of P₂VW₁₇ indicates its crystalline nature (Wu et al. 2014). The PXRD pattern of 20 wt% LDAC-P₂VW₁₇ composite represents both amorphous and crystalline nature. The sharp peaks at approximately 18.7°, 28.8°, 35.4°, and 40° are due to P₂VW₁₇, whereas the peaks at around 24° (002) and 43.8° (100) are attributed to the graphitic carbon present in LDAC.

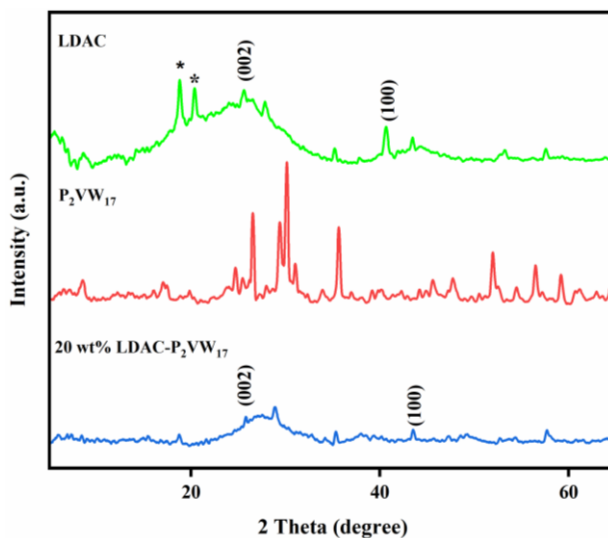
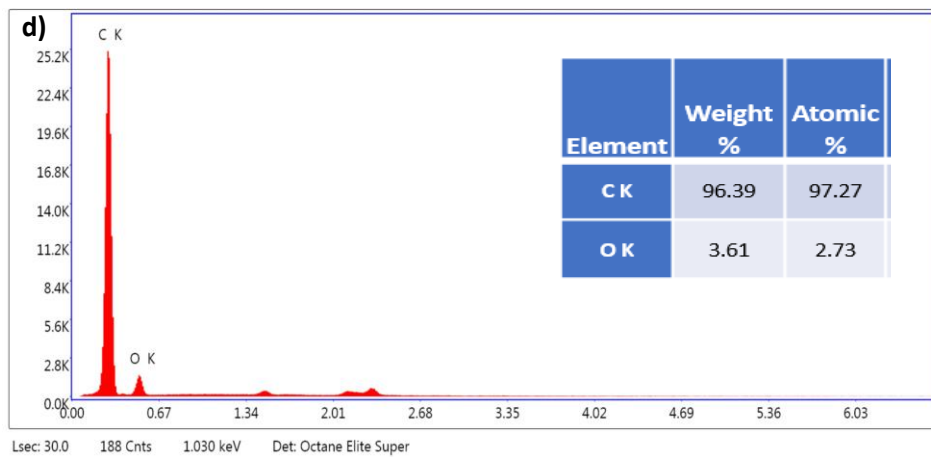
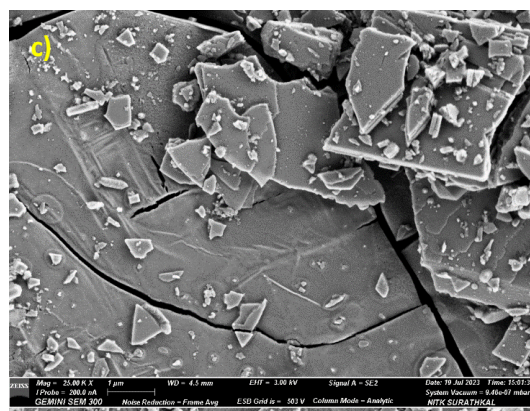
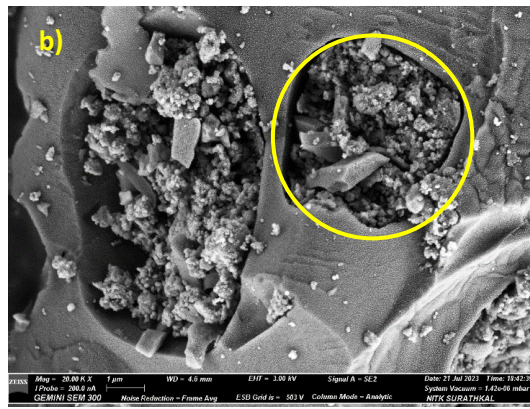
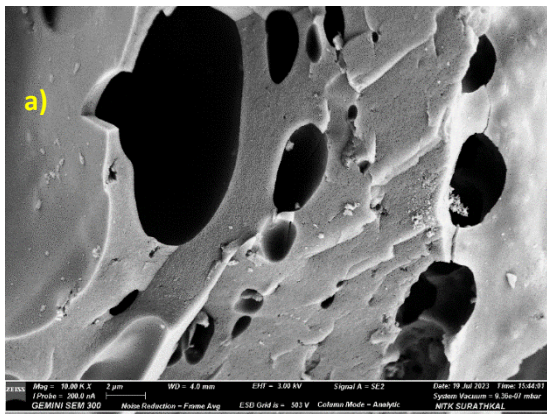


Figure 5.2: PXRD Pattern of LDAC, P₂VW₁₇, 20 wt% of LDAC- P₂VW₁₇,*KOH impurities.

The field emission scanning electron microscope (FESEM, Carl Zeiss Sigma, Germany) was used to analyze the surface morphology of the nanocomposites. **Figure. 5.3(a-c)** illustrates the FESEM images of LDAC, P₂VW₁₇, and 20 wt% LDAC-P₂VW₁₇, respectively. It is evident from the FESEM (**Figure. 5.3a**) images that LDAC has a porous structure with 8.2 μ m, which hosts P₂VW₁₇ polyanion. **Figure. 5.3b** exhibits that P₂VW₁₇ has a rock-like structure. In **Figure. 5.3c**, 20 wt% loaded P₂VW₁₇-LDAC composites show that P₂VW₁₇ polyanions are embedded within the porous surfaces of LDAC. **Figure. 5.3(d-e)** presents the energy dispersive X-ray (EDS) spectra and elemental analysis for P₂VW₁₇, LDAC, and 20 wt% P₂VW₁₇-LDAC nanocomposites. The EDS analysis confirms the presence of all the constituent elements on the LDAC surface.



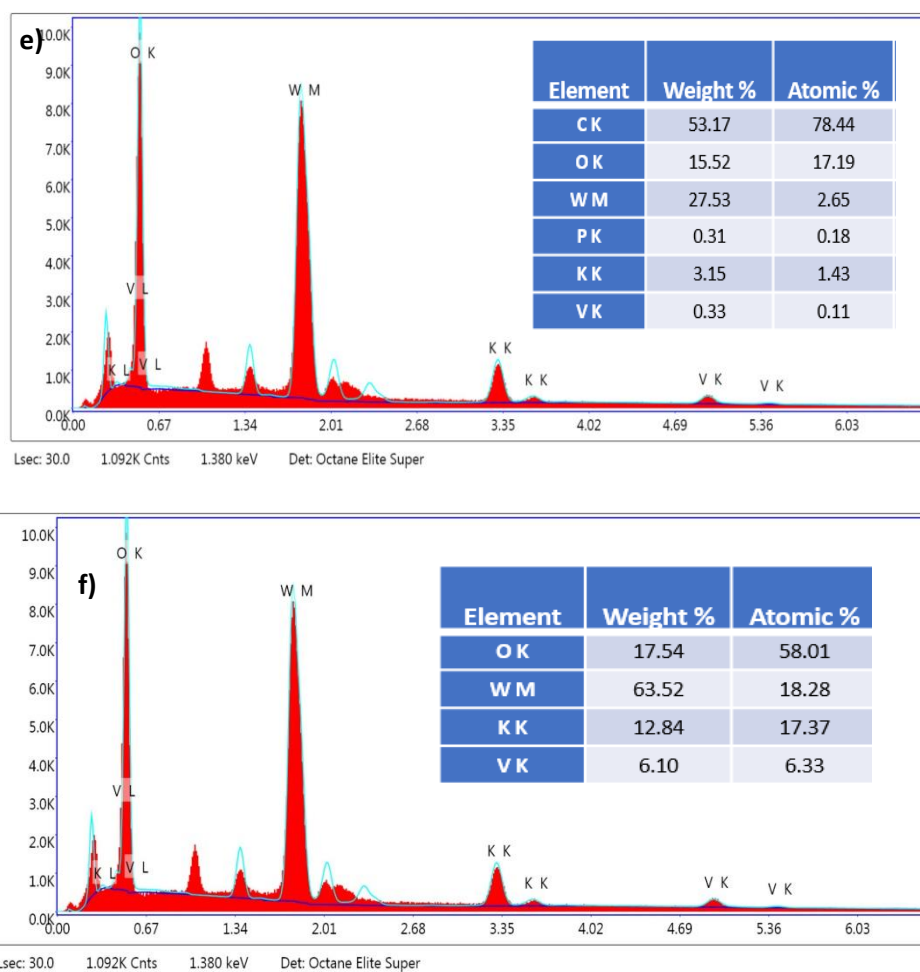


Figure 5.3: FESEM image of a) LDAC, b) P_2VW_{17} , and c) 20 wt% of LDAC- P_2VW_{17} and EDS image d) LDAC e) P_2VW_{17} and f) 20 wt% of LDAC- P_2VW_{17} .

The electronic state of the constituent elements on the surface was determined by the XPS (X-ray photoelectron spectroscopy, Thermofisher scientific: Nexsa G2base) techniques. The XPS spectra of the constituent elements of 20 wt% LDAC- P_2VW_{17} nanocomposites are presented in **Figure. 5.4**. Two peaks were observed in the C1s spectrum of the 20 wt% LDAC- P_2VW_{17} nanocomposite, corresponding to the carbon atoms with different characteristics, such as C=C at 284.5 eV and C-O at 286.4 eV (**Fig 5.4a**) (Arefmanesh et al. 2020). Conversely, the 20 wt% LDAC- P_2VW_{17} nanocomposite exhibited core level peaks of W. The 35.68, 37.5, and 42.71 eV peaks correspond to $4f_{7/2}$, $4f_{5/2}$, and $5p_{3/2}$, respectively (**Figure. 5.4b**) for the W element in the +6-oxidation state (Bai et al. 2020). The peaks observed at BE of 517 eV, 524 eV, and 531 eV, as shown in **Figure. 5.4c**, correspond to $2p_{3/2}$, $2p_{1/2}$, and V-O1s, respectively. These peaks

confirm the presence of vanadium in the composite (Wu et al. 2014; Arefmanesh et al. 2020). Another constituent element phosphorous present in the Wells-Dawson anion, P_2VW_{17} , exhibits a characteristic $2p_{3/2}$ core level peak at 134.2 eV. This indicates the successful deposition of specific chemical composition and structure of the P_2VW_{17} compound (Kasperkiewicz et al. 1983).

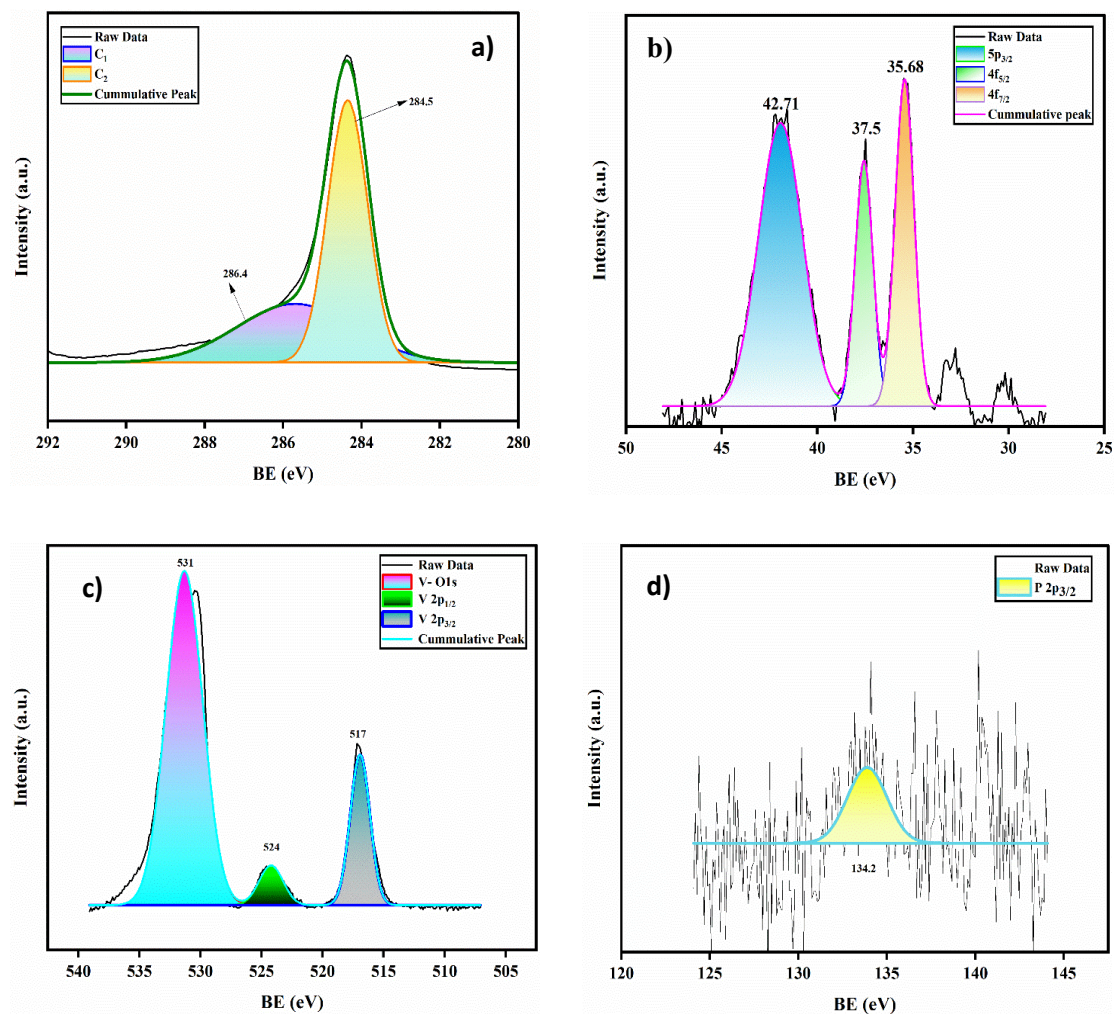


Figure 5.4: XPS Spectra of 20 wt% LDAC- P_2VW_{17} a) C1s b) W4f c) V2p d) P2p.

The N_2 adsorption-desorption isotherm data was collected at 77K in a Micromeritics physisorption analyzer (ASAP 2020, USA). The isotherms of LDAC and 20 wt% LDAC- P_2VW_{17} (Figure. 5.5) exhibit typical Type I isotherms as per IUPAC classification. The sharp uptake of N_2 at low relative pressure represents the microporous nature of both materials. Moreover, deposition of P_2VW_{17} decreases the

specific surface area and micropore volume of the composite, indicating blockage of micropores of LDAC (**Table 5.1**). The specific surface area of LDAC and 20 wt% LDAC-P₂VW₁₇ are 2866.41 m² g⁻¹ and 1940.45 m² g⁻¹, respectively.

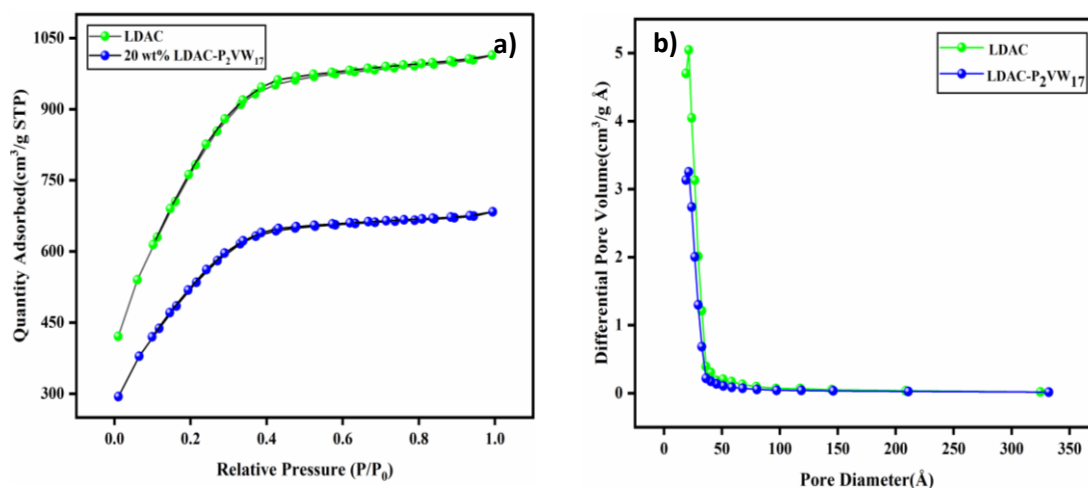


Figure 5.5: a) N₂ adsorption-desorption isotherm of LDAC and 20 wt% LDAC-P₂VW₁₇ and b) Pore size distribution graph.

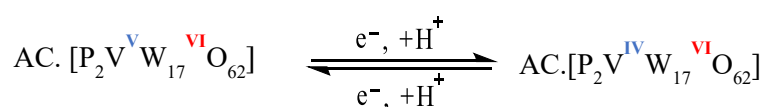
Table 5.1: Surface area and porosity of LDAC and 20 wt% LDAC-P₂VW₁₇.

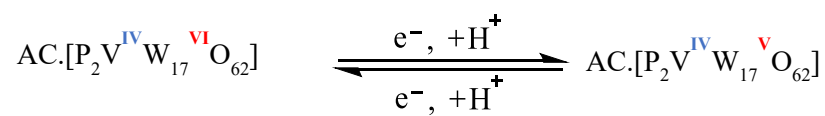
Sample	BET Surface area (m ² g ⁻¹)	Micropore Volume (cm ³ g ⁻¹)	Mesopore Width (Å)	Average nanoparticle size (Å)
LDAC	2866.41	0.37	21.88	20.93
20 wt% LDAC-P ₂ VW ₁₇	1940.45	0.25	21.80	30.92

5.2 Electrochemical Studies

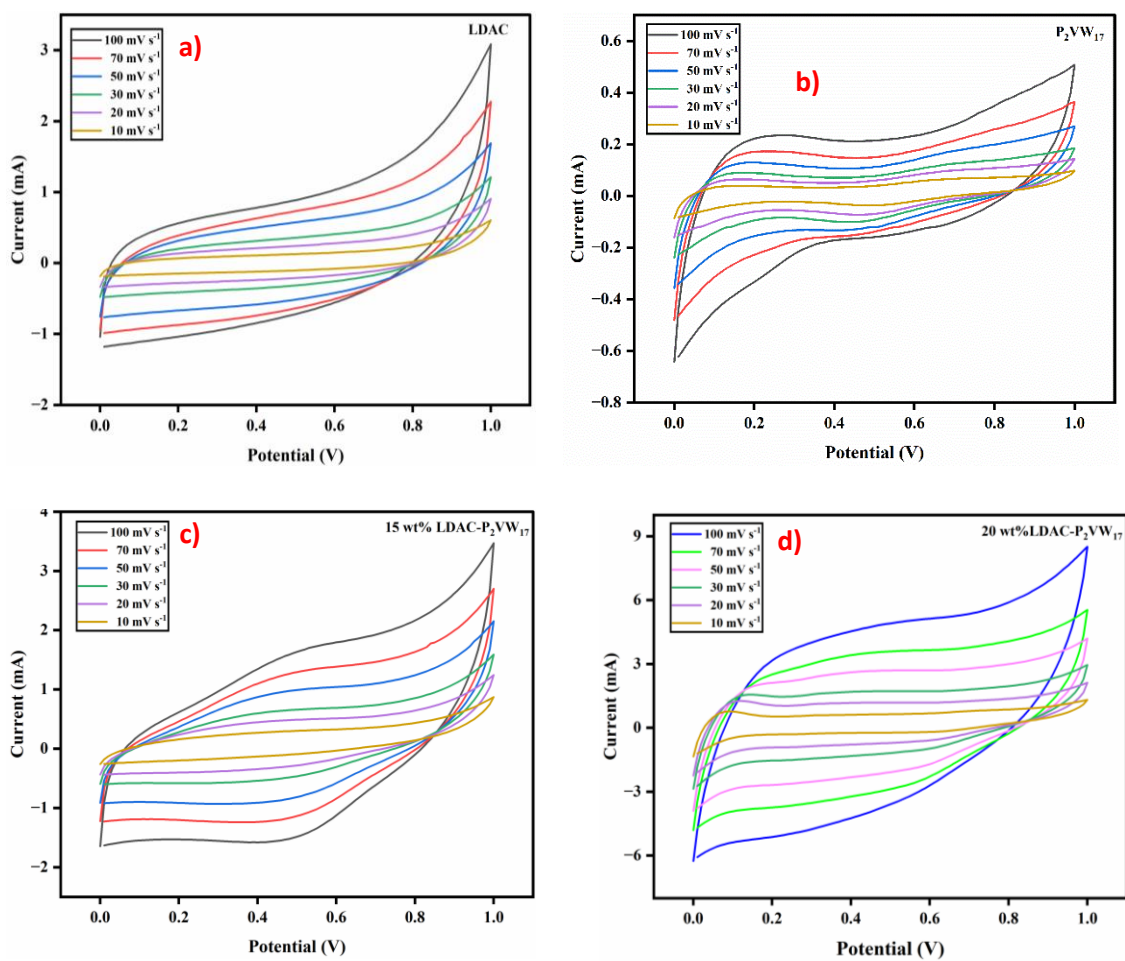
The cyclic voltammetry (IVIUM Technologies BV Co., The Netherlands, Model: Vertex) study was performed using 0.25M H₂SO₄ electrolyte solution in a two-electrode system of all symmetrical electrode materials. In the typical electrochemical study, cyclic voltammetry was conducted as a first step to establish the degradation

mechanism, the chemical kinetics, and the determination of the specific capacitance of electrode material (Zhou and Han 2010; Elgrishi et al. 2018). The cyclic voltammetry (CV) of LDAC, P₂VW₁₇, and various wt% of LDAC-P₂VW₁₇ nanocomposite of varying wt% of P₂VW₁₇ (LDAC-P₂VW₁₇) are represented in **Figure. 5.6** at different scan rates in a symmetric power cell. The near rectangular curve of the CV plot was observed for LDAC (**Figure. 5.6a**), confirming only EDLC contribution and indicating partial ideal behavior. Nevertheless, the irregular rectangular profile of P₂VW₁₇ (**Figure. 5.6b**) suggests the presence of oxidation and reduction peaks of faradaic materials. Alternatively, quasi-rectangular CV curves were observed for different wt% of LDAC-P₂VW₁₇ (**Figure. 5.6(c-e)**), symmetric cells, indicating the simultaneous existence of both charge-storage mechanisms in nanocomposites (EDLC and Faradaic). In charge and discharge processes, the CV curve still shows distinct redox peaks as the scan rate increases, showing good electrochemical reversibility and superior high-rate performance of 20 wt% LDAC-P₂VW₁₇ symmetric cells. **Figure. 5.6d** illustrates the voltammetry peaks for the electrode with 20 wt% LDAC-P₂VW₁₇. This indicates that the electrode is acting as a hybrid material. **Scheme 5.1** shows plausible oxidation/reduction reactions of the nanocomposite materials. As observed in **Figure. 5.6f**, increasing the weight percentage of P₂VW₁₇ in the composite increases its specific capacitance. However, to some extent, as more faradic material is loaded onto the LDAC surface, the specific capacitance decreases of LDAC-P₂VW₁₇ as the loading of P₂VW₁₇ increases. This could be due to either the limited availability of surface area for P₂VW₁₇ or leaching out of P₂VW₁₇ from the surface (Maity et al. 2021). The specific capacitance values for the electrode materials were calculated using **Equation 2.1** and the highest value observed was 85.01 F g⁻¹ for a 20 wt% LDAC-P₂VW₁₇ composite at a scan rate of 10 mV s⁻¹. However, at a higher loading of 30 wt%, the specific capacitance decreased to 58.07 F g⁻¹ due to the increased accumulation of P₂VW₁₇ on the LDAC surface. The specific capacitance versus scan rate for the various weight percentages of the LDAC-P₂VW₁₇ composite is shown in **Figure. 5.4f**.





Scheme 5.1: Plausible reduction mechanism for P₂VW₁₇ immobilized on LDAC surface.



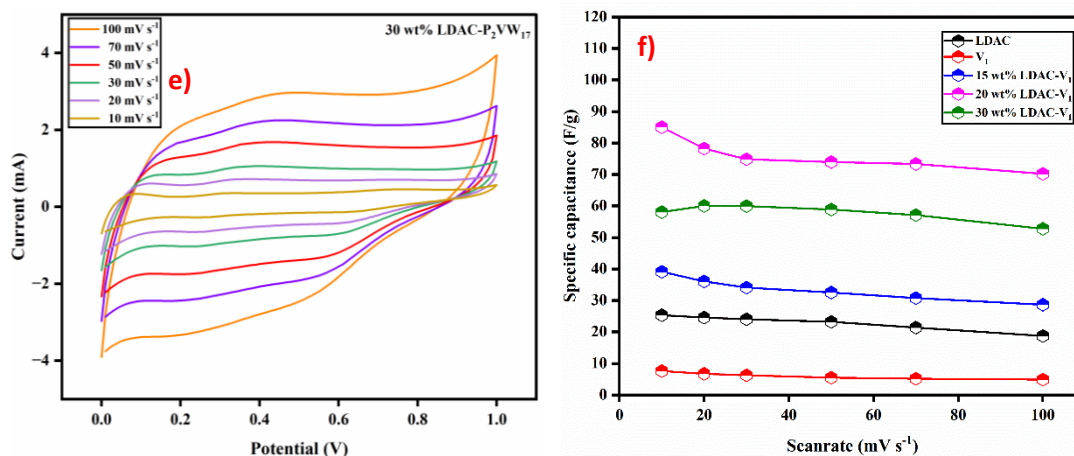
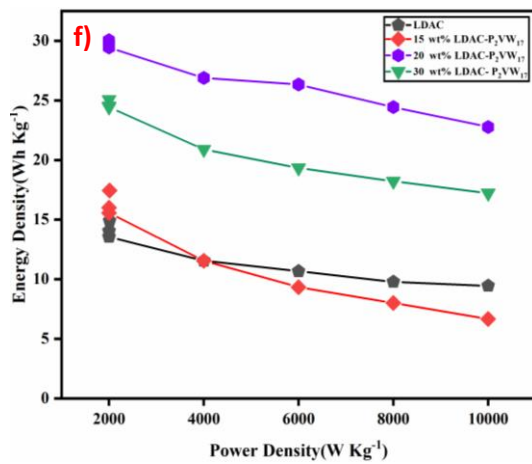
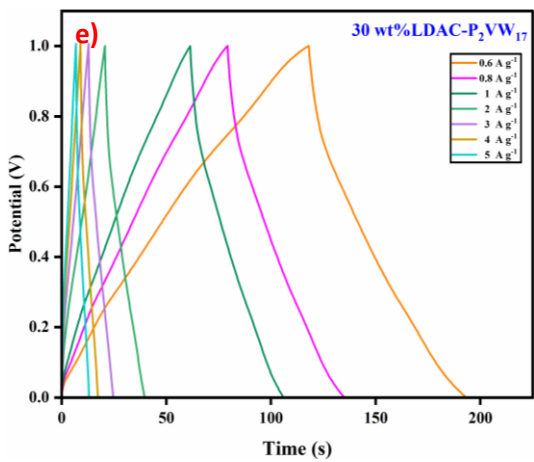
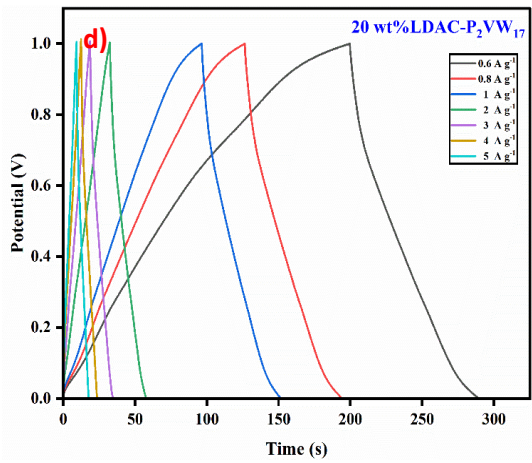
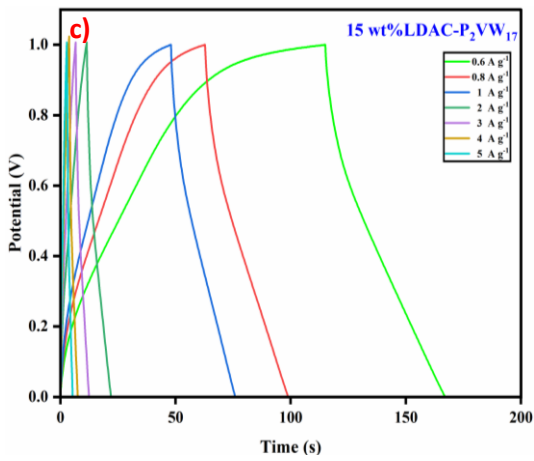
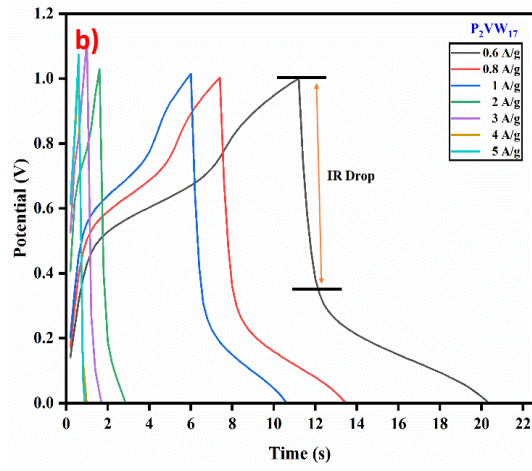
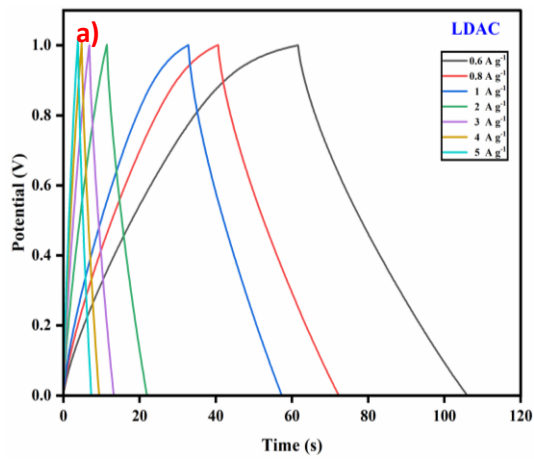


Figure 5.6: Cyclic Voltammetry graph of a) LDAC, b) P₂VW₁₇, c) 15 wt% LDAC-P₂VW₁₇, d) 20 wt% LDAC-P₂VW₁₇, e) 30 wt% LDAC-P₂VW₁₇ and f) comparison graph of specific capacitance vs. scan rate.

The electrochemical performance of all symmetric electrode cells was examined through galvanostatic charge and discharge studies at several current densities under a defined potential window of 0-1V in a two-electrode cell configuration. The galvanostatic charge-discharge responses of a symmetric cell configuration were analyzed to determine the performance of LDAC-P₂VW₁₇ nanocomposites with 15, 20, and 30 wt%, as well as LDAC and P₂VW₁₇ with various weight percentages, as shown in **Figure 5.7**. During the charge-discharge measurement, the supercapacitor cell is charged with a persistent current until it reaches its maximum potential. After discharging with the same current, it drops over the minimum voltage range (Momodu et al. 2017). The GCD curves of LDAC are exactly triangular, while charging and discharging maintain a linear curve, indicating EDLC behavior, a non-faradic process (**Figure 5.7a**). However, for P₂VW₁₇ material, the curves are not perfectly triangular (**Figure 5.7b**) because the electrode material contains a redox-active component that changes from reduction during charging to oxidation when discharging. Different weight percentages of LDAC-P₂VW₁₇ (**Figure 5.7(c-e)**) nanocomposites show a slight non-triangular curve due to the synergic combination of non-faradic (LDAC) and faradic (P₂VW₁₇) behavior. This results in greater specific capacitance values while sustaining higher specific energy and power levels. **Equation 2.2** was used to assess the galvanometric measurement of each symmetric supercapacitor. The 20 wt% of

LDAC-P₂VW₁₇ offered the highest capacitance value of 216.48 F g⁻¹ at 0.6 A g⁻¹ current density (**Figure. 5.7g**), significantly higher than the values obtained from 15 wt% of LDAC-P₂VW₁₇ (125.6 F g⁻¹) and 30 wt% of LDAC- P₂VW₁₇ (180.48 F g⁻¹). The 20 wt% LDAC-P₂VW₁₇ shows a higher specific capacitance value than others because of the even distribution of P₂VW₁₇ in the LDAC structure, which could be the reason for providing the high surface area for charge diffusion. Using **Equation 2.3**, all symmetric LDAC-P₂VW₁₇ nanocomposite's specific energy densities were calculated. The 20 wt% of LDAC- P₂VW₁₇ showed a higher energy density of 30.06 Wh kg⁻¹ as compared to 15 wt% LDAC-P₂VW₁₇ (17.44 Wh kg⁻¹) and 30 wt% LDAC-P₂VW₁₇ (25.06 Wh kg⁻¹). The specific power density of LDAC-P₂VW₁₇ symmetric cells for different concentrations was calculated using **Equation 2.4**. The 20 wt% of LDAC-P₂VW₁₇ showed a higher power density of 1999.97 W kg⁻¹ compared to 15 wt% LDAC-P₂VW₁₇ (1997.45 W kg⁻¹) and 30 wt% LDAC-P₂VW₁₇ (1995.2 W kg⁻¹). **Figure. 5.7f** presents a graphical representation of the relationship between specific capacitance and current density for LDAC-P₂VW₁₇ cells with varying compositions. Due to limited ion mobility in the electrolyte, which reduces the amount of time that ions have to interact with the electrode material, the discharge time reduces as the current density rises. At lower current density, the discharge time increases because ions will generate more in the electrolyte (Bohinc et al. 2001). P₂VW₁₇ polyanions are dispersed through the LDAC surface at a lower concentration of 15 wt%. However, with a concentration of 20 wt%, the specific capacitance rises, demonstrating the potential of uniform dispersion over the LDAC surface. In contrast, at 30 wt%, the deposition of P₂VW₁₇ leads to the accumulation of metal oxides. During the charge-discharge process, the polyanions can easily detach from the surface due to weaker electrostatic attraction. This phenomenon contributes to the dynamic behavior of the LDAC- P₂VW₁₇ cells. **Figure. 5.7f** illustrates the Ragone plot, which provides insights into different compositions' specific energy and power. The coulombic efficiency (**Fig 5.7 (h-j)**) of all nanocomposites was calculated by **Equation 2.5**.



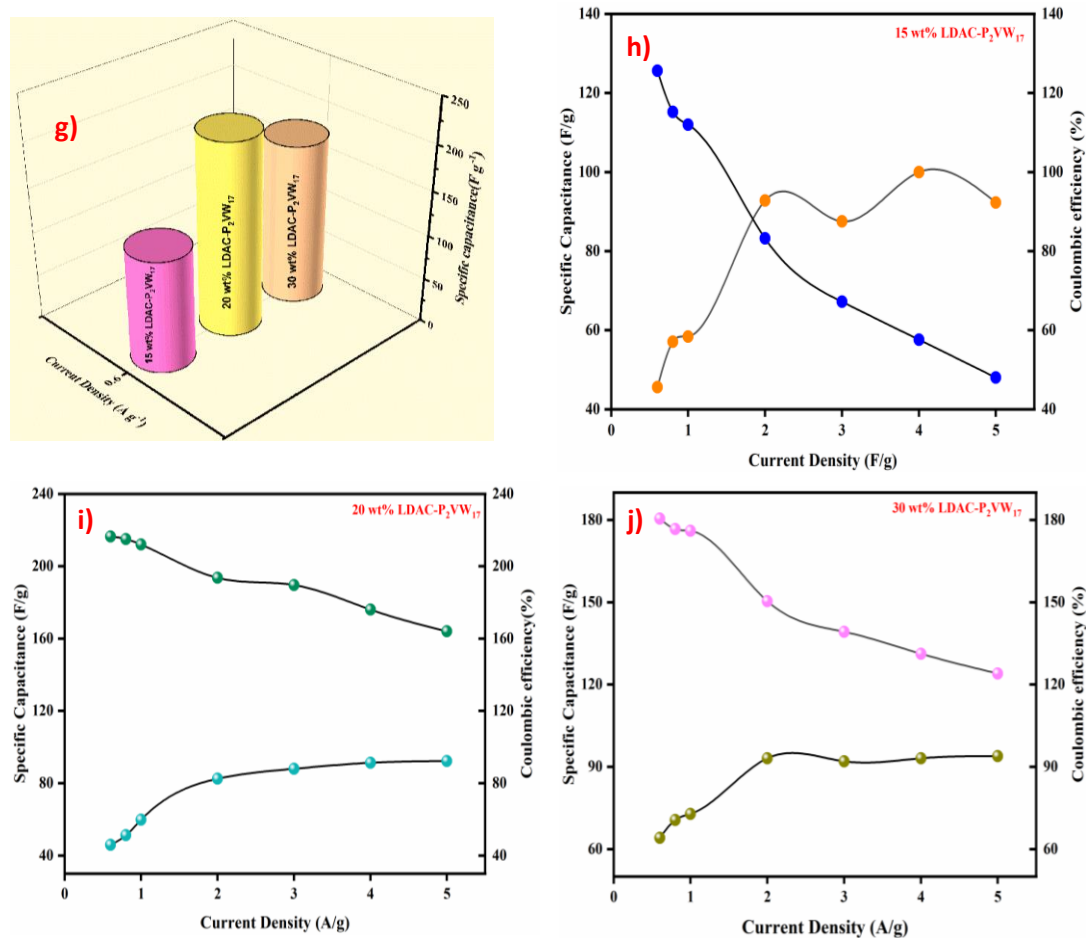


Figure 5.7: Galvanostatic charge and discharge graph of a) LDAC, b) P₂VW₁₇, c) 15 wt% LDAC-P₂VW₁₇, d) 20 wt% LDAC-P₂VW₁₇, e) 30 wt% LDAC-P₂VW₁₇, f) Ragone plot, g) Comparison graph of different wt% of LDAC-P₂VW₁₇, and Specific capacitance and Coulombic efficiency vs current density graph of h) 15 wt% LDAC-P₂VW₁₇, i) 20 wt% LDAC-P₂VW₁₇, j) 30 wt% LDAC-P₂VW₁₇.

In order to study the electron transfer kinetics of the redox process at the electrode-electrolyte interface using the Nyquist plot, electrochemical impedance spectroscopy was carried out for all nanohybrids. **Figure 5.8a** shows the Nyquist plot denotes a semicircular curve in the high frequency region and a straight line in the low-frequency region. An electron-transfer-limited process is indicated by a semicircle-shaped in the high-frequency region, where the resistance is attributed to the charge transfer resistance (R_{ct}). On the other hand, at the low frequency region, the linear portion depicts the diffusion-limited electron transfer mechanism (Augustyn et al. 2014; Conway and Pell 2003). Generally, the larger the arc, the more excellent the resistance

between the electrode and electrolyte. Further, the electrode material has additional capacitive properties that contribute to the sharp response of the lower frequency region. **Table 2** illustrates calculated values for different weight percentages of LDAC-P₂VW₁₇ in which R_s represents the solution resistance, R_p is the polarized resistance, and R_{ct} is the charge transfer resistance. The charge transfer resistance (R_{ct}) of 20 wt% LDAC-P₂VW₁₇ has a lower resistance of 4.583(Ω) than the other electrodes with 15 wt% LDAC-P₂VW₁₇ (6.011(Ω)) and 30 wt% LDAC-P₂VW₁₇ (6.777 (Ω)). The uniform distribution of P₂VW₁₇ on the LDAC surface contributes to an increased number of redox-active sites in the 20 wt% LDAC-P₂VW₁₇ compared to other materials. This higher concentration of redox-active sites enhances the conductivity nature of LDAC-P₂VW₁₇ and reduces its resistance. The Zswipwim (3.21) software was used to fit the equivalent series circuit (**Figure. 5.8b**), here the solution resistance denotes R_s , capacitances denoted as C_1 & C_2 , R_1 & R_2 represent resistances, and T represents the time constant.

Table 5.2: Fitted data from Nyquist plots of equivalent circuit elements of LDAC-P₂VW₁₇ of 15 wt%, 20 wt%, and 30 wt%.

Electrode Material	R_s (Ω)	R_p (Ω)	R_{ct} (Ω)
15 wt% LDAC-P ₂ VW ₁₇	0.901	7.217	6.011
20 wt% LDAC-P ₂ VW ₁₇	0.684	5.268	4.583
30 wt% LDAC-P ₂ VW ₁₇	0.568	7.346	6.777

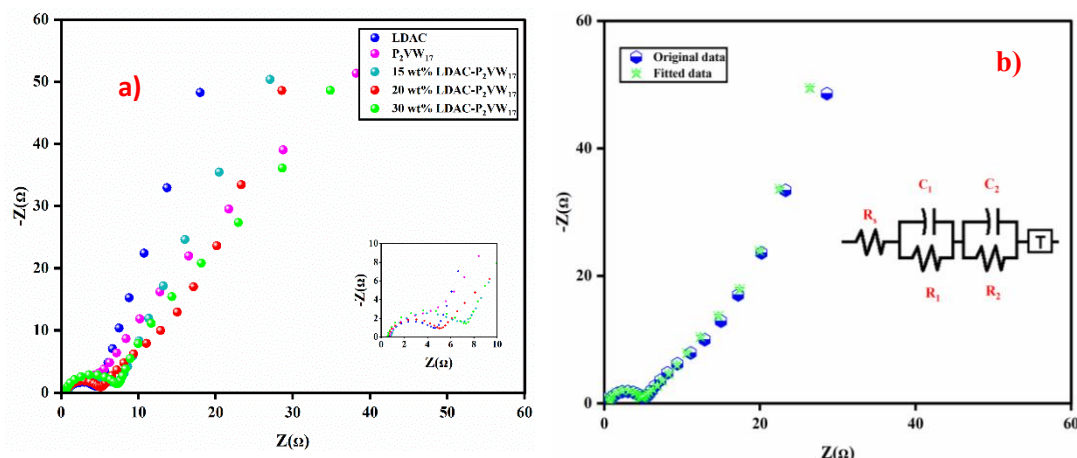
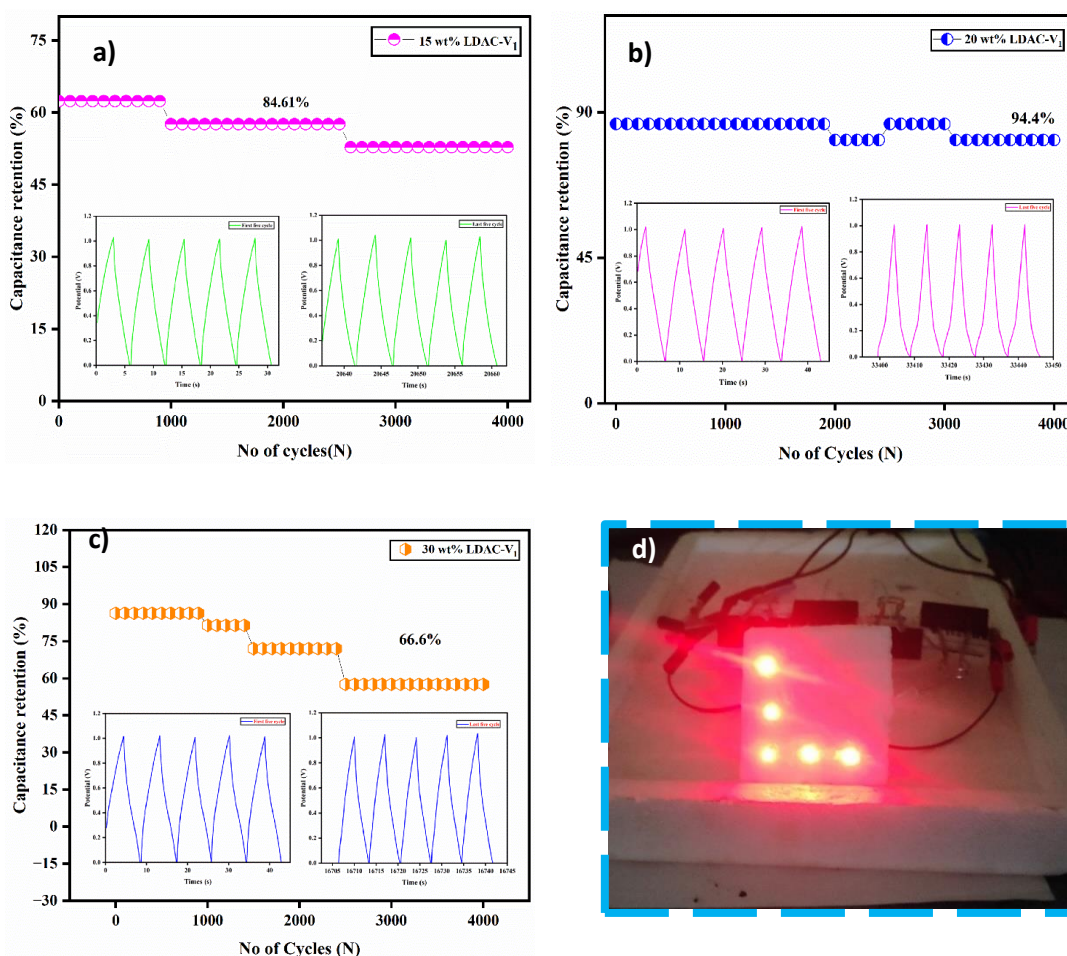


Figure 5.8: a) Nyquist plot and b) Fitted Nyquist plot require an equivalent circuit.

5.3 Cyclic Stability

The capacity retention of a supercapacitor can be determined by determining the cycle stability of the Cell. Cycle stability has been tested on all the different percentages of LDAC-P₂VW₁₇ composite, like 15 wt% LDAC-P₂VW₁₇, 20 wt% LDAC-P₂VW₁₇, and 30 wt% LDAC-P₂VW₁₇ (**Figure. 5.9(a-c)**) Cell using a symmetrical electrode configuration. Thus, in a symmetrical electrochemical system with a 6 A g⁻¹ current, the 20 wt% LDAC-P₂VW₁₇ composite shows a very high degree of stability retention of 94.4% over 4000 cycles, demonstrating that subsequent cycles do not affect long-term electrochemical capacitor performance but is similar to the initial cycle in terms of cycle stability. A 4000-cycle test with 15 wt% LDAC-P₂VW₁₇ cells and 30 wt% LDAC-P₂VW₁₇ cells resulted in capacitance retention of 84.6% and 66.6%, respectively. All three symmetric arrangements could still be well-loaded with P₂VW₁₇ polyanions even after being swept for a large number of charge-discharge cycles within the LDAC surface. It is evident from the above results that the 20 wt% LDAC-P₂VW₁₇ nanohybrid composite has the required mechanical durability and stability to be used as a SC electrode material. This composite is an excellent alternative option for using practical energy storage devices. As a practical application test of the composite material, four pairs of carbon clothing (2 cm x 2 cm) were coated with 20 wt% LDAC-P₂VW₁₇ according to the fabrication method described above (80 mg of active electrode material coated) and connected in series. An electrochemical workstation was used to charge a series of red LEDs (2V) and to light them up at a potential window of 0–3V (**Figure.**

5.9d). In addition to charging the device for 30 seconds, the series of LEDs continued to glow for 30 seconds, using energy from the device, assuring the device's remarkable power density. The LEDs were switched between red(2V), green(3V), and blue(3V) (**Figure. 5.9e**). After disconnecting the electrochemical workstation, the LEDs continued to glow continuously red for 120 seconds, green for 60 seconds, and blue for 50 seconds. A piezoelectric buzzer (3V) (**Fig 5.9f**) was then used. Once the buzzer was connected to the electrochemical workstation, it sounded for 140 seconds.



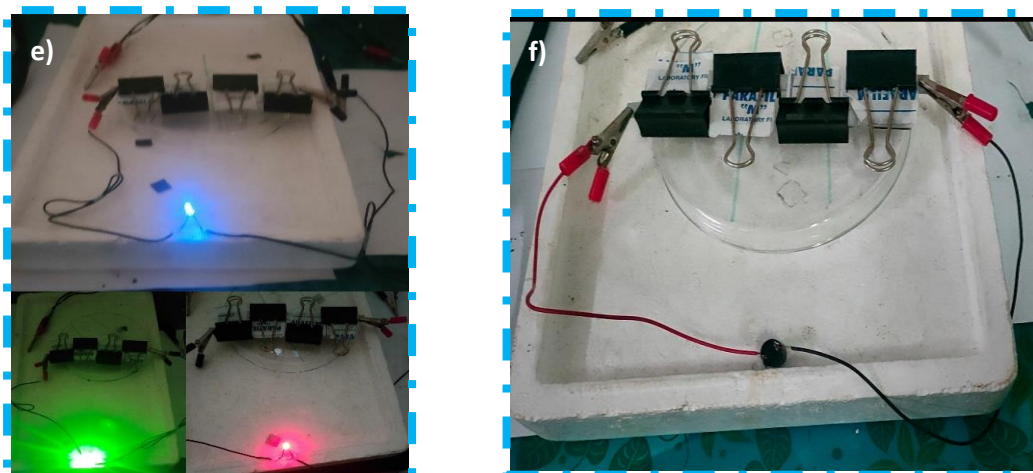
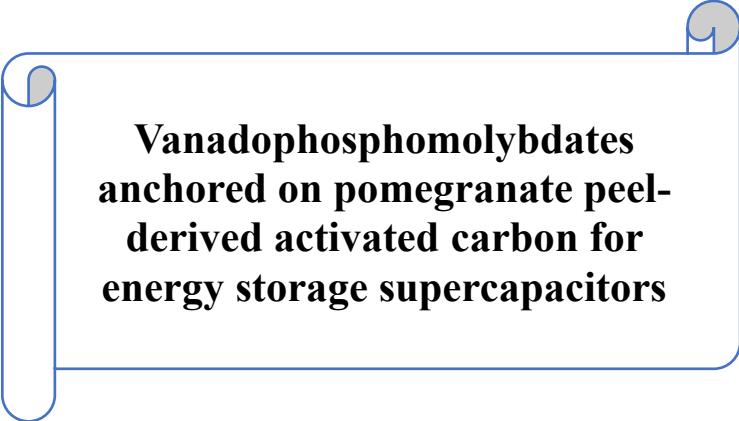


Figure 5.9: Cyclic stability of a) 15 wt% LDAC-P₂VW₁₇, b) 20 wt% LDAC-P₂VW₁₇, c) 30 wt% LDAC-P₂VW₁₇, realistic application of 20 wt% LDAC-P₂VW₁₇ d) Series LED image, e) Red, Blue, Green LED image and f) piezoelectric buzzer image.

5.4 Summary

Novel nanohybrids were prepared using a simple deposition method, where P₂VW₁₇ polyanion is infused on LDAC surface in different weight percentages like 15, 20, and 30 wt%, as confirmed by various analytical techniques. Electrochemical analyses were conducted on all nanohybrids. In that, 20 wt% LDAC-P₂VW₁₇ showed excellent specific capacitance of 216.48 F g⁻¹ at 0.6 A g⁻¹ current density in 0.25M H₂SO₄ electrolyte. Furthermore, 20 wt% LDAC-P₂VW₁₇ displays more energy and power densities of 30.06 Wh kg⁻¹ and 1999.98 W kg⁻¹ than other nanohybrids. The cyclic retention studies demonstrated that the 20 wt% LDAC-P₂VW₁₇ electrode material retained 94.4% specific capacitance over 4000 charge-discharge cycles. Furthermore, the real-world application of the fabricated 20 wt% LDAC-P₂VW₁₇ cell was performed in a series of LEDs, which took 30 seconds to discharge. A piezoelectric buzzer sounded for 140s.

CHAPTER 6



**Vanadophosphomolybdates
anchored on pomegranate peel-
derived activated carbon for
energy storage supercapacitors**

This chapter probes into the innovation of nanofabricated electrodes through the integration of two distinct polyanions: the vanadium-substituted Wells-Dawson polyanion (P_2VMO_{17}) and the vanadium-substituted Keggin polyanion ($PVMO_{11}$), into activated carbon derived from pomegranate peel (PDAC). These novel nanohybrid materials were methodically examined to uncover their structural and electrochemical characteristics. The inherent mechanical robustness of PDAC enhances both the conductivity and the stability of the polyanions. Moreover, the polyanions exhibit a high redox potential, significantly enhancing the charge storage capacity of the device.

6. Results and Discussion

6.1 FTIR

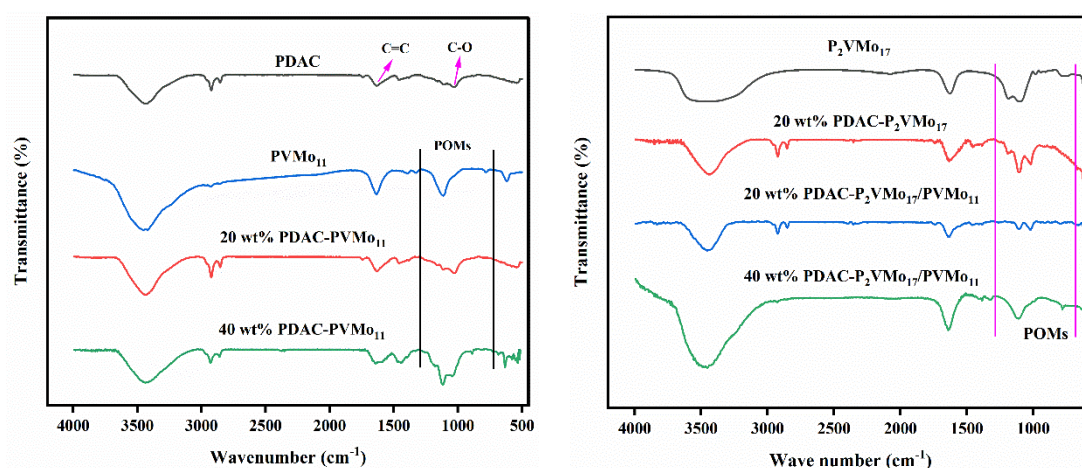


Figure 6.1: FTIR spectra of PDAC, $PVMO_{11}$, P_2VMO_{17} , and all nanocomposites.

FTIR spectra were obtained using a Bruker 4000 spectrometer (USA) to analyze the chemical composition of the materials. **Figure 6.1** shows the FTIR spectra of PDAC, P_2VMO_{17} , $PVMO_{11}$ and the composites of 20 wt% PDAC- $P_2VMO_{17}/PVMO_{11}$, 40 wt% PDAC- $P_2VMO_{17}/PVMO_{11}$, 20 wt% PDAC- $PVMO_{11}$, 40 wt% PDAC- $PVMO_{11}$, 20 wt% PDAC- P_2VMO_{17} , respectively. In all composite materials, PDAC, $PVMO_{11}$, and P_2VMO_{17} polyanions, the characteristic IR bands are well-matched with those reported in the literature (Gao et al. 2018; Vannathan et al. 2020). The prominent four-characteristic peaks of $PVMO_{11}$ and P_2VMO_{17} polyanions were exhibited in the 750-

1100 cm^{-1} range. The peaks at 1060, 965, 875, and 783 cm^{-1} correspond to the vibration of the P-O, terminal Mo=O and Mo-O-Mo, V-O bonds. The IR bands at 3400 cm^{-1} , 1642 cm^{-1} , and 1101 cm^{-1} confirm the presence of three groups of O-H, C=C, and C-O, respectively (Anagbonu et al. 2023), indicating the Keggin and Wells-Dawson polyanion intact after deposition on PDAC.

6.2 PXRD

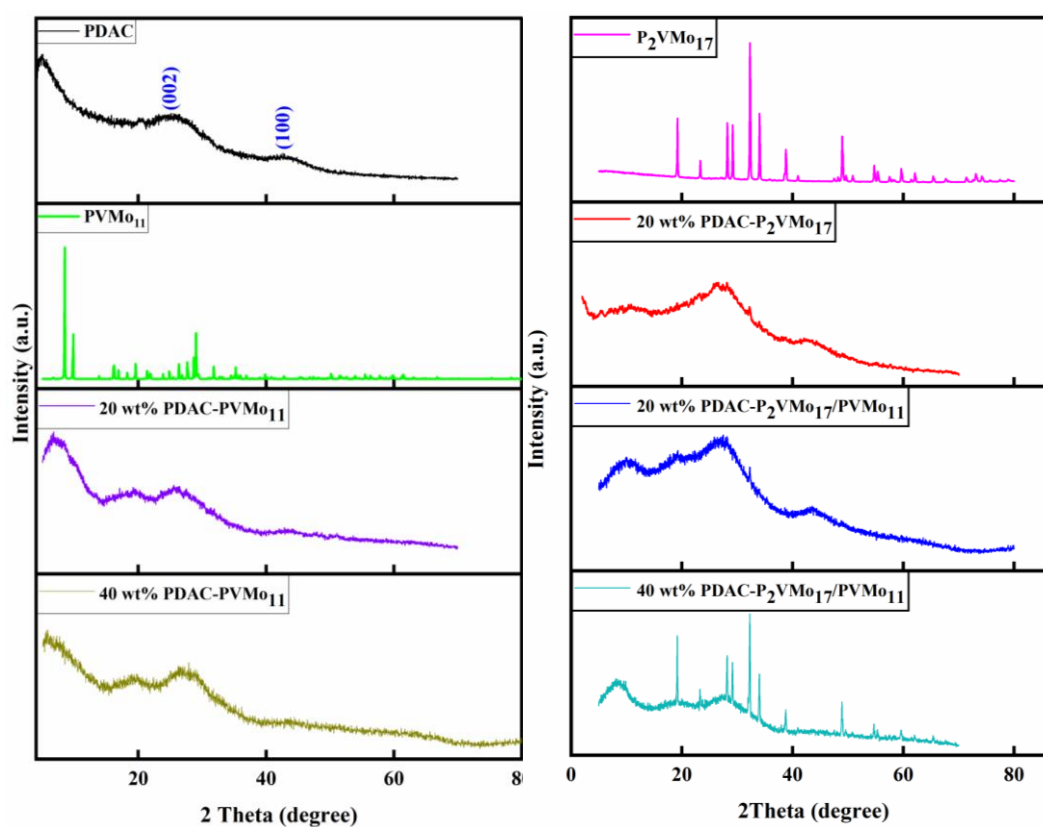
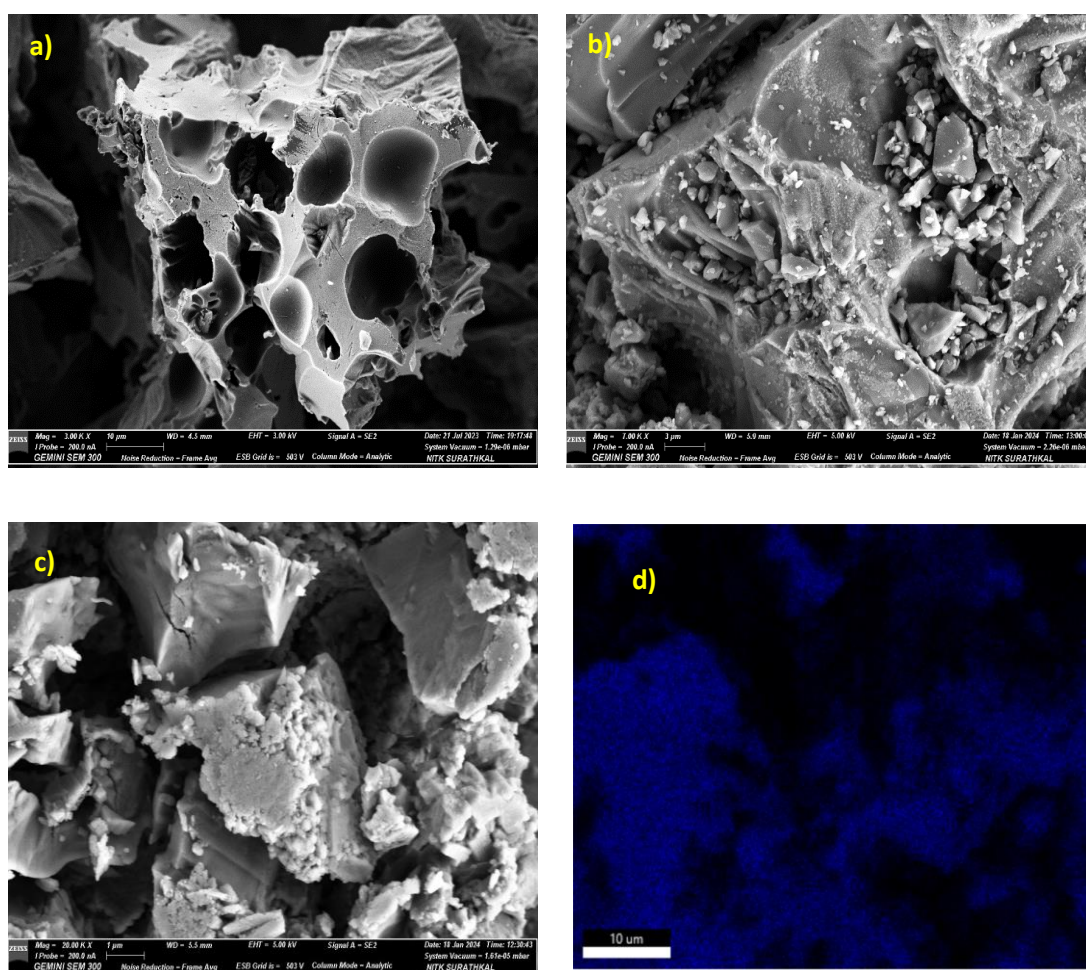


Figure 6.2: PXRD pattern of PDAC, PVMo_{11} , $\text{P}_2\text{VMo}_{17}$, 20 wt% PDAC- $\text{P}_2\text{VMo}_{17}/\text{PVMo}_{11}$, 40 wt% PDAC- $\text{P}_2\text{VMo}_{17}/\text{PVMo}_{11}$, 20 wt% PDAC- $\text{P}_2\text{VMo}_{17}$, 20 wt% PDAC- PVMo_{11} , and 40 wt% PDAC- PVMo_{11} .

Figure. 6.2 displays the powder XRD patterns of PDAC, PVMo_{11} , $\text{P}_2\text{VMo}_{17}$, and all nanocomposites. The broad pattern indicates the amorphous nature of pristine PDAC. The observed peaks around 24° and 43.8° are attributed to the graphitic carbon (002) and (100), respectively (Bharath et al. 2021). The PXRD pattern of pure $\text{P}_2\text{VMo}_{17}$ and PVMo_{11} (JCPDS card no: 00-045-0611) polyanions indicates their crystalline

nature (Babeł and Jurewicz 2008; Gao et al. 2018). The PXRD pattern of all composites represents both amorphous and crystalline nature. The broad peaks around 10° degrees, representing the presence of polyanion in the composite. The sharp peaks at approximately 19.24° , 28.2° , 29.17° , 32.32° , and 34° are due to polyanions, whereas the peaks at around 24° (002) and 43.8° (100) are attributed to the graphitic carbon present in PDAC.

6.3 FESEM



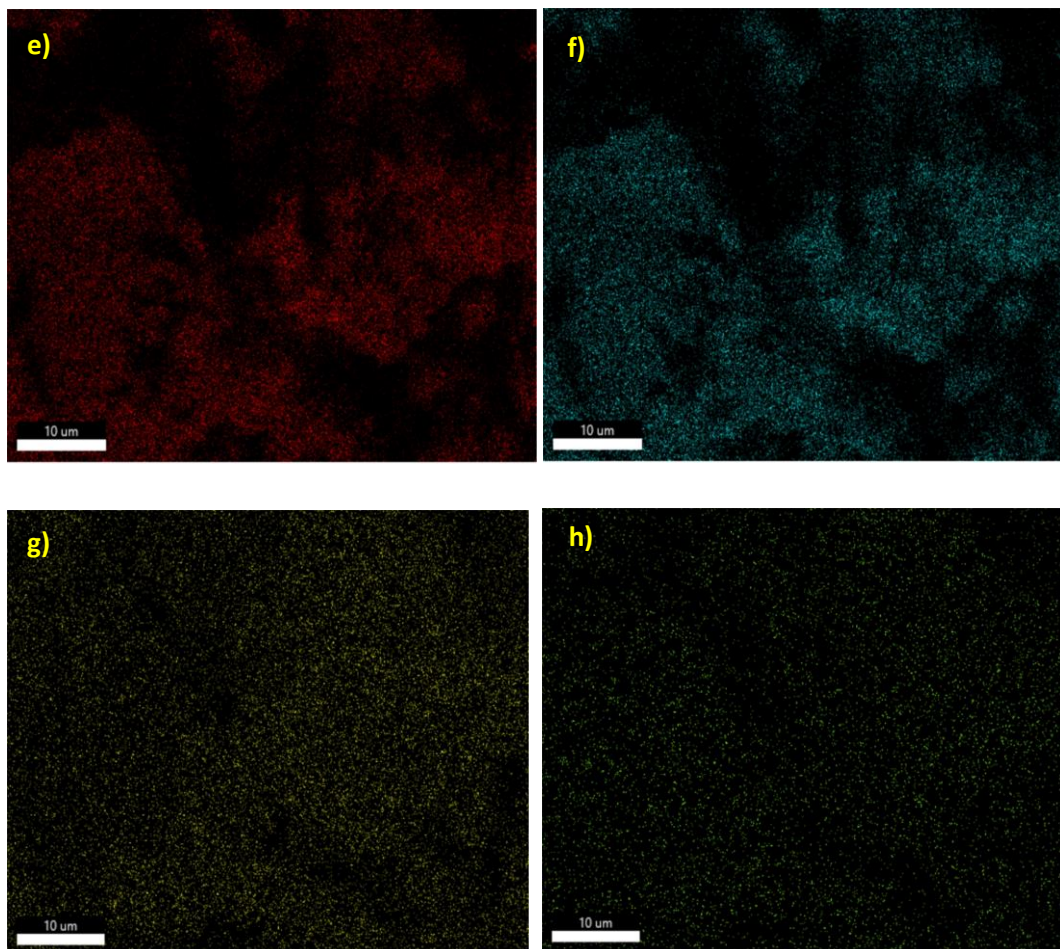


Figure 6.3:FESEM image of a) PDAC, b) 20 wt% of PDAC-P₂VMO₁₇ /PVMo₁₁, c) P₂VMO₁₇, and Elemental mapping image of 20 wt% of PDAC-P₂VMO₁₇/PVMo₁₁ d) Carbon e) Vanadium, f) Oxygen, g) Molybdenum and h) Phosphorous.

The nanocomposite's surface morphology was examined with the field emission scanning electron microscope (FESEM) equipment from Carl Zeiss Sigma in Germany. The FESEM of PDAC, P₂VMO₁₇, and 20 wt % PDAC-P₂VMO₁₇/PVMo₁₁ were illustrated in **Figure. 6.3(a-c)**. According to the figure, PDAC has a porous structure that can hold the polyanion P₂VMO₁₇ and PVMo₁₁, whereas P₂VMO₁₇ and PVMo₁₁ have a structure that resembles rock. Nevertheless, the 20 wt% PDAC-P₂VMO₁₇/PVMo₁₁ composites demonstrated that P₂VMO₁₇ and PVMo₁₁ polyanions are incorporated in PDAC's porous surfaces (**Figure. 6.3b**). The elemental analysis for 20 wt% PDAC-

P₂VMo₁₇/PVMo₁₁ nanocomposites is exhibited in **Figure 6.3(e-h)**. All components have been demonstrated to be found on the PDAC surface by the elemental analysis.

6.4 BET

The N₂ adsorption-desorption isotherm of the composites was determined with a Micromeritics physisorption analyzer (ASAP 2020, USA) at 77K. A typical Type I isotherm may be observed in the isotherms of PDAC and 20 wt% PDAC-P₂VMo₁₇/PVMo₁₁. The microporous nature of both materials is evident from the absorption of N₂ at low relative pressure. However, with the deposition of P₂VMo₁₇ and PVMo₁₁, the specific surface area, micropore area, and micropore volume of the composite all decrease, which indicates the existence of PDAC micropores. PDAC (**Figure 6.4a**) and 20 wt% PDAC-P₂VW₁₇/PVMo₁₁ (**Figure 6.4a**) have specific surface areas and micropore areas of 2416.57 m² g⁻¹ and 617.12 m² g⁻¹, respectively, 956.39 m² g⁻¹ and 323.39 m² g⁻¹ (**Table 6.1**). The BJH technique determines the average pore diameter, about 2nm (**Figure 6.4b**).

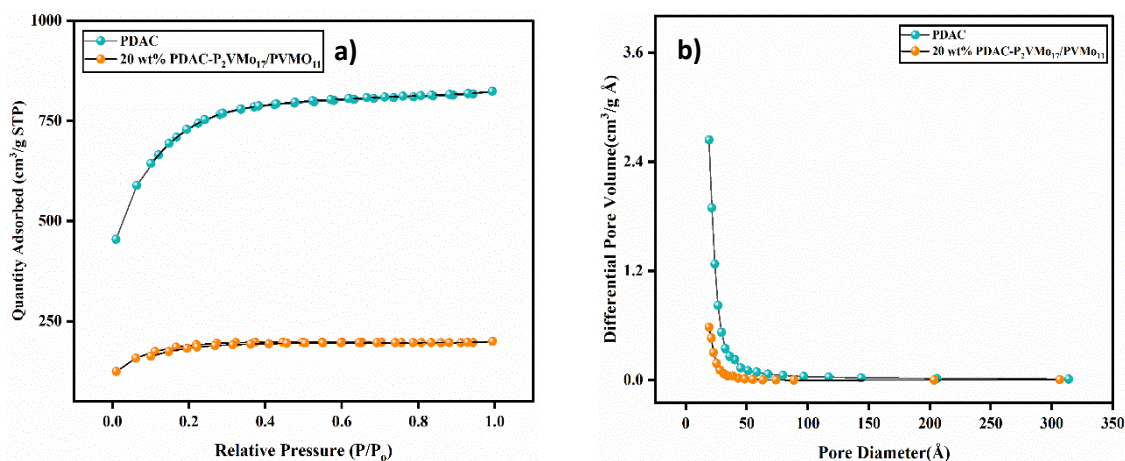


Figure 6.4: a) N₂ adsorption-desorption isotherm of PDAC and 20 wt% PDAC-P₂VMo₁₇/PVMo₁₁ and b) Pore size distribution graph of PDAC and 20 wt% PDAC-P₂VMo₁₇/PVMo₁₁.

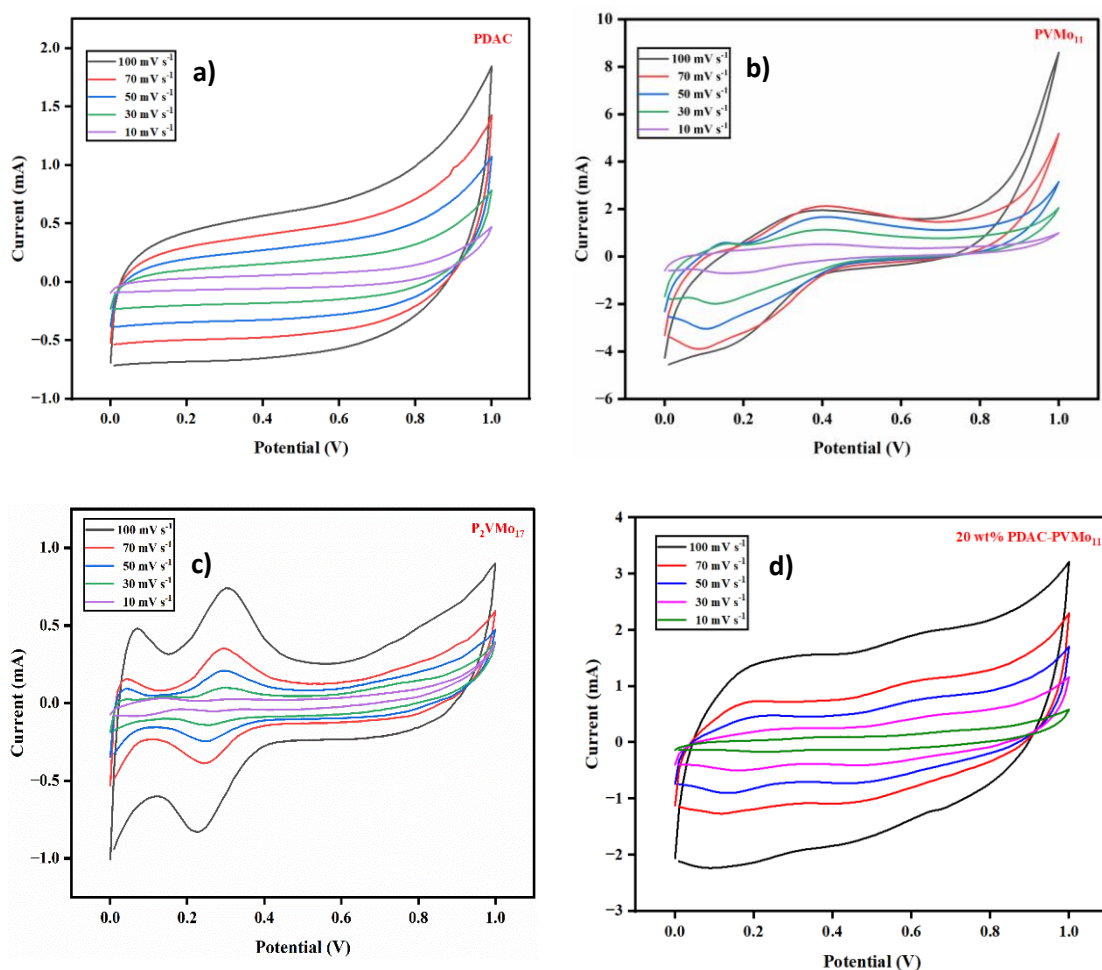
Table 6.1: Surface area and porosity of PDAC and 20 wt% PDAC-P₂VMo₁₇/PVMo₁₁.

Sample	BET Surface area (m ² g ⁻¹)	Micropore Area (m ² g ⁻¹)	Micropore Volume (cm ³ g ⁻¹)
PDAC	2416.57 m ² /g	956.39 m ² /g	0.47 cm ³ /g
20 wt%PDAC-P ₂ VMo ₁₇ /PVMo ₁₁	617.12 m ² /g	323.39 m ² /g	0.16 cm ³ /g

6.5 Electrochemical Characterizations

The cyclic voltammetry (IVIUM Technologies BV Co., The Netherlands, Model: Vertex) study was performed using two-electrode system in a 0.5M H₂SO₄ electrolyte solution of all symmetrical electrode materials. In the typical electrochemical study, cyclic voltammetry was conducted as a first step to establish the degradation mechanism, the chemical kinetics, and the determination of the specific capacitance of electrode material (Zhou and Han 2010; Elgrishi et al. 2018). In a symmetric cell (**Figure. 6.5**), cyclic voltammetry (CV) studies were performed for PDAC, P₂VMo₁₇, PVMo₁₁, and all nanocomposites at various scan rates. The CV plot showed a perfect rectangular curve for pristine PDAC (**Figure. 6.5a**), verifying the capacitive response and demonstrating a non-faradic characteristic. However, the irregular rectangular shape of P₂VMo₁₇ and PVMo₁₁ (**Figure. 6.5b&c**) indicate the existence of faradaic material oxidation and reduction peaks. The partial-rectangular CV curves were observed for all nanocomposites (**Figure. 6.5(d-h)**), suggesting that both non-faradic and faradaic charge-storage processes coexist in it. A consistent response emerged when P₂VMo₁₇ and PVMo₁₁ molecules were immobilized to the PDAC surface (20 wt% PDAC-P₂VMo₁₇/PVMo₁₁). This is because the redox peaks of P₂VMo₁₇ and PVMo₁₁ in the 20 wt% PDAC-P₂VMo₁₇/PVMo₁₁ gradually broaden the area with the same redox potential and enhance the electrochemical performance (Genovese et al. 2015; Sadakane and Steckhan 1998). The CV curve still exhibits the cathodic and

anodic peaks as the scan rate increases, indicating the electrochemical behavior of composite materials for vanadium +5 to +4 and vice versa. However, in the case of molybdenum, it moves from +6 to +5 and +5 to +6 (Maity et al. 2021). **Figure. 6.5(d-h)** depicts the electrode's voltammetry peaks in various PVMo_{11} and $\text{P}_2\text{VMo}_{17}$ combinations, suggesting the electrode functions as a hybrid material. During the CV evaluation at 30 mV s^{-1} for the 20 wt% PDAC- $\text{P}_2\text{VMo}_{17}/\text{PVMo}_{11}$ composite, observations were made indicating the presence of discrete redox peaks at 0.26V and 0.64V for oxidation, and 0.15V and 0.49V for reduction (**Figure. 6.5i**), with a significantly wider current range. These peaks show reversible redox reactions behavior at particular potentials. Notably, that PDAC-polyanions composites are formed by physisorption processes which will not change the structure of polyanions. So, the capacitive and faradic peak (Genovese et al. 2016) are clearly visible in the CV.



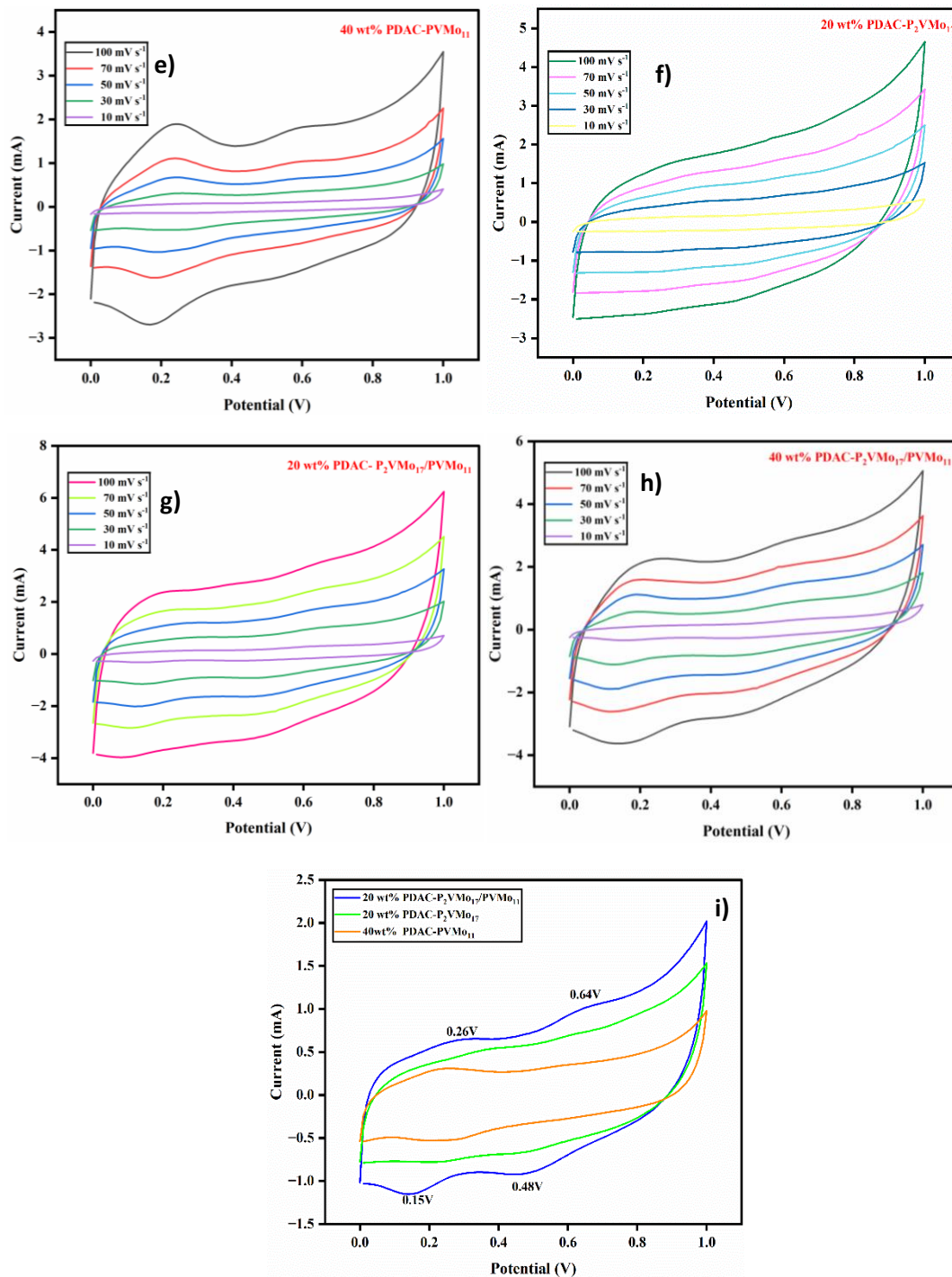
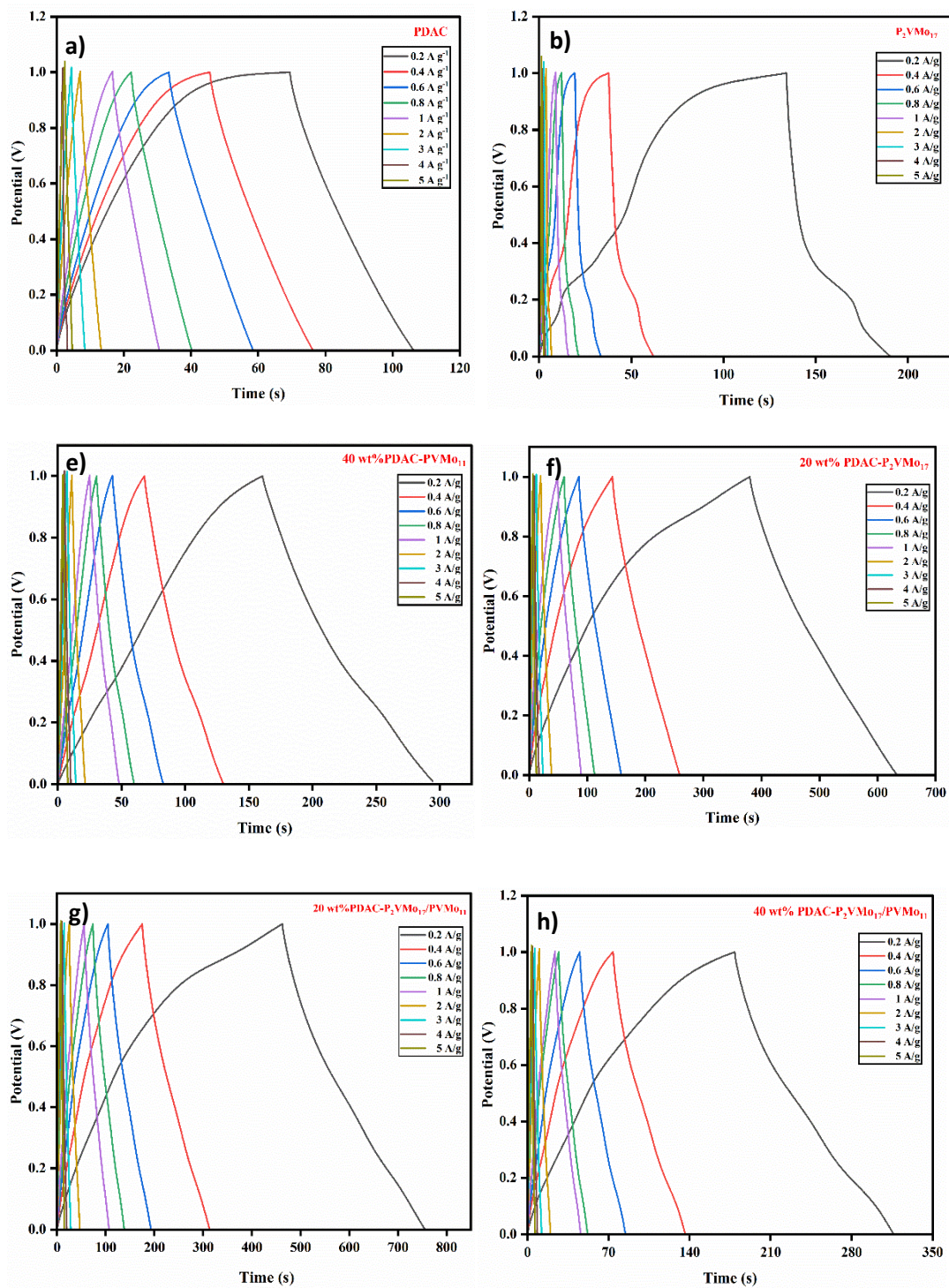


Figure 6.5: Cyclic Voltammetry graph of a) Pure PDAC, b) Pure PVMO₁₁, c) Pure P₂VMo₁₇, d) 20 wt% PDAC-PVMO₁₁, e) 40 wt% PDAC-PVMO₁₁, f) 20 wt% PDAC-P₂VMo₁₇, g) 20 wt% PDAC-P₂VMo₁₇/PVMO₁₁ h) 40 wt% PDAC-P₂VMo₁₇/PVMO₁₁

and i) comparison cyclic graph of 20 wt% PDAC-P₂VMo₁₇/PVMo₁₁, 20 wt% PDAC-P₂VMo₁₇ and 20 wt% PDAC-PVMo₁₁.



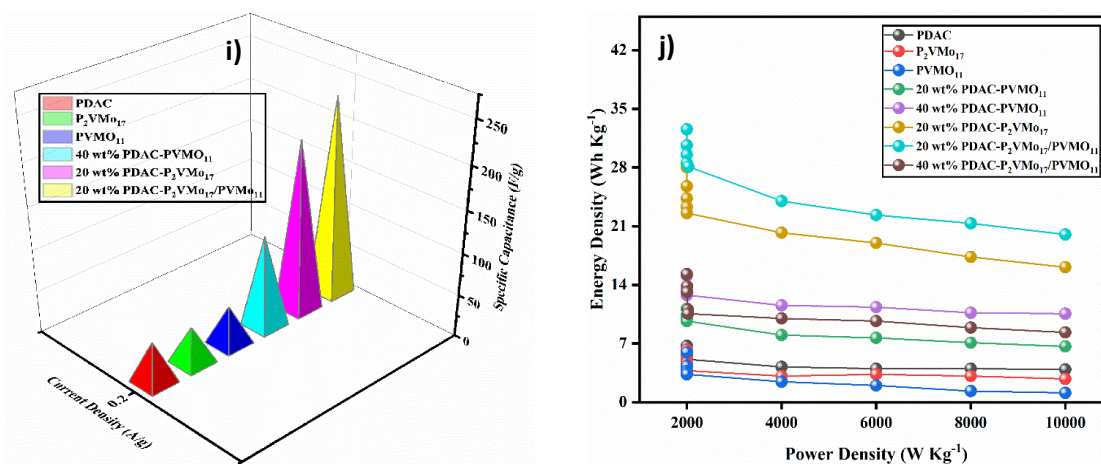


Figure 6.6: Galvanostatic charge and discharge graph of a) Pure PDAC, b) Pure P₂VMo₁₇, c) Pure PVMo₁₁, d) 20 wt% PDAC-PVMo₁₁, e) 40 wt% PDAC-PVMo₁₁, f) 20 wt% PDAC-P₂VMo₁₇, g) 20 wt% PDAC- P₂VMo₁₇/PVMo₁₁, h) 40 wt% PDAC-P₂VMo₁₇/PVMo₁₁, i) comparison graph of all nanocomposites specific capacitance versus current density at 0.2 A g⁻¹ and j) Ragone plot of all nanocomposites.

In a two-electrode cell arrangement, galvanostatic charge and discharge experiments were carried out to evaluate the electrochemical performance of all symmetric electrode cells at various current densities within a specified potential window of 0–1V in 0.5M H₂SO₄ electrolyte medium. The galvanostatic charge-discharge responses of a symmetric cell configuration were analyzed to determine the performance of 20 wt% PDAC-P₂VMo₁₇/PVMo₁₁, 40 wt% PDAC-P₂VMo₁₇/PVMo₁₁, 20 wt% PDAC-PVMo₁₁, 40 wt% PDAC-PVMo₁₁, 20 wt% PDAC-P₂VMo₁₇ nanocomposites, PDAC, P₂VMo₁₇ and PVMo₁₁ with various weight percentages, as shown in **Figure 6.6**. The pristine PDAC's charge-discharge curves are symmetrical triangular, indicating the process is non-faradic and signifying EDLC behavior (**Figure 6.6a**). Regarding the polyanions P₂VMo₁₇ and PVMo₁₁, it's observed that their charge-discharge curves deviate from the ideal triangular shape, as shown in **Figure 6.6b&c**. This variation can be associated to the presence of a redox-active component in the electrode material. This component shows an electrochemical reversibility, which undergoes a reduction process during the charging phase and an oxidation process during discharging.

Polyanion's combined effect was integrated into an equal ratio of PDAC carbon matrices. This combination was prepared at two different concentrations, 20 wt% and 40 wt%, specifically for PDAC-P₂VMo₁₇/PVMo₁₁, where the structure of the polyanions remained consistent due to the physisorption process during formation (Genovese et al. 2016). Additionally, combinations using a single polyanion were prepared at various wt% which included 20 wt% and 40 wt% of PDAC-PVMo₁₁ and 20 wt% PDAC-P₂VMo₁₇. All five nanocomposites (**Figure. 6.6(d-h)**) exhibited a slightly non-linear curve, indicating both non-faradic and faradic behaviors. This increased specific capacitance while maintaining high power and energy densities. The galvanostatic analysis of the symmetric supercapacitors was conducted according to **Equation 2.2**. The nanocomposite with 20 wt% PDAC-P₂VMo₁₇/PVMo₁₁ (**Figure. 6.6g**) demonstrated the high specific capacitance of 234.4 F g⁻¹ at a current density of 0.2 A g⁻¹. This peak in specific capacitance for the 20 wt% PDAC-P₂VMo₁₇/PVMo₁₁ is largely due to the even distribution of the polyanions P₂VMo₁₇ and PVMo₁₁ across the PDAC matrix. The energy density for symmetric cells at different wt% were calculated using **Equation 2.3**, with the 20 wt% PDAC-P₂VMo₁₇/PVMo₁₁ showing a high energy density of 32.55 Wh kg⁻¹. Furthermore, the specific power density was calculated using **Equation 2.4**, where the 20 wt% composition demonstrated a high-power density of 1999.96 W kg⁻¹. As the current density increases, the discharge time decreases due to the limited ion mobility of the electrolyte, reducing the time for ions to interact with the electrode material. The discharge time rises with decreased current density because ions develop more in the electrolyte (Bohinc et al. 2001). The 40 wt% PDAC-P₂VMo₁₇/PVMo₁₁ exhibits a specific capacitance of 109.92 F g⁻¹ with energy and power values of 15.26 Wh kg⁻¹ and 1999.0 W kg⁻¹. The 40 wt% PDAC-P₂VMo₁₇/PVMo₁₁ shows less than the 20 wt% PDAC-P₂VMo₁₇/PVMo₁₁; this could be due to the accumulation of redox-active component is higher, which leads to the easily detachable of polyanions from the surface of PDAC. The composites like 20 wt% of PDAC-PVMo₁₁, 40 wt% of PDAC-PVMo₁₁ and 20 wt% PDAC-P₂VMo₁₇ show lesser specific capacitance of 80.32 F g⁻¹, 108.64 F g⁻¹, 201.76 F g⁻¹ with lesser energy and power values of 11.15 Wh kg⁻¹, 15.08 Wh kg⁻¹, 28.02 Wh kg⁻¹ and 2000.0 W kg⁻¹, 1999.98 W kg⁻¹, 1999.0 W kg⁻¹, respectively it's because of uneven distribution and started leaching when cell starts performing compared to the 20 wt% of PDAC-PVMo₁₁. **Figure. 6.6j**

illustrates the Ragone plot, which provides insights into the specific energy and power of different compositions.

Electrochemical impedance spectroscopy was performed to evaluate the electron transfer kinetics of the redox process at the electrode-electrolyte interface. As shown in **Figure. 6.7a**, from the Nyquist plot the high-frequency region has a semicircular curve and in the low-frequency region contains a straight line (Conway and Pell 2003). The semicircle arc indicates the electron transfer process is limited, with the resistance attributed to the charge transfer resistance (R_{ct}). On the other hand, the linear part represents diffusion-limited electron transfer processes within the lower frequency range (Huang and Chen 2012, Augustyn et al. 2014). It has been shown that the arc is larger, then the resistance is higher between the electrode and electrolyte. The electrode material is also capacitive and contributes to the sharp response to lower frequencies due to its additional capacitive properties. **Table 6.2** illustrates the calculated values of charge transfer resistance for all nanocomposites, such as 20 wt% PDAC-P₂VMo₀₁₇, 20 wt% PDAC- P₂VMo₀₁₇/PVMo₀₁₁, 40 wt% PDAC- P₂VMo₀₁₇/PVMo₀₁₁, and 20 wt% PVMo₀₁₁ & 40 wt% PDAC-PVMo₀₁₁ & 40 wt% PVMo₀₁₁, respectively. R_s denotes solution resistance, R_p represents the polarized resistance, and R_{ct} is the charge transfer resistance. The R_{ct} of 20 wt% PDAC-P₂VMo₀₁₇/PVMo₀₁₁ exhibits lower resistance of 1.03(Ω) than the other electrodes with 20 wt% PDAC-P₂VMo₀₁₇ (1.76(Ω)), 40 wt% PDAC-PVMo₀₁₁ (1.83 (Ω)), 40 wt% PDAC-P₂VMo₀₁₇/PVMo₀₁₁ (2.54(Ω)) and 20 wt% PDAC-PVMo₀₁₁ (2.79(Ω)). The even distribution of P₂VMo₀₁₇ and PVMo₀₁₁ on the surface of PDAC results in more redox-active sites in the 20 wt% PDAC-P₂VMo₀₁₇/PVMo₀₁₁ compared to other nanocomposites. The 20 wt% PDAC-P₂VMo₀₁₇/PVMo₀₁₁ shows that conductivity was enhanced and its resistance was reduced. The equivalent series circuit was fitted using Zswipwim (3.21) (**Figure. 6.7b**), where R_s represents the solution resistance, C_1 & C_2 represent capacitances, R_1 & R_2 represent resistances, and W represents the Warburg impedance.

Table 6.2: Fitted data from Nyquist plots of equivalent circuit elements of 20 wt% PDAC-P₂VMo₀₁₇, 20 wt% PDAC-P₂VMo₀₁₇/PVMo₀₁₁, 40 wt% PDAC-P₂VMo₀₁₇/PVMo₀₁₁, and 20 wt% PVMo₀₁₁ & 40 wt% PDAC-PVMo₀₁₁.

Electrode Material	R_s (Ω)	R_p (Ω)	R_{ct} (Ω)
20 wt% PDAC-PVMO ₁₁	1.425	4.221	2.796
40 wt% PDAC-PVMO ₁₁	0.861	2.686	1.825
20 wt% PDAC-P ₂ VMo ₁₇	1.074	2.832	1.758
20 wt% PDAC-P ₂ VMo ₁₇ /PVMO ₁₁	1.378	2.411	1.033
40 wt% PDAC-P ₂ VMo ₁₇ /PVMO ₁₁	1.425	3.635	2.537

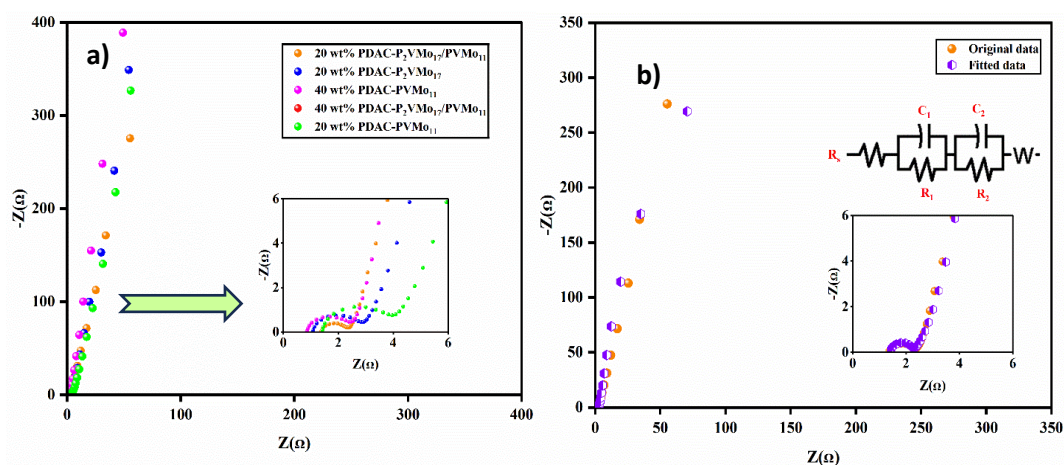
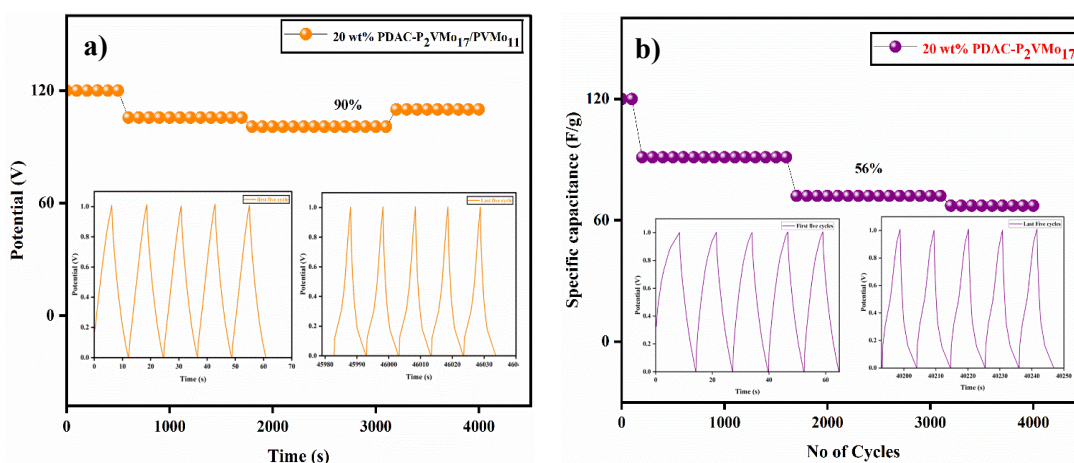


Figure 6.7: a) Nyquist plot and b) Fitted Nyquist plot require an equivalent circuit.

A supercapacitor's capacity retention could be assessed by evaluating the cell's cycle stability. A symmetrical electrode arrangement was used to determine cycle stability on the nanocomposites in various weight percentage combinations, such as 20 wt% PDAC-P₂VMo₁₇, 20 wt% PDAC-P₂VMo₁₇/PVMO₁₁, and 40 wt% PDAC-P₂VMo₁₇/PVMO₁₁ (**Figure 6.8(a-c)**). Based on this, the composite 20 wt% PDAC-P₂VMo₁₇/PVMO₁₁ exhibits a retention loss of 10% over 4000 cycles in a symmetrical electrochemical system at a 6 A g⁻¹ current. The 44% and 17% retention loss for cells

for 20 wt% PDAC-P₂VMo₁₇ and 20 wt% PDAC-PVMo₁₁ were observed after 4000 cycles. Even after being swept through a significant number of charge-discharge cycles on the PDAC surface, all three symmetric configurations remained well-loaded with P₂VMo₁₇ and PVMo₁₁ polyanions. The results above clearly demonstrate that the three nanohybrid composites have the necessary mechanical stability and durability to be employed as SC electrode materials. Since 20 wt% PDAC-P₂VMo₁₇/PVMo₁₁ showed a better electrochemical performance compared to others, we performed the practical applications. Four pairs of carbon clothes measuring 2 cm x 2 cm were coated with 20 wt% PDAC- P₂VMo₁₇/PVMo₁₁ using the above-described fabrication method (88 mg of coated active electrode material) and connected in series for lit-up LED lights. A workstation for electrochemistry was utilized to illuminate the LEDs at a potential window of 0–3 V and were alternated between red (2 V), green (3 V), and blue (3 V) (Figure. 6.8(d-f)). The LEDs continued to shine continuously for 80 seconds, around 60 seconds, and 40 seconds after the electrochemical workstation was disconnected. The device's significant power density is ensured by utilizing the 20 wt% PDAC-P₂VMo₁₇/PVMo₁₁ device's energy.



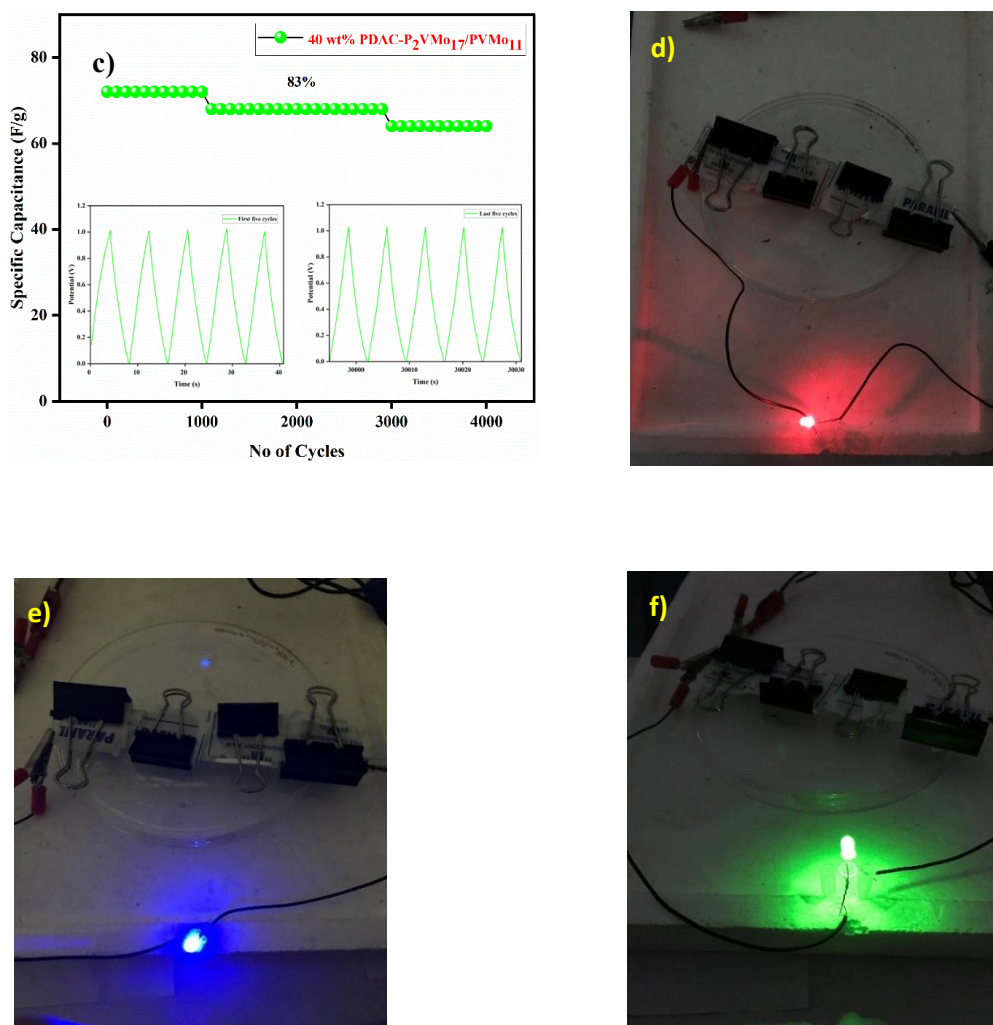


Figure 6.8: Cyclic Stability graph of a) 20 wt% PDAC- P₂VMo₁₇/ PVMo₁₁ b) 20 wt% PDAC- P₂VMo₁₇ and 40 wt% PDAC- PVMo₁₁ c) LED images of 20 wt% PDAC- P₂VMo₁₇/PVMo₁₁ d) red, e) green and f) blue.

6.6 Summary

The simple deposition method was used to deposit the polyanions of Keggin and Wells-Dawson type through physisorption, ensuring that the chemical properties of the polyanions remain unchanged. The dominant nature of the interaction between the P₂VMo₁₇/PVMo₁₁ components and the carbon surface is physical in nature. Five nanocomposites were synthesized, incorporating both types of polyanions onto PDAC surfaces at different weight percentages, 20 wt% and 40 wt% for both PDAC-P₂VMo₁₇/PVMo₁₁ and single polyanions infused onto PDAC surfaces like PDAC-PVMo₁₁ in different wt% of 20 and 40, along with 20 wt% PDAC-P₂VMo₁₇. Amongst,

the 20 wt% PDAC-P₂VMo₁₇/PVMo₁₁ composite demonstrated superior electrochemical performance, achieving a high specific capacitance of 234.4 F g⁻¹, coupled with impressive energy and power values of 32.55 Wh kg⁻¹ and 1999 W kg⁻¹, respectively. Then, the cyclic stability study was examined for 20 wt% PDAC-P₂VMo₁₇/PVMo₁₁ electrode material, which shows only 10 % of capacitance retention loss for over 4000 charge/discharge cycles. Moreover, practical uses were investigated, such as employing this substance to energize LED bulbs, highlighting its capabilities for applications in the real world.

CHAPTER 7



Summary and conclusion

7.1. Summary

In summary, a hybridization strategy by integrating phosphomolybdic acid (PMA) redox-active clusters with activated carbon derived from orange peels creates a nanohybrid electrode material through a one-pot synthesis method. Utilizing activated carbon from renewable biomass is environmentally friendly and provides inherent mechanical strength, although it may limit the specific capacitance of the material. The electrochemical performance was significantly enhanced by incorporating PMA onto the surface of orange peel-activated carbon (OPAC). This enhancement is attributed to integrating faradaic and capacitive components effectively within a single electrode structure. Electrochemical analysis of the OPAC-PMA nanohybrid revealed a notable specific capacitance of 126 F g^{-1} , accompanied by impressive specific power and energy values of 17.55 Wh kg^{-1} and 2000 W kg^{-1} , respectively, at a current density of 1 A g^{-1} . Moreover, the supercapacitor cell exhibited remarkable stability of retaining 88.23% of its capacity over 4000 cycles at a current density of 6 A g^{-1} in a $0.5 \text{ M H}_2\text{SO}_4$ electrolyte, highlighting its potential for sustainable energy storage solutions.

Subsequently, next chapter summarizes the investigation of successfully synthesized symmetric electrodes by integrating Wells-Dawson POMs onto activated carbon matrices. The hybrid electrode materials show remarkable electrochemical performances, with the 5 wt% AC- P_2W_{18} electrodes exhibiting a specific capacitance of 289 F g^{-1} . It also show impressive energy and power densities of 40 Wh kg^{-1} and 1999 W kg^{-1} , respectively. The charge storage mechanism involved efficient ion adsorption on the activated carbon surface and redox reactions facilitated by POMs that enhance the energy and power values. The hybrid electrode displayed excellent cyclic stability of 89% for 4000 cycles at 7 A g^{-1} , underlining their prolonged operational reliability for energy storage applications. The synergetic amalgamation of activated carbon and POMs within the electrode structure yielded superior electrochemical characteristics, emphasizing the promising prospects of these hybrid materials for pioneering supercapacitor technologies.

The next chapter demonstrates the overview of developing high-performance hybrid supercapacitors using vanadium-substituted Wells-Dawson POM (P_2VW_{17}) on lignin-derived activated carbon (LDAC) in different wt% of 15, 20, and 30, respectively. All three nanocomposites were fabricated to investigate their mechanical and electrochemical properties and use them as supercapacitor cells. Inclusion of pseudo-material like P_2VW_{17} on the surface of biomass-derived activated carbon, particularly from Lignin, highlighted its mechanical stability, cost-effectiveness, and eco-friendliness. LDAC showcases a porous nature ideally suited to accommodate the P_2VW_{17} polyanions, significantly enriching its properties. Among the three symmetric cells, 20 wt% LDAC- P_2VW_{17} exhibits an excellent specific capacitance of 216.48 F g^{-1} at 0.6 A g^{-1} current density. Moreover, it exhibits a high energy density of 30.06 Wh kg^{-1} and a power density of $1999.99 \text{ W kg}^{-1}$. The cycle stability study demonstrated that the 20 wt% LDAC- P_2VW_{17} electrode material retained 94.4% specific capacitance over 4000 charge-discharge cycles. However, the realistic application of the fabricated 20 wt% LDAC- P_2VW_{17} cell was performed in a series of LEDs, which took 30 seconds to charge and 30 seconds to discharge. A piezoelectric buzzer sounded for 140s.

The subsequent chapter presents a detailed overview of the innovative properties of a novel hybrid supercapacitor electrode material. This material is created by combining POMs with activated carbon derived from pomegranate peel (PDAC). Specifically, vanadium-substituted phosphomolybdates of the Wells-Dawson type (P_2VMO_{17}) and the Keggin type ($PVMO_{11}$) polyanions were integrated onto the surface of PDAC. The composite formation occurs through physisorption, ensuring that the chemical properties of the polyanions remain unchanged. This indicates that the interaction between the carbon surface and the $P_2VMO_{17}/PVMO_{11}$ components is predominantly physical. Five nanocomposites were synthesized, incorporating both types of polyanions onto PDAC surfaces at different weight percentages, 20 wt% and 40 wt% for both PDAC- $P_2VMO_{17}/PVMO_{11}$ and single polyanions infused onto PDAC surfaces like PDAC- $PVMO_{11}$ in different wt% of 20 and 40, along with 20 wt% PDAC- P_2VMO_{17} . Among these, the 20 wt% PDAC- $P_2VMO_{17}/PVMO_{11}$ composite demonstrated superior electrochemical performance, achieving a high specific capacitance of 234.4 F g^{-1} , coupled with impressive energy and power values of 32.55 Wh kg^{-1} and 1999 W

kg^{-1} , respectively. Furthermore, practical applications were explored, including using this material to power LED bulbs, showcasing its potential for real-world applications.

7.2 Conclusions

- The formation of orange peel-derived activated carbon (OPAC), the host material for infusing PMA, provided novel electrode material for SC applications. It is observed that OPAC-PMA demonstrates remarkable specific capacitance, energy density, power density, and stability due to the fast multi-electron transfer redox property of PMA in OPAC.
- A simple deposition was used to inclusion of phosphotungstate (P_2W_{18}) in activated carbon. Three different nanocomposites were synthesized by varying the wt % of P_2W_{18} , like 5 wt%, 10 wt%, and 15 wt% of AC- P_2W_{18} . Among these 5 wt% shows the highest specific capacitance of 289 F g^{-1} with an energy density of 40 Wh kg^{-1} .
- Lignin-derived activated carbon is a highly preferred material due to its excellent mechanical stability, which makes it a suitable host material for POMs. Wells- Dawson-type vanadium-substituted POMs (P_2VW_{17}) were deposited on the surface of LDAC by using an in-situ deposition method. This enhances the material's specific capacitance, energy, and power density. The effectiveness of this material was confirmed by testing it in realistic applications.
- Unique properties of electrochemical energy behavior were studied by mixing the Wells-Dawson ($\text{P}_2\text{VMo}_{17}$) and Keggin (PVMo_{11}) type polyanion in pomegranate peel-derived activated carbon (PDAC) through physisorption. The physical interaction between the carbon surface and the polyanions suggested that the structures of the polyanions remained intact. The nanohybrid materials thus produced were precisely characterized using various analytical techniques.

7.3 Scope for Future Work

- ❖ The ternary composites can be synthesized using multiple transition metal substituted polyanion structures in biomass-derived activated carbon with conducting polymer, which is not included in the thesis.
- ❖ Investigating the synergy between the high porosity of biomass-derived activated carbon and Anderson-type POMs for enhancing hybrid electrode materials.
- ❖ Developing a multifaceted approach to waste management by repurposing waste cotton materials, contributing to a circular economy.

References

- Afif, A., Rahman, S. M., Tasfiah Azad, A., Zaini, J., Islan, M. A., and Azad, A. K. (2019). "Advanced materials and technologies for hybrid supercapacitors for energy storage – A review." *Journal of Energy Storage*, 25, 100852.
- Ammam, M. (2013). "Polyoxometalates: formation, structures, principal properties, main deposition methods and application in sensing." *J. Mater. Chem. A*, 1(21), 6291.
- Anagbonu, P., Ghali, M., and Allam, A. (2023). "Low-temperature green synthesis of few-layered graphene sheets from pomegranate peels for supercapacitor applications." *Sci Rep*, 13(1), 15627.
- Anderson, J. S. (1937). "Constitution of the Poly-acids." *Nature*, 140(3550), 850–850.
- Arefmanesh, M., Vuong, T. V., Mobley, J. K., Alinejad, M., Master, E. R., and Nejad, M. (2020). "Bromide-Based Ionic Liquid Treatment of Hardwood Organosolv Lignin Yielded a More Reactive Biobased Polyol." *Ind. Eng. Chem. Res.*, 59(42), 18740–18747.
- Augustyn, V., Simon, P., and Dunn, B. (2014). "Pseudocapacitive oxide materials for high-rate electrochemical energy storage." *Energy Environ. Sci.*, 7(5), 1597.
- Ashok Kumar, N., and Baek, J.-B. (2014). "Electrochemical supercapacitors from conducting polyaniline–graphene platforms." *Chem. Commun.*, 50(48), 6298.
- Awitdrus, Siregar, G. M. G., Agustino, Saktioto, Iwantono, Syahputra, R. F., and Farma, R. (2021). "KOH Activation with Microwave Irradiation and its Effect on the Physical Properties of Orange Peel Activated Carbon." *J. Phys.: Conf. Ser.*, 2049(1), 012025.
- Babeł, K., and Jurewicz, K. (2008). "KOH activated lignin based nanostructured carbon exhibiting high hydrogen electrosorption." *Carbon*, 46(14), 1948–1956.
- Bai, Z., Gao, N., Xu, H., Wang, X., Tan, L., Pang, H., and Ma, H. (2020). "Construction of an ultra-sensitive electrochemical sensor based on Polyoxometalates decorated with CNTs and AuCo nanoparticles for the voltammetric simultaneous determination of dopamine and uric acid." *Microchim Acta*, 187(8), 483.

- Barzegar, F., Momodu, D. Y., Fashedemi, O. O., Bello, A., Dangbegnon, J. K., and Manyala, N. (2015). “Investigation of different aqueous electrolytes on the electrochemical performance of activated carbon-based supercapacitors.” *RSC Adv.*, 5(130), 107482–107487.
- Bedia, J., Peñas-Garzón, M., Gómez-Avilés, A., Rodríguez, J., and Belver, C. (2018). “A Review on the Synthesis and Characterization of Biomass-Derived Carbons for Adsorption of Emerging Contaminants from Water.” *C*, 4(4), 63.
- Bharath, G., Hai, A., Rambabu, K., Ahmed, F., Haidyrah, A. S., Ahmad, N., Hasan, S. W., and Banat, F. (2021). “Hybrid capacitive deionization of NaCl and toxic heavy metal ions using faradic electrodes of silver nanospheres decorated pomegranate peel-derived activated carbon.” *Environmental Research*, 197, 111110.
- Bohinc, K., Kralj-Iglič, V., and Iglič, A. (2001). “Thickness of electrical double layer. Effect of ion size.” *Electrochimica Acta*, 46(19), 3033–3040.
- Briand, L. E., Baronetti, G. T., and Thomas, H. J. (2003). “The state of the art on Wells–Dawson heteropoly-compounds.” *Applied Catalysis A: General*, 256(1–2), 37–50.
- Bazan, A., Nowicki, P., Pórolniczak, P., and Pietrzak, R. (2016). “Thermal analysis of activated carbon obtained from residue after supercritical extraction of hops.” *J Therm Anal Calorim*, 125(3), 1199–1204.
- Berzelius, J. J. (1826). “Beitrag zur näheren Kenntniss des Molybdäns.” *Annalen der Physik*, 82(4), 369–392.
- Bagheri, S., Muhd Julkapli, N., and Bee Abd Hamid, S. (2015). “Functionalized Activated Carbon Derived from Biomass for Photocatalysis Applications Perspective.” *International Journal of Photoenergy*, 2015, 1–30.
- Bian, W., Zhu, S., Qi, M., Xiao, L., Liu, Z., and Zhan, J. (2017). “Electrostatic-driven solid phase microextraction coupled with surface enhanced Raman spectroscopy for rapid analysis of pentachlorophenol.” *Anal. Methods*, 9(3), 459–464.
- Babu, B., Simon, P., and Balducci, A. (2020). “Fast Charging Materials for High Power Applications.” *Advanced Energy Materials*, 10(29), 2001128.

- Chen, K., and Xue, D. (2016). “Colloidal supercapacitor electrode materials.” *Materials Research Bulletin*, 83, 201–206.
- Conway, B. E. (1991). “Transition from ‘Supercapacitor’ to ‘Battery’ Behavior in Electrochemical Energy Storage.” *J. Electrochem. Soc.*, 138(6), 1539–1548.
- Conway, B. E., and Pell, W. G. (2003). “Double-layer and pseudocapacitance types of electrochemical capacitors and their applications to the development of hybrid devices.” *Journal of Solid State Electrochemistry*, 7(9), 637–644.
- “Crystallite growth in graphitizing and non-graphitizing carbons.” (1951). *Proc. R. Soc. Lond. A*, 209(1097), 196–218.
- Choi, D., Blomgren, G. E., and Kumta, P. N. (2006). “Fast and Reversible Surface Redox Reaction in Nanocrystalline Vanadium Nitride Supercapacitors.” *Advanced Materials*, 18(9), 1178–1182.
- Davies, A., and Yu, A. (2011). “Material advancements in supercapacitors: From activated carbon to carbon nanotube and graphene.” *Can J Chem Eng*, 89(6), 1342–1357.
- Dawson, B. (1953). “The structure of the 9(18)-heteropoly anion in potassium 9(18)-tungstophosphate, $K_6(P_2W_{18}O_{62}) \cdot 14H_2O$.” *Acta Cryst*, 6(2), 113–126.
- Dawson, E. A., Parkes, G. M. B., Barnes, P. A., and Chinn, M. J. (2003). “An investigation of the porosity of carbons prepared by constant rate activation in air.” *Carbon*, 41(3), 571–578.
- Devillers, N., Jemei, S., Péra, M.-C., Bienaimé, D., and Gustin, F. (2014). “Review of characterization methods for supercapacitor modelling.” *Journal of Power Sources*, 246, 596–608.
- Dodds, P. E., Staffell, I., Hawkes, A. D., Li, F., Grünewald, P., McDowall, W., and Ekins, P. (2015). “Hydrogen and fuel cell technologies for heating: A review.” *International Journal of Hydrogen Energy*, 40(5), 2065–2083.
- Du, D.-Y., Yan, L.-K., Su, Z.-M., Li, S.-L., Lan, Y.-Q., and Wang, E.-B. (2013). “Chiral Polyoxometalates-based materials: From design syntheses to functional applications.” *Coordination Chemistry Reviews*, 257(3–4), 702–717.

- Dubey, P., Shrivastav, V., Maheshwari, P. H., and Sundriyal, S. (2020). "Recent advances in biomass derived activated carbon electrodes for hybrid electrochemical capacitor applications: Challenges and opportunities." *Carbon*, 170, 1–29.
- Elgrishi, N., Rountree, K. J., McCarthy, B. D., Rountree, E. S., Eisenhart, T. T., and Dempsey, J. L. (2018). "A Practical Beginner's Guide to Cyclic Voltammetry." *J. Chem. Educ.*, 95(2), 197–206.
- Elmouwahidi, A., Bailón-García, E., Pérez-Cadenas, A. F., Maldonado-Hódar, F. J., and Carrasco-Marín, F. (2017). "Activated carbons from KOH and H₃PO₄ -activation of olive residues and its application as supercapacitor electrodes." *Electrochimica Acta*, 229, 219–228.
- Evans, H. T., Gatehouse, B. M., and Leverett, P. (1975). "Crystal structure of the heptamolybdate(VI)(paramolybdate) ion, [Mo₇O₂₄]⁶⁻, in the ammonium and potassium tetrahydrate salts." *J. Chem. Soc., Dalton Trans.*, (6), 505–514.
- Endo, M., Maeda, T., Takeda, T., Kim, Y. J., Koshiba, K., Hara, H., and Dresselhaus, M. S. (2001). "Capacitance and Pore-Size Distribution in Aqueous and Nonaqueous Electrolytes Using Various Activated Carbon Electrodes." *J. Electrochem. Soc.*, 148(8), A910.
- Gao, Y., Lv, Z., Gao, R., Zhang, G., Zheng, Y., and Zhao, J. (2018). "Oxidative desulfurization process of model fuel under molecular oxygen by Polyoxometalates loaded in hybrid material CNTs@MOF-199 as catalyst." *Journal of Hazardous Materials*, 359, 258–265.
- Gao, Y., Yue, Q., Gao, B., and Li, A. (2020). "Insight into activated carbon from different kinds of chemical activating agents: A review." *Science of The Total Environment*, 746, 141094.
- Genovese, M., Foong, Y. W., and Lian, K. (2015). "Designing Polyoxometalates based Layer-by-Layer Thin Films on Carbon Nanomaterials for Pseudocapacitive Electrodes." *J. Electrochem. Soc.*, 162(5), A5041–A5046.
- Genovese, M., Foong, Y. W., and Lian, K. (2016). "The unique properties of aqueous Polyoxometalates (POM) mixtures and their role in the design of molecular coatings for electrochemical energy storage." *Electrochimica Acta*, 199, 261–269.

- Genovese, M., and Lian, K. (2017). "Polyoxometalates." *Metal Oxides in Supercapacitors*, Elsevier, 133–164.
- González, A., Goikolea, E., Barrena, J. A., and Mysyk, R. (2016). "Review on supercapacitors: Technologies and materials." *Renewable and Sustainable Energy Reviews*, 58, 1189–1206.
- Gumerova, N. I., and Rompel, A. (2018). "Synthesis, structures and applications of electron-rich Polyoxometalates." *Nat Rev Chem*, 2(2), 0112.
- Han, F., Jing, W., Wu, Q., Tian, B., Lin, Q., Wang, C., Zhao, L., Liu, J., Sun, Y., and Jiang, Z. (2022). "Nitrogen-doped graphene fiber electrodes with optimal micro-/meso-/macro-porosity ratios for high-performance flexible supercapacitors." *Journal of Power Sources*, 520, 230866.
- Harmalkar, S. P., Leparulo, M. A., and Pope, M. T. (1983). "Mixed-valence chemistry of adjacent vanadium centers in heteropolytungstate anions. I. Synthesis and electronic structures of mono-, di-, and trisubstituted derivatives of .alpha.-octadecatungstodiphosphate(6-) ion (.alpha.-[P₂W₁₈O₆₂]⁶⁻)." *J. Am. Chem. Soc.*, 105(13), 4286–4292.
- Harris, P. J. F., Liu, Z., and Suenaga, K. (2008). "Imaging the atomic structure of activated carbon." *J. Phys.: Condens. Matter*, 20(36), 362201.
- Heidarinejad, Z., Dehghani, M. H., Heidari, M., Javedan, G., Ali, I., and Sillanpää, M. (2020). "Methods for preparation and activation of activated carbon: a review." *Environ Chem Lett*, 18(2), 393–415.
- Hill, C. L. (1998). "Introduction: PolyoxometalatesMulticomponent Molecular Vehicles To Probe Fundamental Issues and Practical Problems." *Chem. Rev.*, 98(1), 1–2.
- Hossain, E., Faruque, H., Sunny, Md., Mohammad, N., and Nawar, N. (2020). "A Comprehensive Review on Energy Storage Systems: Types, Comparison, Current Scenario, Applications, Barriers, and Potential Solutions, Policies, and Future Prospects." *Energies*, 13(14), 3651.

- Huang, F., and Chen, D. (2012). “Towards the upper bound of electrochemical performance of ACNT@polyaniline arrays as supercapacitors.” *Energy Environ. Sci.*, 5(2), 5833–5841.
- Hu, B., Wang, K., Wu, L., Yu, S., Antonietti, M., and Titirici, M. (2010). “Engineering Carbon Materials from the Hydrothermal Carbonization Process of Biomass.” *Advanced Materials*, 22(7), 813–828.
- He, H., Liu, Y., Shearing, P. R., He, G., and Brett, D. J. L. (2022). “Mesoporous Carbon for Supercapacitors.” *Nanostructured Materials for Supercapacitors*, Advances in Material Research and Technology, S. Thomas, A. B. Gueye, and R. K. Gupta, eds., Cham: Springer International Publishing, 147–163.
- Jin, H., Li, J., Yuan, Y., Wang, J., Lu, J., and Wang, S. (2018). “Recent Progress in Biomass-Derived Electrode Materials for High Volumetric Performance Supercapacitors.” *Adv. Energy Mater.*, 8(23), 1801007.
- Ji, Y., Huang, L., Hu, J., Streb, C., and Song, Y.-F. (2015). “Polyoxometalates-functionalized nanocarbon materials for energy conversion, energy storage and sensor systems.” *Energy Environ. Sci.*, 8(3), 776–789.
- Jia, X., Fan, D., Tang, P., Hao, J., Ma, L., and Liu, T. (2006). “‘Second Organized Structures’ of Nanoscale Inorganic Polyoxomolybdate Compounds.” *Acta Physico-Chimica Sinica*, 22(10), 1300–1304.
- Jarrah, A., and Farhadi, S. (2018). “ $K_6P_2W_{18}O_{62}$ encapsulated into magnetic Fe_3O_4 /MIL-101 (Cr) metal–organic framework: a novel magnetically recoverable nanoporous adsorbent for ultrafast treatment of aqueous organic pollutants solutions.” *RSC Adv.*, 8(66), 37976–37992.
- Iordache, I., Gheorghe, A. V., and Iordache, M. (2013). “Towards a hydrogen economy in Romania: Statistics, technical and scientific general aspects.” *International Journal of Hydrogen Energy*, 38(28), 12231–12240.
- K, D., and Singh, A. K. (2023). “Highly performed electrochemical activities of hybrid supercapacitors based on CeO_2 - Sm_2O_3 nanocomposites.” *Electrochimica Acta*, 466, 143008.

- Kamiya, Y., Sadakane, M., and Ueda, W. (2013). "Heteropoly Compounds." *Comprehensive Inorganic Chemistry II*, Elsevier, 185–204.
- Kasperkiewicz, J., Kovacich, J. A., and Lichtman, D. (1983). "XPS studies of vanadium and vanadium oxides." *Journal of Electron Spectroscopy and Related Phenomena*, 32(2), 123–132.
- Keggin, J. F. (1933). "Structure of the Molecule of 12-Phosphotungstic Acid." *Nature*, 131(3321), 908–909.
- Khalilpour, H., Shafiee, P., Darbandi, A., Yusuf, M., Mahmoudi, S., Moazzami Goudarzi, Z., and Mirzamohammadi, S. (2021). "Application of Polyoxometalates-based composites for sensor systems: A review." *jcc*, 3(7), 129–139.
- Kötz, R., and Carlen, M. (2000). "Principles and applications of electrochemical capacitors." *Electrochimica Acta*, 45(15–16), 2483–2498.
- Kozhevnikov, I. (2002). "Catalysis by Polyoxometalates." (*No Title*).
- Kwon, S. J., Kim, T., Jung, B. M., Lee, S. B., and Choi, U. H. (2018). "Multifunctional Epoxy-Based Solid Polymer Electrolytes for Solid-State Supercapacitors." *ACS Appl. Mater. Interfaces*, 10(41), 35108–35117.
- Kaipannan, S., and Marappan, S. (2019). "Fabrication of 9.6 V High-performance Asymmetric Supercapacitors Stack Based on Nickel Hexacyanoferrate-derived Ni(OH)₂ Nanosheets and Bio-derived Activated Carbon." *Sci Rep*, 9(1), 1104.
- Kozhevnikov, I. V. (2003). "Heterogeneous Catalysis by Heteropoly Compounds." *Polyoxometalates Molecular Science*, J. J. Borrás-Almenar, E. Coronado, A. Müller, and M. Pope, eds.
- Kim, H.-S., Cook, J. B., Lin, H., Ko, J. S., Tolbert, S. H., Ozolins, V., and Dunn, B. (2017). "Oxygen vacancies enhance pseudocapacitive charge storage properties of MoO_{3-x}." *Nature Mater*, 16(4), 454–460.
- Laforgue, A., Simon, P., Fauvarque, J. F., Mastragostino, M., Soavi, F., Sarrau, J. F., Lailier, P., Conte, M., Rossi, E., and Saguatti, S. (2003). "Activated Carbon/Conducting Polymer Hybrid Supercapacitors." *J. Electrochem. Soc.*, 150(5), A645.

- Lei, Z., Christov, N., and Zhao, X. S. (2011). “Intercalation of mesoporous carbon spheres between reduced graphene oxide sheets for preparing high-rate supercapacitor electrodes.” *Energy Environ. Sci.*, 4(5), 1866.
- Lim, E., Jo, C., Kim, M. S., Kim, M.-H., Chun, J., Kim, H., Park, J., Roh, K. C., Kang, K., Yoon, S., and Lee, J. (2016). “High-Performance Sodium-Ion Hybrid Supercapacitor Based on Nb₂O₅@Carbon Core-Shell Nanoparticles and Reduced Graphene Oxide Nanocomposites.” *Adv. Funct. Mater.*, 26(21), 3711–3719.
- Liu, H., Liu, X., Wang, S., Liu, H.-K., and Li, L. (2020). “Transition metal based battery-type electrodes in hybrid supercapacitors: A review.” *Energy Storage Materials*, 28, 122–145.
- Liu, S., Wei, W., Wu, S., and Zhang, F. (2020). “Preparation of hierarchical porous activated carbons from different industrial lignin for highly efficient adsorption performance.” *J Porous Mater*, 27(5), 1523–1533.
- Low, W. H., Siong, C. W., Chia, C. H., Lim, S. S., and Khiew, P. S. (2019). “A facile synthesis of graphene/Co₃V₂O₈ nanocomposites and their enhanced charge storage performance in electrochemical capacitors.” *Journal of Science: Advanced Materials and Devices*, 4(4), 515–523.
- Luo, L., Lan, Y., Zhang, Q., Deng, J., Luo, L., Zeng, Q., Gao, H., and Zhao, W. (2022). “A review on biomass-derived activated carbon as electrode materials for energy storage supercapacitors.” *Journal of Energy Storage*, 55, 105839.
- Luo, X., Wang, J., Dooner, M., and Clarke, J. (2015). “Overview of current development in electrical energy storage technologies and the application potential in power system operation.” *Applied Energy*, 137, 511–536.
- Liu, J., Wang, J., Xu, C., Jiang, H., Li, C., Zhang, L., Lin, J., and Shen, Z. X. (2018). “Advanced Energy Storage Devices: Basic Principles, Analytical Methods, and Rational Materials Design.” *Adv. Sci.*, 5(1), 1700322.
- M. Malarvizhi, M. M., S. Meyvel, S. M., S.Karthikeyan, S. K., D. Thillaikkarasi, D. T., M. Dakshana, M. D., and G. Ravikumar, G. R. (2019). “Biomass derived Nanoporous Carbon Based Electrodes for High Performance Symmetric Supercapacitor.” *J. Environ. Nanotechnol.*, 8(4), 33–37.

- Maity, S., Bm, N., Kella, T., Shee, D., Das, P. P., and Mal, S. S. (2021). “Activated carbon- supported Vanado-nickelate (IV) based hybrid materials for energy application.” *Journal of Energy Storage*, 40, 102727.
- Mbomekalle, I., Keita, B., Lu, Y. W., Nadjo, L., Contant, R., Belai, N., and Pope, M. T. (2004). “Synthesis and Electrochemistry of the Monolacunary Dawson-Type Tungstoarsenate $[H_4 AsW_{17} O_{61}]^{11-}$ and Some First-Row Transition-Metal Ion Derivatives.” *Eur J Inorg Chem*, 2004(20), 4132–4139.
- Momodou, D., Bello, A., Oyedotun, K., Ochai-Ejeh, F., Dangbegnon, J., Madito, M., and Manyala, N. (2017). “Enhanced electrochemical response of activated carbon nanostructures from tree-bark biomass waste in polymer-gel active electrolytes.” *RSC Adv.*, 7(59), 37286–37295.
- Muzaffar, A., Ahamed, M. B., Deshmukh, K., and Thirumalai, J. (2019). “A review on recent advances in hybrid supercapacitors: Design, fabrication and applications.” *Renewable and Sustainable Energy Reviews*, 101, 123–145.
- Muduli, S., Naresh, V., and Martha, S. K. (2020). “Boron, Nitrogen-Doped Porous Carbon Derived from Biowaste Orange Peel as Negative Electrode Material for Lead-Carbon Hybrid Ultracapacitors.” *J. Electrochem. Soc.*, 167(9), 090512.
- Mousavi, M. F., Hashemi, M., Rahmanifar, M. S., and Noori, A. (2017). “Synergistic effect between redox additive electrolyte and PANI-rGO nanocomposite electrode for high energy and high power supercapacitor.” *Electrochimica Acta*, 228, 290–298.
- Markoulidis, Todorova, Grilli, Lekakou, and Trapalis. (2019). “Composite Electrodes of Activated Carbon and Multiwall Carbon Nanotubes Decorated with Silver Nanoparticles for High Power Energy Storage.” *J. Compos. Sci.*, 3(4), 97.
- Murugan, A. V., Kwon, C.-W., Campet, G., and Kale, B. B. (2003). “Synthesis and Characterization of Novel Organo-Inorganic Hybrid Material of Poly(3,4-Ethylene Dioxythiophene) and Phosphomolybdate Anion.” *Active and Passive Electronic Components*, 26(2), 81–86.
- Müller, A., Krickemeyer, E., Meyer, J., Bögge, H., Peters, F., Plass, W., Diemann, E., Dillinger, S., Nonnenbruch, F., Randerath, M., and Menke, C. (1995). “[$Mo_{154} (NO)_{14} O_{420} (OH)_{28} (H_2 O)_{70}]^{(25 \pm 5)-}$: A Water-Soluble Big Wheel with More than 700

Atoms and a Relative Molecular Mass of About 24000.” *Angew. Chem. Int. Ed. Engl.*, 34(19), 2122–2124.

Miolati, A., & Pizzighelli, R. (1908). Zur Kenntnis der komplexen Säuren I. 1. Über die Leitfähigkeit von molybdänsäurehaltigen Gemischen. *Journal für Praktische Chemie*, 77(1), 417–456.

Miller, J. R., and Burke, A. (2008). “Electrochemical Capacitors: Challenges and Opportunities for Real-World Applications.” *Electrochem. Soc. Interface*, 17(1), 53–57.

Midilli, A., Ay, M., Dincer, I., and Rosen, M. A. (2005). “On hydrogen and hydrogen energy strategies.” *Renewable and Sustainable Energy Reviews*, 9(3), 255–271.

Osman, S., Senthil, R. A., Pan, J., Chai, L., Sun, Y., and Wu, Y. (2021). “Hierarchically activated porous carbon derived from zinc-based fluorine containing metal-organic framework as extremely high specific capacitance and rate performance electrode material for advanced supercapacitors.” *Journal of Colloid and Interface Science*, 591, 9–19.

Pope, M. T., Jeannin, Y., and Fournier, M. (2013). *Heteropoly and Isopoly Oxometalates*. Inorganic Chemistry Concepts, Berlin: Springer Berlin.

Pope, M. T., and Müller, A. (1991). “Polyoxometalates Chemistry: An Old Field with New Dimensions in Several Disciplines.” *Angew. Chem. Int. Ed. Engl.*, 30(1), 34–48.

Pope, M. T., and Müller, A. (Eds.). (1994). *Polyoxometalates: From Platonic Solids to Anti-Retroviral Activity*. Topics in Molecular Organization and Engineering, Dordrecht: Springer Netherlands.

Pauling, L. (1929). “THE PRINCIPLES DETERMINING THE STRUCTURE OF COMPLEX IONIC CRYSTALS.” *J. Am. Chem. Soc.*, 51(4), 1010–1026.

Pell, W. G., and Conway, B. E. (2004). “Peculiarities and requirements of asymmetric capacitor devices based on combination of capacitor and battery-type electrodes.” *Journal of Power Sources*, 136(2), 334–345.

Panwar, N. L., Kaushik, S. C., and Kothari, S. (2011). “Role of renewable energy sources in environmental protection: A review.” *Renewable and Sustainable Energy Reviews*, 15(3), 1513–1524.

- Park, D.-W., Cañas, N. A., Schwan, M., Milow, B., Ratke, L., and Friedrich, K. A. (2016). “A dual mesopore C-aerogel electrode for a high energy density supercapacitor.” *Current Applied Physics*, 16(6), 658–664.
- Ramachandran, R., and Wang, F. (2018). “Electrochemical Capacitor Performance: Influence of Aqueous Electrolytes.” *Supercapacitors - Theoretical and Practical Solutions*, L. Liudvinavičius, ed., InTech.
- Reza, M. S., Yun, C. S., Afroze, S., Radenahmad, N., Bakar, M. S. A., Saidur, R., Taweekun, J., and Azad, A. K. (2020). “Preparation of activated carbon from biomass and its’ applications in water and gas purification, a review.” *Arab Journal of Basic and Applied Sciences*, 27(1), 208–238.
- Roy, B. K., Tahmid, I., and Rashid, T. U. (2021). “Chitosan-based materials for supercapacitor applications: a review.” *J. Mater. Chem. A*, 9(33), 17592–17642.
- Rajaitha, P. M., Hajra, S., Mistewicz, K., Panda, S., Sahu, M., Dubal, D., Yamauchi, Y., and Kim, H. J. (2022). “Multifunctional materials for photo-electrochemical water splitting.” *J. Mater. Chem. A*, 10(30), 15906–15931.
- Rhule, J. T., Hill, C. L., Judd, D. A., and Schinazi, R. F. (1998). “Polyoxometalates in Medicine.” *Chem. Rev.*, 98(1), 327–358.
- Roberts, S. M., and Poignant, G. (2002). *Hydrolysis, oxidation and reduction. Catalysts for fine chemical synthesis*, Chichester (GB): J. Wiley & sons.
- Sadakane, M., and Steckhan, E. (1998). “Electrochemical Properties of Polyoxometalates as Electrocatalysts.” *Chem. Rev.*, 98(1), 219–238.
- Saikia, B. K., Benoy, S. M., Bora, M., Tamuly, J., Pandey, M., and Bhattacharya, D. (2020). “A brief review on supercapacitor energy storage devices and utilization of natural carbon resources as their electrode materials.” *Fuel*, 282, 118796.
- Salitra, G., Soffer, A., Eliad, L., Cohen, Y., and Aurbach, D. (2000). “Carbon Electrodes for Double-Layer Capacitors I. Relations Between Ion and Pore Dimensions.” *J. Electrochem. Soc.*, 147(7), 2486.
- Samantara, A. K., and Ratha, S. (2018). “Components of Supercapacitor.” *Materials Development for Active/Passive Components of a Supercapacitor*, SpringerBriefs in Materials, Singapore: Springer Singapore, 11–39.

- Sazali, N., Wan Salleh, W. N., Jamaludin, A. S., and Mhd Razali, M. N. (2020). “New Perspectives on Fuel Cell Technology: A Brief Review.” *Membranes*, 10(5), 99.
- Sevilla, M., and Mokaya, R. (2014). “Energy storage applications of activated carbons: supercapacitors and hydrogen storage.” *Energy Environ. Sci.*, 7(4), 1250–1280.
- Sharma, S., and Chand, P. (2023). “Supercapacitor and electrochemical techniques: A brief review.” *Results in Chemistry*, 5, 100885.
- Salgado, M. de F., Abioye, A. M., Junoh, M. M., Santos, J. A. P., and Ani, F. N. (2018). “Preparation of activated carbon from babassu endocarp under microwave radiation by physical activation.” *IOP Conf. Ser.: Earth Environ. Sci.*, 105, 012116.
- Subramani, K., Sudhan, N., Karnan, M., and Sathish, M. (2017). “Orange Peel Derived Activated Carbon for Fabrication of High-Energy and High-Rate Supercapacitors.” *ChemistrySelect*, 2(35), 11384–11392.
- Sheldrick, G. M. (2008). “A short history of *SHELX*.” *Acta Crystallogr A Found Crystallogr*, 64(1), 112–122.
- Sagadevan, S., Marlinda, A. R., Johan, Mohd. R., Umar, A., Fouad, H., Alothman, O. Y., Khaled, U., Akhtar, M. S., and Shahid, M. M. (2020). “Reduced graphene/nanostructured cobalt oxide nanocomposite for enhanced electrochemical performance of supercapacitor applications.” *Journal of Colloid and Interface Science*, 558, 68–77.
- Sadashiv Bubanale, M Shivashankar, and SIDDAGANGA INSTITUTE OF TECHNOLOGY. (2017). “History, Method of Production, Structure and Applications of Activated Carbon.” *IJERT*, V6(06), IJERTV6IS060277.
- Şahin, M., Blaabjerg, F., and Sangwongwanich, A. (2022). “A Comprehensive Review on Supercapacitor Applications and Developments.” *Energies*, 15(3), 674.
- Suárez, L., and Centeno, T. A. (2020). “Unravelling the volumetric performance of activated carbons from biomass wastes in supercapacitors.” *Journal of Power Sources*, 448, 227413.

- Simon, P., Gogotsi, Y., and Dunn, B. (2014). “Where Do Batteries End and Supercapacitors Begin?” *Science*, 343(6176), 1210–1211.
- Song, Y.-F. (Ed.). (2018). *Polyoxometalates-Based Assemblies and Functional Materials*. Structure and Bonding, Cham: Springer International Publishing.
- Suárez, L., and Centeno, T. A. (2020). “Unravelling the volumetric performance of activated carbons from biomass wastes in supercapacitors.” *Journal of Power Sources*, 448, 227413.
- Tirzhá L P Dantas, Alirio E Rodrigues, and Moreira, R. F. P. M. (2012). “Separation of Carbon Dioxide from Flue Gas Using Adsorption on Porous Solids.”
- Toupin, M., Brousse, T., and Bélanger, D. (2004). “Charge Storage Mechanism of MnO₂ Electrode Used in Aqueous Electrochemical Capacitor.” *Chem. Mater.*, 16(16), 3184–3190.
- Tatibouët, J.-M., Montalescot, C., Brückman, K., Haber, J., and Che, M. (1997). “A Two-Step Transformation of the Magnesium Salt of Phosphomolybdic Acid HMgPMo₁₂O₄₀Supported on Silica.” *Journal of Catalysis*, 169(1), 22–32.
- Ueda, T., Nishimoto, Y., Saito, R., Ohnishi, M., and Nambu, J. (2015). “Vanadium(V)-Substitution Reactions of Wells–Dawson-Type Polyoxometalates: From [X₂M₁₈O₆₂]⁶⁻ (X = P, As; M = Mo, W) to [X₂VM₁₇O₆₂]⁷⁻.” *Inorganics*, 3(3), 355–369.
- Wang, G., Zhang, L., and Zhang, J. (2012). “A review of electrode materials for electrochemical supercapacitors.” *Chem. Soc. Rev.*, 41(2), 797–828.
- Wang, H., Xu, Z., Kohandehghan, A., Li, Z., Cui, K., Tan, X., Stephenson, T. J., King’ondo, C. K., Holt, C. M. B., Olsen, B. C., Tak, J. K., Harfield, D., Anyia, A. O., and Mitlin, D. (2013). “Interconnected Carbon Nanosheets Derived from Hemp for Ultrafast Supercapacitors with High Energy.” *ACS Nano*, 7(6), 5131–5141.
- Wang, K., Wang, C., Yang, H., Wang, X., Cao, F., Wu, Q., and Peng, H. (2020). “Vertical graphene nanosheetsmodified Al current collectors for high-performance sodium-ion batteries.” *Nano Res.*, 13(7), 1948–1954.

- Wang, X., Yang, C., and Wang, G. (2016). “Stretchable fluoroelastomer quasi-solid-state organic electrolyte for high-performance asymmetric flexible supercapacitors.” *J. Mater. Chem. A*, 4(38), 14839–14848.
- Wu, X., Li, Y., Wu, Q., Ding, H., and Yan, W. (2014). “The invertible electrochemical properties and thermal response of a series of gel-type ionic liquids based on Polyoxometalates.” *Phys. Chem. Chem. Phys.*, 16(44), 24598–24603.
- Xue, W., Wang, W., Fu, Y., He, D., Zeng, F., and Zhao, R. (2017). “Rational synthesis of honeycomb-like NiCo₂O₄@NiMoO₄ core/shell nanofilm arrays on Ni foam for high-performance supercapacitors.” *Materials Letters*, 186, 34–37.
- Yang, F., Yu, Q., Xie, H., Zuo, Z., Hou, L., and Qin, Q. (2018). “Comparative kinetic study of coal gasification with steam and CO₂ in molten blast furnace slags.” *Korean J. Chem. Eng.*, 35(8), 1626–1635.
- Zhai, Z., Zhang, L., Du, T., Ren, B., Xu, Y., Wang, S., Miao, J., and Liu, Z. (2022). “A review of carbon materials for supercapacitors.” *Materials & Design*, 221, 111017.
- Zhang, L., Hu, X., Wang, Z., Sun, F., and Dorrell, D. G. (2018). “A review of supercapacitor modeling, estimation, and applications: A control/management perspective.” *Renewable and Sustainable Energy Reviews*, 81, 1868–1878.
- Zhang, L. L., and Zhao, X. S. (2009). “Carbon-based materials as supercapacitor electrodes.” *Chem. Soc. Rev.*, 38(9), 2520.
- Zhang, L., Xu, C. (Charles), and Champagne, P. (2010). “Overview of recent advances in thermo-chemical conversion of biomass.” *Energy Conversion and Management*, 51(5), 969–982.
- Zhi, M., Xiang, C., Li, J., Li, M., and Wu, N. (2013). “Nanostructured carbon–metal oxide composite electrodes for supercapacitors: a review.” *Nanoscale*, 5(1), 72–88.
- Zhong, C., Deng, Y., Hu, W., Qiao, J., Zhang, L., and Zhang, J. (2015). “A review of electrolyte materials and compositions for electrochemical supercapacitors.” *Chem. Soc. Rev.*, 44(21), 7484–7539.
- Zhou, D., and Han, B. (2010). “Graphene-Based Nanoporous Materials Assembled by Mediation of Polyoxometalates Nanoparticles.” *Adv Funct Materials*, 20(16), 2717–2722.

Zhu, Q., Paci, B., Generosi, A., Renaudineau, S., Gouzerh, P., Liang, X., Mathieu, C., Rountree, C., Izzet, G., Proust, A., Barrett, N., and Torteck, L. (2019). “Conductivity via Thermally Induced Gap States in a Polyoxometalates Thin Layer.” *J. Phys. Chem. C*, 123(3), 1922–1930.

Zhu, S., Wu, M., Ge, M.-H., Zhang, H., Li, S.-K., and Li, C.-H. (2016). “Design and construction of three-dimensional CuO/polyaniline/rGO ternary hierarchical architectures for high performance supercapacitors.” *Journal of Power Sources*, 306, 593–601.

LIST OF PUBLICATION

Journal Publications from this thesis work

1. **J. E Madhusree.**, Chandewar, P. R., Shee, D., and Sankar Mal, S. (2023) High-performance hybrid supercapacitor-immobilized Wells-Dawson Polyoxometalates on activated carbon electrodes. *RSC Advances*,26744-26754.
2. **J. E, Madhusree.**, Chandewar, P. R., Shee, D., and Sankar Mal, S. (2023). “Phosphomolybdic acid embedded into biomass-derived biochar carbon electrode for supercapacitor applications.” *Journal of Electroanalytical Chemistry*, 117354.
3. **J. E, Madhusree.**, Chandewar, P. R., Shee, D., and Sankar Mal, S. “Wells-Dawson Polyoxometalates Modified Lignin Derived High Surface Area Activated Carbon Electrode Materials for Energy Storage Application”. *ChemistrySelect*,e202401533.
4. **J. E, Madhusree.**, Chandewar, P. R., Shee, D., and Sankar Mal, S. “Vanadophosphomolybdates anchored on pomegranate derived activated carbon for energy storage supercapacitors”. (Communicated)

Other publications

1. **J. E, Madhusree.**, and Sankar Mal, S. (2023). “Polyoxometalates-based materials for the effluent treatment of removing heavy metals in the water pollutants: Minireview.” *Journal of Applied Nanoscience*, 1-9.
2. Maity Sukanya., **J. E, Madhusree.**, Biradar R B., Chandewar, P. R., Shee, D., Das P P., and Sankar Mal, S. (2021). “Polyoxomolybdate–Polypyrrole–Graphene Oxide Nanohybrid Electrode for High-Power Symmetric Supercapacitors”. *Journal of Energy & Fuels*, 18824-18832.

Book chapters

1. Organic-inorganic hybrid Mixed-valent Bisphosphonate-polyoxovanadates composites with Activated carbon for energy storage application. (Communicated)
2. High Surface area as an effective electrochemical material for supercapacitive applications. (Nova Publisher).

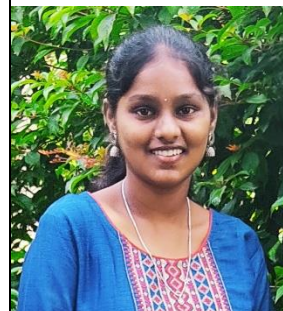
Workshop and conference attended

- ❖ Oral presentation at International Conference on “RECENT ADVANCEMENT IN MATERIAL SCIENCE AND ITS APPLICATIONS” on January 11&12th, 2023 held at the Research Center and PG Department of Physics Mannar Thirumalai Naicker College.
- ❖ Presented a poster on the “Electrochemical study of Infused Trivanadophosphomolybdate in Activated Carbon Hybrid Material” at The National Institute of Technology Meghalaya, hosted the 3rd Research conclave 2022.

CURRICULUM VITAE

MADHUSREE J E

Research Scholar, Department of Chemistry, National Institute of Technology Karnataka, Surathial-575025



PROFESSIONAL SUMMARY

A highly dedicated Doctoral Research Fellow with hands-on experience and record accomplishment in the field of Super capacitor. Self-motivated and hardworking professional with methodical and detail-oriented approach. Diligent and reliable with a strong ability to solve scientific problems, highly organized, proactive, and punctual with a team-oriented mentality.

EDUCATIONAL EXPERIENCE

- Ph.D. in Chemistry, National Institute of Technology Karnataka, India. 2019-2024
- M.Sc. in Chemistry, Sastra deemed to be university, Tanjore, Tamilnadu, India 2017 - 2019
- B.Sc. in Chemistry, Jairam Arts and Science College, Tamilnadu, India. 2014 – 2017.

RESEARCH EXPERIENCE

- PhD Scholar (December 2019 - Thesis Submitted) Department of Chemistry, National Institute of Technology Karnataka, Surathkal, India.
- Masters Research Project (December 2017 – May 2019) Topic: Catalyst Free Synthesis Of 4-Formylbenzoic Acid Derived Dipyrromethene's, School Of Chemical And Biotechnology, Sastra Deemed To Be University, Tanjore, India.

MAJOR PUBLICATIONS

J. E Madhusree., Chandewar, P. R., Shee, D., and Sankar Mal, S. (2023) High-performance hybrid supercapacitor-immobilized Wells-Dawson Polyoxometalates on activated carbon electrodes. *RSC Advances*, 26744-26754.

J. E, Madhusree., Chandewar, P. R., Shee, D., and Sankar Mal, S. (2023). "Phosphomolybdic acid embedded into biomass-derived biochar carbon electrode for supercapacitor applications." *Journal of Electroanalytical Chemistry*, 117354.

J. E, Madhusree., and Sankar Mal, S. (2023). "Polyoxometalates-based materials for the effluent treatment of removing heavy metals in the water pollutants: Minireview." *Journal of Applied Nanoscience*, 1-9.

Maity Sukanya., **J. E, Madhusree.**, Biradar R B., Chandewar, P. R., Shee, D., Das P P., and Sankar Mal, S. (2021). "Polyoxomolybdate–Polypyrrole–Graphene Oxide Nanohybrid Electrode for High-Power Symmetric Supercapacitors". *Journal of Energy & Fuels*, 18824-18832.

WORKSHOP AND CONFERENCE ATENDED

- ❖ Oral presentation at International Conference on “RECENT ADVANCEMENT IN MATERIAL SCIENCE AND ITS APPLICATIONS” on January 11&12th 2023 held at the Research center and PG department of physics Mannar Thirumalai Naicker college.
- ❖ Presented a poster on the topic of the “Electrochemical study of Infused Trivanadophosphomolybdate in Activated Carbon Hybrid Material” at The National Institute of Technology Meghalaya hosted the 3rd Research conclave 2022.

RELEVANT LABORATORY AND INSTRUMENTATION SKILLS

- ✚ Setting the reaction setup for catalysis reactions and electrochemical setups.
- ✚ Synthesis of various Polyoxometalates, conducting polymer and its composites.
- ✚ Synthesis of Biomass-derived Activated Carbon.
- ✚ Electrode coating for electrochemical reactions.
- ✚ Construction of Symmetric and Asymmetric ultracapacitor cells.
- ✚ Operating and analysis of FTIR spectroscopy, UV-VIS, TGA, BET, XPS, PXRD, FESEM, TEM and Electrochemical studies (CV, GCD, Impedance etc.)

GENERAL SKILLS

- ✚ Microsoft Office, Microsoft Excel.
- ✚ Handling Xpert Highscore, Origin Pro 2022, ZSimpWin, chem draw, ImageJ software and Topspin.
- ✚ Guided 2 PG students with project works during my Ph.D.
- ✚ Problem-Solving & Critical Thinking.
- ✚ Lab Report Completion Procedures, Discussion Facilitation.
- ✚ Quantitative Research & Qualitative Research.
- ✚ Academic Writing, Academic Presentations & Project Support.
- ✚ Laboratory Oversight, Academic Monitoring.
- ✚ Group Assistance & Administrative Support.

PERSONAL INFORMATION

Name : Madhusree J E
Father's Name : Elangovan P J
Nationality : Indian
Gender : Female
Date of Birth :10.06.1997
Marital Status : Single
Personal Telephone Number :+91 8072227014
Email id :madhusrije@gmail.com
Address :22/7, Arumugam Street,
Dadagapatty,
Salem – 636006.

